MOLECULAR IMAGING OF INFLAMMATION-RELATED BIOMARKERS IN CANCER, FIBROSIS, AND NEURODEGENERATIVE DISEASE

by
Stephanie Slania

A dissertation submitted to Johns Hopkins University in conformity with the requirements for the degree of Doctor of Philosophy

Baltimore, Maryland
April 2021

Abstract

The overall goal of this thesis is to develop novel molecular imaging strategies for the targeted imaging of inflammation-related biomarkers of disease. In particular, these strategies focus on the careful development and assessment of molecular imaging agents targeting relevant disease markers related to cancer (fibroblast activation protein), neurodegenerative disease (nicotinic acetylcholine receptors and soluble epoxide hydrolase), and fibrosis (death receptor 5). We aim to show the feasibility and importance of these efforts in the following 6 chapters. In chapter 1, we provide an introduction to molecular imaging, discuss inflammation-related biomarkers of diseases, and outline the scope of the dissertation. In chapter 2, we focus on the development of small molecule imaging agents targeting fibroblast activation protein and the assessment of these agents in *in vitro* and *in vivo* cancer models. In chapters 3-5, we focus on the kinetic modeling of three separate molecular imaging agents, [^{18}F]FNDP, [^{18}F]XTRA, and [^{18}F]ASEM targeting soluble epoxide hydrolase (sEH) and nicotinic acetylcholine receptors (nAChRs) in the brain. Chapters 3 and 4 focus on first in human studies of [^{18}F]FNDP and [^{18}F]XTRA, respectively, whereas in chapter 5 we focus on a study of [^{18}F]ASEM distribution with healthy aging. Finally, in chapter 6, we focus on the development of new peptide-based imaging agents directed at the engagement of death receptor 5 and initial *in vitro* assessment of these peptide agents in cellular models.

Advisor

Martin G. Pomper, M.D., Ph.D.

Professor of Radiology and Radiological Science, Johns Hopkins University

Committee Members

Zaver M. Bhujwalla, M.Sc., Ph.D.

Professor of Radiology and Radiological Science, Johns Hopkins University

Jordan J. Green, Ph.D. (Reader)

Professor of Biomedical Engineering, Johns Hopkins University

Seulki Lee, Ph.D.

Associate Professor of Radiology and Radiological Science, Johns Hopkins University

Acknowledgements

I would like to thank my advisor, Dr. Marty Pomper, for his invaluable guidance and training these past six years. He has opened my world to a whole new realm of science and has played a fundamental part in shaping me into the scientist I am today. He has given me so much opportunity to grow and supported me through all the ups and downs of graduate school. I will forever value my time here at Hopkins because of him.

I'd also like to thank my committee members, Dr. Zaver Bhujwalla, Dr. Jordan Green, and Dr. Seulki Lee, for their support and guidance over the past year. Their feedback and input on my work was very valuable and helped me refine my work further.

The support of my colleagues, both past and present, in the Precision Molecular Imaging Coalition has been invaluable to me the past six years. I could not have asked for a better team of scientists to train alongside with and am grateful for all our time together. I am forever grateful for the mentorship and training I received from Dr. Xing Yang, who took me under his wing for my first few years of graduate school. I am grateful for Dr. Ron Mease and Dr. Sridhar Nimmagadda, who were never too busy for a question and were always willing to help me work towards my goals. Their patience and kindness will be something I will never forget. Dr. Jennifer Coughlin and Dr. Yong Du, thanks for giving me the opportunity to get involved in the clinical side of research and see how our work can directly impact patients. Working as a team with you two has been one of the most rewarding parts of my time here at Hopkins. Ala Lisok, thank you for always being a helping hand and making late-night biodistribution studies a lot more enjoyable. Karen Stanton, thank you for always being the most responsive and helpful when it came to anything administrative-related and for making everything a little easier. Your support did not go unnoticed.

To my mentors back at UIUC, thank you for always believing I would be here someday. Dr. Dobrucki, thank you for introducing me to molecular imaging research and for your hands on training in the field. I will always be appreciative of the time and energy you gave to me. Dr. Jennifer Amos and Kerri Green, thank you for being my advocates throughout undergrad and showing me that

graduate school was even an option. I would have been lost without your career and educational guidance.

To my Baltimore “family”, thanks for making my time here in the city some of the best times of my life. I will miss our potlucks and game nights, but I know these friendships will last long past our time here in Baltimore. Morgan, I will forever cherish your kindness and will always have fond memories of our little home on Centre Street. Elana, thanks for being one of my biggest supporters here and for always being up for all my antics. I will miss our times together in Baltimore but am so excited to see where your career will take you.

To my friends from UIUC, I am so lucky that a freshman year study group ended up turning in to one of the most supportive friend groups. These past 6 years have shown me just how much you all mean to me and I am looking forward to all of our adventures in the years to come. Ashley and Alyssa, thank you for being my sisters, constant sources of advice, and always there when I needed a moment to take a breath. I couldn’t have done it without you two.

Jen, Kelly, and Lisa, I would not be here today without your love and support. You have been by my side since my elementary school days, where the dream of becoming Dr. Slania was not even something that I knew was an option for a little girl from the Chicago suburbs. Thanks for never doubting my abilities even when I doubted myself, for lifting me up during the hardest moments, and celebrating me every step along the way.

To Brett, thank you for your patience and love, especially during the most grueling moments of graduate school. You are the best partner and dog dad I could ask for and I cannot wait to see where this life takes us. Thanks for always stepping up when I needed you most, for proofreading every presentation, and making sure I took a moment to enjoy the process.

And finally, I would like to thank my family for the insurmountable amount of love and support they have given me throughout my life. You taught me the value of hard work and showed me that I could be anything I wanted to be as long as I put my heart into it. Thank you for giving me the opportunity to go to college, for embracing my new life here in Baltimore, and, most importantly, for being my #1 supporters. This Ph.D. is also for you.

Dedication

To my parents, Sheri and Bob

I wouldn't know where I'd be without your love and support

Table of Contents

List of Tables

List of Figures

Chapter 1: Introduction

Introduction to Molecular Imaging

Molecular imaging can be defined as the visualization and characterization of biological processes at the molecular and cellular level[1]. A distinct advantage of molecular imaging is its non-invasive nature, allowing it to characterize disease processes in vivo without relying on surgical procedures or biopsies[2]. This has led to the application of molecular imaging beyond just disease detection, but also in the development of precision medicine therapies and drug development[3]. Molecular imaging is impacting medicine directly by helping detect disease in early stages, acting as a guide for determining patient-specific therapies, and measuring the effects of targeted therapies at a molecular level[2]. Molecular imaging research is characterized by the combination of various technologies, such as imaging modalities and molecular imaging agents, in order to generate information on imaging targets. Due to the broad nature of this field, the majority of molecular imaging research is highly multidisciplinary, with teams composed of chemists, biologists, imaging scientists, and clinical experts working together to achieve their research goals. Due to the broad nature of this field, molecular imaging strategies have been employed to answer questions in various realms of research, including neuroscience[4], inflammatory diseases[5], cancer[6], cardiology[7], and theranostics[8].

The majority of molecular imaging modalities can be categorized into two groups: functional imaging techniques and anatomical imaging techniques (Figure 1-1). Functional imaging techniques are characterized by the ability to detect changes in biochemical processes at the molecular and cellular level and usually rely on an imaging agent or “probe” to provide information at the site of interest. Popular in both clinical and preclinical settings, single photon emission computed tomography (SPECT) and positron emission tomography (PET) employ radionucleotide-based imaging agents to image and detect changes in activity in tissues of interest. Optical and fluorescent imaging techniques employ fluorescent-based probes to capture signals and are primarily utilized in the

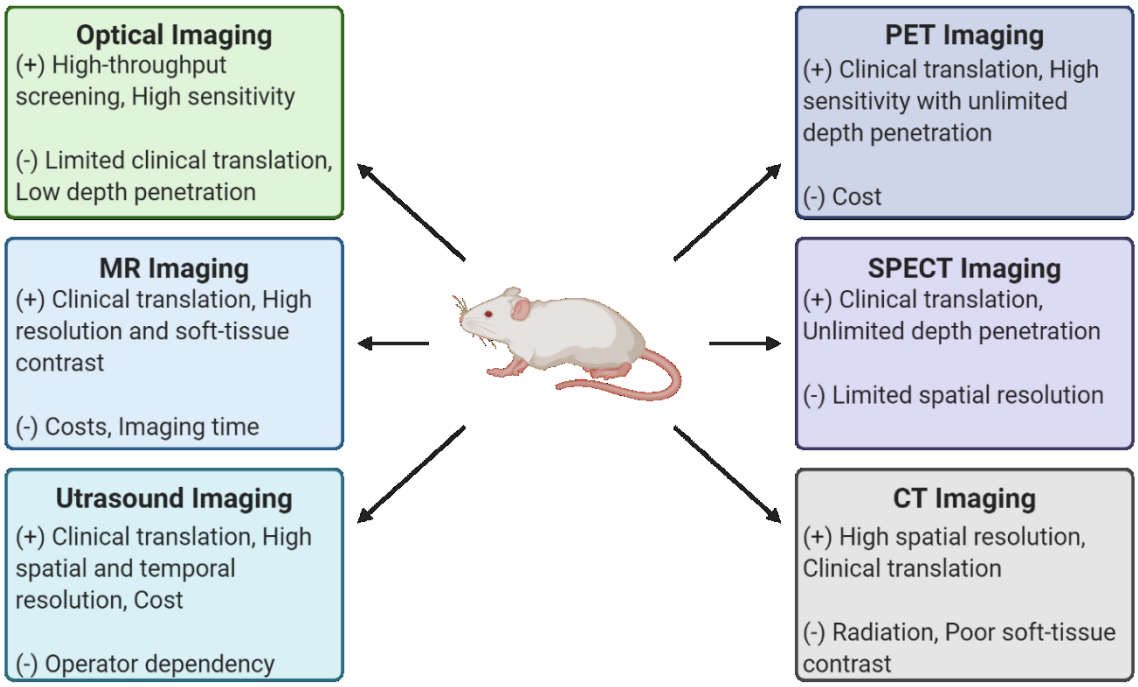

Figure 1-1. A summary of imaging modalities used for molecular imaging.

Adapted from Willmann JK et al.[3]

preclinical setting[9]. These techniques are characterized by high sensitivity but lack spatial resolution. In contrast, anatomical imaging techniques provide high structural resolution and provide detailed information on the structure that is being imaged. These techniques include computed tomography (CT), ultrasound (US), and magnetic resonance imaging (MRI) and are commonly employed in both clinical and preclinical applications. To advantage of the strengths of the various imaging techniques, anatomical and functional imaging techniques are commonly combined, resulting in molecular imaging strategies that can provide powerful information on targets of interest *in vivo*[10].

A central part of molecular imaging research is the identification of disease-specific targets and finding ligands that interact with those targets. This process has been greatly assisted with the rise of “omics” research, with more and more disease-associated targets being identified and studied[6]. Once a target has been identified, the careful development and characterization of molecular imaging agents is the next crucial step. Molecular imaging agents are usually comprised of two parts, a signal and a targeting moiety. The signal component is application-dependent, and its main function is to report back a signal to the imaging modality so it can generate an image. The targeting moiety is what directs the imaging agent to the target of interest and can take on a variety of forms, including small-molecules, peptides, antibodies, antibody fragments, aptamers, and nanoparticles[11]. These components are usually connected with a linker, which bounds the signal to the targeting moiety and helps tune the pharmacokinetic properties of the agent[12]. The combination of signal, targeting moiety, and linker should be optimized for each molecular imaging application to ensure favorable pharmacokinetics, binding specificity, and stability of these agents.

The development and validation of molecular imaging agents is very similar to the drug-development pipeline[13]. Once a target of interest has been identified, the imaging agent is designed and a synthesis approach is developed. Next, the imaging agent goes through lead compound optimization, where the agent is assessed for its binding ability and specificity for the target of

interest. This process is important and often revisited many times to ensure that the agent has favorable chemical properties before moving towards further testing. Usually done in conjunction with this is the preclinical assessment of the agent in cellular and small animal models. This step is crucial to understand how the agent is behaving *in vivo* and evaluating the pharmacokinetic and biodistribution properties of the agent of interest. If the agent is showing favorable properties, the agent will move forward toward larger animal testing, commonly small primates like baboons, before moving towards human clinical studies. Like the drug development pipeline, many molecular imaging agents don't make it to the end of the pipeline and to use in the clinical setting, so there is increasing interest in optimizing this process in order to increase the success of new molecular imaging agents in development[14].

Inflammation-Related Biomarkers of Disease

Inflammation is the immune system's response to harmful stimuli such as bacteria, viruses, toxins, and injury[15]. The goal of the inflammatory response is to eliminate pathogens and promote tissue repair and recovery[16]. Inflammation is initiated by tissue resident cells that detect pathogen-associated molecular patterns (PAMPs) and/or damage-associated molecular patterns (DAMPs), which then recruit additional immune cells of the innate and adaptive immune system through release of cytokines and chemokines[17]. This leads to a local inflammatory environment the enables the transport of cells from the blood stream to the site of inflammation by changes in vascular permeability, blood flow, and endothelial adhesion[18]. A normal inflammatory response is characterized by the temporary upregulation of inflammatory activity while a DAMP and/or PAMP is present followed by resolution and tissue repair[19]. In contrast, chronic inflammatory responses occur when acute inflammatory processes fail to eliminate tissue injury and are characterized by a persistent inflammatory state, the infiltration of macrophages and lymphocytes, and dysregulated tissue remodeling[20]. Chronic inflammation is implicated in a variety of diseases, including cancer, neurodegenerative disease, and fibrosis, which can be characterized by distinct biomarkers.

Fibroblast Activation Protein

Fibroblast activation protein (FAP), a serine protease, is a member of the dipeptidyl peptidase (DPP) family of proteins, which are known for their unique ability to cleave prolyl bonds two residues from the N terminus[21]. While FAP expression in normal tissues is minimal, it is highly upregulated in the chronic inflammatory environment of cancer, with FAP being expressed in over 90% of epithelial tumors[22]. FAP is expressed by both cancer epithelial cells and the surrounding stromal cells in the tumor microenvironment[23]. That expression supports tumorigenesis by contributing to an active cancer stroma and participating in the enzymatic remodeling of the ECM essential for cancer cell invasion and metastasis[24].

Nicotinic Acetylcholine Receptors

Nicotinic acetylcholine receptors (nAChRs) are members of the Cys-loop superfamily of pentameric ligand-gated ion channels[25]. The most commonly expressed nAChR subtypes in mammalian central nervous system (CNS) are the heteromeric α4β2 and homomeric α7 subtypes. The discovery that α4β2 and α7 nAChRs were abundantly expressed in the CNS and that they play an important role in neurotransmission and neuronal integration led to increased interest in understanding the role these receptors play in neurodegenerative disease. Neurodegenerative diseases are characterized by neuroinflammation and are characterized by an altered distribution of the α4β2 and α7 nAChRs. In general, there is an observed loss of the α4β2 nAChR in the presence of neurodegenerative disease[26]. In contrast, an increase in the density of the α7 nAChR is observed in neurodegenerative disease, likely due to the suspected role this receptor plays in the cholinergic anti-inflammatory pathway[27].

Soluble Epoxide Hydrolase

Soluble epoxide hydrolase (sEH) is an enzyme that metabolizes anti-inflammatory epoxy fatty acids to relatively inert 1,2-diol forms. In this manner, the availability and activity of sEH may critically control the bioavailability of epoxyeicosatrienoic and epoxydocosapentaenoic acids that have vasoactive and anti-inflammatory roles. sEH is expressed widely throughout the body and a high

availability or activity of this enzyme may promote inflammation in local tissues[28]. This promotion of an inflammatory microenvironment may exacerbate pathological changes in several clinical conditions, such as vascular cognitive impairment (VCI) where greater sEH expression was observed in subjects with VCI versus age matched controls[29].

Death Receptor 5

Death receptor 5 (DR5) triggers apoptosis upon binding of tumor necrosis factor-related apoptosis-inducing ligand (TRAIL). This apoptosis can be triggered either through the extrinsic or intrinsic apoptotic pathways. Recently, there has been an interest in the role of death receptor 5 in fibrosis. In a study of scleroderma, it was observed that in skin biopsies of patients with systemic sclerosis there was an upregulation of mRNA *DR5*, which was mainly colocalized with smooth muscle actin positive (aSMA+) myofibroblasts[30]. In wound healing, myofibroblasts help initiate the scarring process[31], but in the case of chronic inflammation, they are overactive and contribute to fibrosis[32]. Similar results were observed in liver fibrosis, where activated hepatic stellate cells (aHSCs), the major cell type responsible for liver fibrosis, in liver sections of patients with liver cirrhosis upregulated death receptor 5 compared to healthy liver tissues[33]. Taken together, this has led to increased interested in the role of death receptor 5 in fibrosis and how its expression plays a role in the control of apoptosis in fibrotic diseases.

Scope of Dissertation

The overall goal of this thesis is to develop novel molecular imaging strategies for the targeted imaging of inflammation-related biomarkers of disease. In particular, these strategies focus on the careful development and assessment of molecular imaging agents targeting relevant disease markers related to cancer (fibroblast activation protein), neurodegenerative disease (nicotinic acetylcholine receptors and soluble epoxide hydrolase), and fibrosis (death receptor 5). We aim to show the feasibility and importance of these efforts in the following 5 chapters. In chapter 2, we focus on the development of small molecule imaging agents targeting fibroblast activation protein and the assessment of these agents in *in vitro* and *in vivo* cancer models. In chapters 3-5, we focus

on the kinetic modeling of three separate molecular imaging agents, [^{18}F]FNDP, [^{18}F]XTRA, and [^{18}F]ASEM targeting soluble epoxide hydrolase (sEH) and nicotinic acetylcholine receptors (nAChRs) in the brain. Chapters 3 and 4 focus on first in human studies of [^{18}F]FNDP and [^{18}F]XTRA, respectively, whereas in chapter 5 we focus on a study of [^{18}F]ASEM distribution with healthy aging. Finally, in chapter 6, we focus on the development of new peptide-based imaging agents directed at the engagement of death receptor 5 and initial *in vitro* assessment of these peptide agents in cellular models.

Chapter 2: Development and assessment of inhibitor-based agents for targeted molecular imaging of fibroblast activation protein alpha (FAP)

Summary:

The focus of this chapter is on the development of small molecule imaging agents targeting FAP and the assessment of these agents in *in vitro* and *in vivo* cancer models. These agents, inspired by FAP-specific inhibitors with a (4-quinolinoyl)-glycyl-2-cyanopyrrolidine scaffold, will be assessed for their ability to inhibit FAP binding after chemical modification. To gain a deeper knowledge of FAP expression in cancer, we will examine FAP expression in cancer cell lines and human primary tumors using database-driven analyzes. Then we will assess the binding ability and specificity of these agents in cell-based cancer models, specifically looking at selectively of these agents for FAP over DPP-IV, an enzyme of the sample family in which it shares significant sequence and structural homogeneity. After characterization *in vitro*, we will determine the biodistribution and specificity of these agents in tumor xenograft mouse models.

Imaging of fibroblast activation protein in cancer xenografts using novel (4-quinolinoyl)-glycyl-2-cyanopyrrolidine-based small molecules

This work has been published and is reprinted here with permission by *The Journal of Medicinal Chemistry.*

Slania SL, Das D, Lisok A, Du Y, Jiang Z, Mease RC, Rowe SP, Nimmagadda S, Yang X, Pomper MG. Imaging of fibroblast activation protein in cancer xenografts using novel (4-quinolinoyl)-glycyl-2-cyanopyrrolidine-based small molecules. J Med Chem. 2021 Mar; 64(7):4059-4070.

Abstract

Fibroblast activation protein (FAP) has become a favored target for imaging and therapy of malignancy. We have synthesized and characterized two new (4-quinolinoyl)-glycyl-2-cyanopyrrolidine-based small molecules for imaging of FAP, **QCP01** and [^{111}In]**QCP02**, using optical and single-photon computed tomography/CT, respectively. Binding of imaging agents to FAP was assessed in six human cancer cell lines of different cancer types: glioblastoma (U87), melanoma (SKMEL24), prostate (PC3), NSCLC (NCIH2228), colorectal carcinoma (HCT116), and lung squamous cell carcinoma (NCIH226). Mouse xenograft models were developed with FAP-positive U87 and FAP-negative PC3 cells to test pharmacokinetics and binding specificity *in vivo*. **QCP01** and [^{111}In]**QCP02** demonstrated nanomolar inhibition of FAP at K_i values of 1.26 and 16.20 nM, respectively. Both were selective for FAP over DPP-IV, a related serine protease. Both enabled imaging of FAP-expressing tumors specifically *in vivo*. [^{111}In]**QCP02** showed high uptake at 18.2 percent injected dose per gram in the U87 tumor at 30 min post-administration.

Introduction

Fibroblast activation protein (FAP) is highly upregulated at sites of active tissue remodeling, including wound healing, fibrosis, and cancer[23,34–36]. It is a member of the dipeptidyl peptidase (DPP) family of serine proteases known for their unique ability to cleave prolyl bonds two residues from the N-terminus[21]. FAP has the ability to cleave after prolyl bonds within peptides (not just at the N-terminus), which enables it to act as a collagenase and cleave type I collagen[37–40]. The collagenase activity of FAP is a major driver in the remodeling of the extracellular matrix (ECM) in a variety of diseases, including cancer[38,40,41]. While FAP expression in normal tissues is minimal, it is highly upregulated in cancer, with presence in over 90% of epithelial tumors[22].

In cancer, FAP has emerged as a distinct marker of cancer-associated fibroblasts (CAFs) and a key regulator and driver of the tumor microenvironment (TME). CAFs are one of the largest components of the TME and promote tumor growth and cell invasion by secreting pro-inflammatory factors and growth factors as well as remodeling the ECM[42,43]. In addition to cells within the TME, FAP expression can be present within malignant epithelial cells[44]. FAP promotes tumor growth through ECM remodeling, which leads to the formation of an active cancer stroma, essential for cancer cell invasion and metastasis[24]. This has been observed clinically, where FAP expression was increased at the invasive front of tumor samples of colorectal cancer, further supporting its role in invasion and metastasis[45]. FAP also contributes to the formation of an immunosuppressive TME by enabling tumor-promoting inflammation[46]. Due to the important roles FAP plays in the TME, there is increasing interest in utilizing it as a target for imaging and therapy.

Clinical studies show that FAP expression has prognostic value in a variety of cancers. In pancreatic cancer, FAP expression is related directly to poor clinical outcome. Patients with pancreatic cancer and high FAP expression have lower chances of overall and disease-free survival[47]. In non-small-cell lung cancer (NSCLC), a larger percentage of cells staining positively for FAP and a higher FAP-staining grade were both significant predictors of poor overall survival[48]. Henry *et al.* observed

similar results in colon cancer, where patients with high levels of tumor stromal FAP expression were more likely to progress and develop metastases[49]. These results, generated from biopsy specimens, have motivated the search for ways to interrogate FAP concentration *in vivo*, preferably non-invasively so that repeat measurements would be possible.

Antibody-based imaging agents targeting FAP were first tested clinically over 25 years ago[50], with immuno-positron emission tomography (PET) of FAP having more recently been used in preclinical models, such as to delineate rheumatoid arthritis[51]. However, the small-molecule FAP-targeting agents have captured the most attention recently. Such compounds, if suitably functionalized, promise to have superior and modifiable pharmacokinetics, enabling imaging soon after injection, among other advantages of using drug-like molecules for imaging.

A variety of small-molecule FAP inhibitors have been functionalized for imaging. MIP-1232, based on a boronic acid FAP inhibitor, demonstrated its ability to bind FAP-positive SK-MEL-187 (melanoma) xenografts[52]. However, boronic acid FAP inhibitors often have affinity for multiple prolyl peptidases related to FAP, limiting the specificity of these agents[53,54]. Lindner *et al.* recently developed theranostic agents[55] based on the specificity of the (4-quinolinoyl)-glycyl-2-cyanopyrrolidine nucleus of general structure **2** targeting FAP (Figure 2-), originally reported by Jansen *et al.*[56,57] While the radioiodinated inhibitor **FAPI-01** (Figure 2-) suffered from rapid deiodination, radiometal complexes of **FAPI-02** or **FAPI-04** (^{68}Ga or ^{177}Lu, Figure 2-) exhibited high and rapid uptake in FAP-expressing cells and mouse xenograft models[58]. Early clinical studies of those agents in pancreatic, head and neck, colon, lung, and breast cancers indicate that both [^{68}Ga]**FAPI-02** and [^{68}Ga]**FAPI-04** can be used to detect FAP expression in primary tumors as well as metastatic lesions and indicate the potential of FAP-targeted imaging to visualize the components of the TME[59]. Roy *et al.* have also recently leveraged the 2-cyanopyrolidine moiety for FAP binding, but utilized a pyridine rather than a quinoline to link to a variety of imaging and therapeutic functionalities to good effect[60].

Despite the use of FAP-targeted small-molecule PET agents in clinical studies, a comprehensive preclinical evaluation has not been carried out to ascertain an optimal compound for clinical use. Here, we build toward a more complete understanding of these agents with the preclinical development of two novel FAP-targeted imaging agents based on the (4-quinolinoyl)-glycyl-2-cyanopyrrolidine scaffold, **QCP01** and [^{111}In]**QCP02**. These agents are equipped for near-infrared fluorescence (NIRF) and single-photon emission computed tomography (SPECT) imaging, respectively. **QCP01** and **QCP02** share the same (4-quinolinoyl)-glycyl-2-cyanopyrrolidine scaffold as **FAPI-02** but differ in the linking group using a flexible linear linker instead of one containing a semi-rigid piperazine moiety, potentially allowing for better penetration into the binding site. Also, the chelating group, 2-1,4,7,10-tetraazacyclododecane-1,4,7,10-tetra acetate (DOTA-GA) in **QCP02**, contains an additional carboxylate group compared to the chelator in **FAPI-02** and **FAPI-04**, increasing affinity for radiometals, including ^{111}In[61,62]. We chose ^{111}In as the imaging radionuclide because of the high affinity to DOTA-GA, its ready detectability with SPECT by virtue of two emitted photons (171 and 245 keV), and its long physical half-life (2.8 days), which could accommodate lengthy imaging times after administration if needed[63]. We evaluated the affinity and specificity of these agents *in vitro* and studied their abilities to image cancer xenografts in mouse models. Additionally, to examine further the role of FAP in cancer, we analyzed the FAP expression profiles in the Cancer Cell Line Encyclopedia (CCLE) and The Cancer Genome Atlas (TCGA) data sets.

Results and Discussion

Chemical Synthesis

The FAP binding reactive moiety was synthesized by coupling 6-hydroxyquinoline-4-carboxylic acid (**3**) with glycine methyl ester hydrochloride to give **4**. Alkylation of **4** with *tert*-butyl-1-(3-bromopropyl)carbamate produced **5**, which underwent basic hydrolysis to give acid **6** (Figure 2-2). Compound **6** was coupled with (*S*)-2-pyrrolidine carbonitrile hydrochloride to produce the common intermediate **7**. **QCP01** was prepared by acid deprotection of **7** to produce intermediate **8**, which was

conjugated with IRDye 800CW-NHS (LI-COR Biosciences, Lincoln, NE) under basic conditions. Similarly, **QCP02** was prepared by conjugation with DOTA-GA(*t*-Bu)$_4$-*N*-hydroxysuccinimide (NHS)[64], followed by acid hydrolysis of the *ter*t-butyl ester groups. Complexation of non-radioactive $^{113/115}$In (III) and radioactive ^{111}In (III) with **QCP02** was carried out in 0.2 M sodium acetate buffer (pH 5.5–6.0) at 70 °C, followed by purification with reverse-phase semi-preparative high-performance liquid chromatography (HPLC). The isolated yields of [$^{113/115}$In]**QCP02** and [^{111}In]**QCP02** were 79 and 69–74%, respectively (n = 4). The radiochemical purity of [^{111}In]**QCP02** was >95%, as measured by radio-HPLC (Supplemental Figure 2-1). Both **QCP02** and **QCP01** were sterile-filtered and formulated in saline solution prior to use.

FAP Inhibitory Capacity

To determine potency toward FAP, we measured the inhibitory capacity of **QCP01** and [$^{113/115}$In]**QCP02** against a fluorogenic FAP substrate (Ala-Pro-AMC) of human recombinant FAP (Supplemental Figure 2-2). **QCP01** demonstrated low nanomolar inhibition of FAP with a K_i of 1.26 nM (95% confidence interval: 0.95–1.67 nM). [$^{113/115}$In]**QCP02** also showed strong inhibition, with a K_i value of 16.20 nM (95% confidence interval: 10.34–26.37 nM). These results demonstrated the FAP binding potential of the synthesized compounds and showed that functionalization of the inhibitor scaffold did not substantially affect its inhibition of FAP *in vitro*.

FAP Expression in Human CCLE Database-Derived and Primary Tumor-Derived TCGA Data Sets

Due to the prominent role FAP plays in cancer and the lack of understanding of its expression across the cancer spectrum, we wanted to gain a detailed picture of FAP expression in cancer cell lines as well as in primary tumor samples. To do so, we obtained gene expression data on FAP from 1047 cancer cell lines from the CCLE database to examine the heterogeneity of FAP expression across cancer cell types. Cancer cell lines that showed high FAP expression include fibroblast-like, glioma, melanoma, osteosarcoma, and upper aerodigestive cancers (Figure 2-3A). Low FAP expression was seen in a variety of leukemia and lymphoma subtypes as well as in prostate cancer.

Using these results, we chose six cancer cell lines of different cancer types for *in vitro* studies from the high- and low-expression subtypes.

Further analysis of the TCGA data set allowed us to examine FAP expression in primary tumor samples across 32 different cancers. Similar to the CCLE results, we observed that FAP expression in primary tumor samples varied across cancer types (Figure 2-3B). High FAP expression was seen in pancreatic ductal adenocarcinoma, a cancer where stroma is known to play a prominent role[65]. Other cancers including breast, mesothelioma, and head and neck also showed high FAP expression. In contrast, low FAP expression was seen in thymoma and acute myeloid leukemia. Additionally, when comparing FAP expression between primary tumor and normal solid tissue samples, we saw that in a majority of cancer types, FAP expression was higher in primary tumors compared to the corresponding normal tissue (Figure 2-3C). Further analysis of FAP expression in primary melanoma and metastases showed a trend in increase in FAP expression in metastases but had no statistical significance (Supplemental Figure 2-4).

In Vitro Fluorescence

All six selected cell lines were tested for FAP expression by flow cytometry (Supplemental Figure 2-3) and observed to have variable FAP expression levels (Figure 2-4). For *in vitro* binding studies, binding of **QCP01** was observed in all three FAP-positive cell lines (Figure 2-4A). **QCP01** binding was observed at concentrations as low as 1.56 nM and exhibited concentration-dependent binding that was saturated at 50 nM. In contrast, no specific binding of **QCP01** was observed in FAP-negative cell lines at any of the concentrations tested. This was further illustrated in the binding curves, which showed that the FAP-negative cell lines exhibited minimal binding of **QCP01** (Figure 2-4A).

Cellular binding of [^{111}In]**QCP02** was also assessed *in vitro*. After incubation with [^{111}In]**QCP02** and subsequent washing, FAP-positive U87 cells demonstrated over 30% binding of the incubated dose of [^{111}In]**QCP02** (0.037 MBq) (Figure 2-4B). In contrast, FAP-negative PC3 cells showed 0.01%

binding of the incubated dose. This difference in binding of [^{111}In]**QCP02** was significant between the FAP-positive and FAP-negative cell lines, with a *P*-value of <0.001.

To examine the specificity of our compounds further, inhibition studies were performed in the FAP-positive cell lines (U87, NCIH228, and SKMEL24) using **QCP01**. Cells were pretreated with either Val-boroPro (IC_{50}; FAP: 0.066 ± 0.011 μM, DPP-IV: 0.022 ± 0.001 μM)[66] or sitagliptin, (IC_{50}; FAP: >100 μM, DPP-IV: 0.04 ± 0.001 μM)[66], followed by incubation with **QCP01**. When pretreated with Val-boroPro, FAP-positive cell lines demonstrated dose-dependent inhibition of the fluorescence signal, indicating decreased binding of **QCP01** with increasing concentration of Val-boroPro (Figure 2-4C). In contrast, **QCP01** binding by FAP-positive cell lines was not inhibited by pretreatment with sitagliptin. These results show that **QCP01** binds to FAP and not DPP-IV when binding to target cells since inhibition of DPP-IV alone did not affect binding of **QCP01**. Taken together, the results establish the specificity of **QCP01** to bind FAP *in vitro*.

NIRF Imaging of QCP01 in a Murine Xenograft Model

To evaluate the ability of **QCP01** to bind FAP *in vivo* and to gain insight into its biodistribution, we performed NIRF imaging in tumor-bearing mice. NIRF imaging results illustrated the pharmacokinetic behavior of **QCP01** *in vivo*. Emission from intact, living, and unshaven tumor-bearing mice demonstrated uptake of **QCP01** in U87 xenografts at 30 min after injection (Supplemental Figure 2-5). This uptake persisted up to 5 h after injection, with washout after 24 h. PC3 tumors showed mild uptake of **QCP01** at 30 min after injection until 5 h, with washout at 24 h. **QCP01** uptake in normal tissues was observed to a mild degree (moderate in the kidney) at 30 min after injection and washed out slowly over time. At 5 h after injection, post-mortem studies were performed to enable exposure of organs for NIRF imaging (Figure 2-5). Although difficult to quantify as the image is planar, one can observe increased binding of **QCP01** in the FAP-positive U87 xenograft compared to that in the FAP-negative PC3 xenograft. This difference was further pronounced in the *ex vivo* organ tissue, with the excised U87 tumor consistently showing higher **QCP01** uptake than the PC3 tumor at 5, 24, and 48 h after injection.

SPECT-CT Imaging and Biodistribution of [^{111}In]QCP02 in a Murine Xenograft Model

SPECT-CT imaging showed high and specific uptake of [^{111}In]**QCP02** in U87 xenografts (Figure 2-6) as early as 1 h post injection and was retained for up to 10 h. In contrast, low uptake of [^{111}In]**QCP02** in the PC3 xenografts was observed at all imaging time points, further demonstrating the *in vivo* specificity of [^{111}In]**QCP02** for FAP. *Ex vivo* biodistribution of [^{111}In]**QCP02** correlated with the observed SPECT-CT imaging results (Figure 2-6, Supplemental Table 2-1). [^{111}In]**QCP02** uptake in the U87 xenograft was 3–4-fold higher than that in the PC3 xenograft (16.09 ± 4.17 vs 4.12 ± 0.36% ID/g at 1 h, $P < 0.0012$) at all time points. At as early as 5 min, the tumor uptake in U87 was over 10% ID/g, which peaked at 30 min post injection (18.16 ± 11.67% ID/g) and remained between 16 and 8% ID/g for up to 6 h. In contrast, the PC3 tumor uptake was less than 5% ID/g at all time points, which was similar to the radioactivity in blood. Washout of the radiotracer in U87 tumors was observed by 28 h post injection. Additionally, co-injection of non-radioactive **QCP02** with [^{111}In]**QCP02** significantly reduced radiotracer uptake in U87 xenografts (7.63 ± 1.39 vs 0.55 ± 0.23% ID/g; $P < 0.0001$), establishing the specific binding of the radiotracer to FAP. Altogether, the results establish the ability of **QCP01** and [^{111}In]**QCP02** to bind FAP *in vivo* and clear rapidly from non-target tissues.

FAP provides a distinct marker of activated fibroblasts and is a key regulator and driver of the TME. Activated fibroblasts, also known as CAFs, are one of the largest components of the TME in many cancers. They promote tumorigenesis by secreting pro-inflammatory cytokines and growth factors, including the vascular endothelial growth factor, as well as by remodeling the ECM to enhance tumor cell invasion[42,43]. Additionally, FAP expression is not limited to fibroblasts but can also be seen on tumor epithelial cells[44], which can then support and accelerate tumorigenesis. This phenomenon has been demonstrated clinically, where FAP expression levels have been linked to poor outcomes[47–49]. Mounting evidence for the role of FAP in cancer explains the rapid adoption of small-molecule agents that target FAP into clinical studies.

The rapidity with which preclinical studies progressed to the clinic may suggest that limited medicinal chemistry was undertaken to optimize the agents that are being utilized in patients. Indeed, a number of new agents have been developed and studied preclinically, which may have superior characteristics to the most commonly used clinical compound[60,67]. First, we provided a comprehensive summary of FAP-expressing cells and tissues from the CCLE and TCGA and chose six lines to test our compounds.

Here, we report the syntheses, FAP binding affinities and specificities, and *in vivo* uptake of two new imaging agents targeting FAP in an experimental model. Novel aspects of this work include our co-development of an optical agent, **QCP01**, to examine the dynamics of FAP binding by this compound both *in vitro* and *in vivo*. Despite introduction of the bulky optical moiety to the (4-quinolinoyl)-glycyl-2-cyanopyrrolidine scaffold, **QCP01** retained FAP inhibitory capacity. The SPECT-CT imaging agent, [^{111}In]**QCP02**, enabled us to investigate FAP expression and target selectivity in mice quantitatively. The use of a common FAP-binding intermediate having a reactive amine moiety permits the ready conjugation of any number of amine reactive optical dyes, metal chelating groups, or radiolabeled prosthetic groups for SPECT/PET imaging and theranostic applications.

Using **QCP01** and [^{111}In]**QCP02**, we demonstrated the ability of our agents to target FAP on the surface of known FAP-positive cancer cells *in vitro* with minimal non-specific binding in FAP-negative cancer cells. Even within FAP-positive cell lines, we saw distinct differences in binding of FAP (Figure 2-4A), further illustrating the heterogeneity of FAP expression within highly expressing cells and the sensitivity of our compounds for detecting these differences. To explore further the dynamics of FAP in cancer, we employed a tumor xenograft model with two cancer cell lines, FAP-positive U87 and FAP-negative PC3, in NOD/SCID mice. When we expanded these studies to *in vivo* imaging and biodistribution, we saw that the agents behaved similarly with favorable biodistribution and retained uptake in the FAP-positive xenograft at various imaging time points.

Since FAP shares over 50 and 70% similarity in the sequence and catalytic region, respectively, with DPP-IV, most inhibitors of FAP also bind to DPP-IV[40]. Due to the ubiquitous expression of DPP-IV in normal human tissues[40], it was important to establish the specificity of imaging compounds of this class for FAP over DPP-IV. The specific binding of **QCP01** and [^{111}In]**QCP02** for FAP was verified in cellular studies of various cell lines with differing FAP expression. *In vitro* blocking studies also showed the specificity of **QCP01** for FAP over DPP-IV. In blocking studies, there was no change in binding of **QCP01** when only DPP-IV binding was inhibited. In contrast, binding of **QCP01** was blocked when DPP-IV and FAP were both inhibited. This was further supported in the biodistribution study for [^{111}In]**QCP02**. This study showed that when a blocking dose was administered, no binding was observed in the FAP-positive xenograft, ruling out a substantial role for flow-mediated phenomena accounting for the observed activity within FAP-expressing tumors.

Although both **QCP01** and [$^{113/115}$In]**QCP02** have low-nanomolar inhibition, they differ by about 1 order of magnitude, with the former demonstrating greater inhibitory capacity. There were distinct differences between **QCP01** and [^{111}In]**QCP02** *in vivo*. While both compounds demonstrated uptake in the FAP-positive U87 xenograft at early time points and clearance through the gastrointestinal tract, **QCP01** showed more non-specific uptake than [^{111}In]**QCP02**. These differences in uptake could be attributed to factors besides binding affinity, such as molecular weight and lipophilicity.

In comparison to other FAP-targeted imaging agents, [^{111}In]**QCP02** demonstrated both higher tumor and normal organ uptake relative to **FAPI-02** and **FAPI-04**, which were evaluated in stably transfected FAP cell lines[55]. [^{111}In]**QCP02** also appears to have significantly higher uptake in the tumor and lower uptake in the kidney than another recently reported small-molecule agent, although again in different cell line xenografts[60]. The optimum imaging time for [^{111}In]**QCP02** to make the best use of its high tumor uptake would appear to be ~30 min post-injection in our mouse xenograft models, with relatively decreased tumor-to-normal-organ uptake after 3 h.

Because of an improved understanding of the TME in tumor progression and resistance to therapy[68], there has been a paradigm shift in cancer treatment to focus on targeting the tumor stroma and other aspects of the TME in addition to the cancer cells themselves[43,69]. FAP can promote generation of regulatory T-cells and tumor-associated macrophages, contributing to the immunosuppressive tumor environment[70]. Active monitoring of targeted treatments with FAP imaging agents may promote optimal cancer management strategies.

Conclusions

We prepared two high-affinity FAP-targeted agents, **QCP01** and [^{111}In]**QCP02**, and demonstrated their specificity for FAP *in vitro* and *in vivo*. We initially tested them *in cellulo* based on the variable expression of FAP noted in a variety of cell lines and tissues according to the CCLE and TCGA. In mouse xenograft models with variable FAP expressions, both agents exhibited significant retention in FAP-positive tumors. The favorable pharmacokinetics and biodistribution observed with these agents provided FAP-specific images by 30 min after injection and also allow for imaging at later time points. The results provide impetus for pursuit of **QCP01**, [^{111}In]**QCP02**, and analogues for clinical use.

Experimental Section

General Procedures

Reagents and solvents were purchased from commercial sources and were of analytical or HPLC grade, which were used as received. 6-Hydroxyquinoline-4-carboxylic acid was purchased from Sigma-Aldrich (St. Louis, MO). Methyl glycinate hydrochloride, 2-(1*H*-benzotriazole-1-yl)-1,1,3,3-tetramethyluronium hexafluorophosphate (HBTU), 1-hydroxylbenzotriazole monohydrate (HOBt), and diisopropylethylamine were purchased from Chem Impex International Inc. (Wood Dale, IL). 3-(Boc-amino) propyl bromide and (*S*)-pyrrolidine-2-carbonitrile hydrochloride were purchased from Combi-Blocks (San Diego, CA). 2-[1,4,7,10-Tetraazacyclododecane-4,7,10-tris(*t*-butyl acetate)]-pentanedioic acid-1-*tert*-butyl ester [DOTAGA-tetra(*tert*-Bu ester); DOTA-GA] was purchased from Macrocyclics (Dallas, TX). IRDye 800CW NHS ester was purchased from LI-COR Biosciences

(Lincoln, NE). Reaction progress was monitored by analytical thin-layer chromatography and was performed on Analtech Uniplate 0.25 mm silica gel 60 F254 plates. Visualization was accomplished with ultraviolet (UV) light. Purification of reaction products was carried out by reverse-phase chromatography using a C18 cartridge (Silicycle, Canada) on a Biotage IsoleraOne flash purification system. HPLC purification was performed using a Phenomenex C18 Luna 10 × 250 mm^2 column on an Agilent Technologies 1260 Infinity semi-preparative HPLC System (Wilmington, DE). HPLC purification of the ^{111}In-labeled compound was performed on an Agilent PrepStar system (Santa Clara, CA), equipped with an Agilent ProStar 325 UV–vis variable wavelength detector and a Bioscan Flow-count in-line radioactivity detector (Washington, DC), with all controlled by OpenLAB software. Proton nuclear magnetic resonance spectra (^{1}H NMR) were recorded on a Bruker UltraShield 400 MHz instrument and are reported in ppm using the solvent as an internal standard ($CDCl_3$ at 7.26 ppm and CD_3OD at 3.31 ppm). Data are reported as app = apparent, br = broad, s = singlet, d = doublet, t = triplet, q = quartet, m = multiplet, and comp = complex, and coupling constant(s) are reported in Hz. Proton-decoupled carbon nuclear magnetic resonance spectra (^{13}C NMR) were recorded on a Bruker UltraShield 400 MHz instrument and are reported in ppm using the solvent as an internal standard ($CDCl_3$ at 77.0 ppm and CD_3OD at 49.00 ppm). Low-resolution electrospray ionization-mass spectrometry (ESI-MS) data were obtained using an Agilent Technologies 1260 series LCMS Single Quad System connected to a variable wavelength detector. High-resolution mass spectra were recorded at the University of Notre Dame Mass Spectrometry and Proteomics Facility (Notre Dame, IN) using ESI by direct infusion on a Bruker microTOF-II.

Methyl (6-Hydroxyquinoline-4-carbonyl)glycinate (4)

6-Hydroxyquinoline-4-carboxylic acid (**3**) (210 mg, 1.1 mmol), methyl glycinate HCl salt (143 mg, 1.1 mmol), HBTU (420 mg, 1.1 mmol), and HOBt (170 mg, 1.1 mmol) were dissolved in 12 mL of dry dimethylformamide (DMF). To the solution, *N*,*N*-diisopropylethylamine (DIPEA) (0.77 mL, 4.4 mmol) was added. The reaction mixture was stirred at room temperature (RT) for 6 h. After the solvent was removed under vacuum, the mixture was loaded onto a 25 g C18 cartridge and the product was purified with a MeCN/water/trifluoroacetic acid (TFA) gradient (0/100/0.1 to 90/10/0.1). After

lyophilization, product **4** was obtained as a yellow powder in a 76% yield (290 mg). ^{1}H NMR (400 MHz, CD_3OD): δ 8.69 (s, 1H), 7.94 (d, *J* = 7.92 Hz, 1H), 7.57–7.51 (m, 3H), 7.42–7.37 (m, 1H), 4.21 (s, 2H), 3.81 (s, 3H). ^{13}C NMR (100 MHz, CD_3OD): δ 172.4, 160.9, 145.1, 143.7, 129.7, 129.4, 128.3, 121.8, 119.6, 112.4, 109.1, 56.8, 44.8. ESI-MS *m*/*z*: calcd for $C_{13}H_{13}N_2O_4$ $[M + H]^+$, 261.3; found, 261.1.

Methyl (6-(3-((*tert*-Butoxycarbonyl)amino)propoxy)quinoline-4-carbonyl)glycinate (5)

Methyl (6-hydroxyquinoline-4-carbonyl)glycinate (**3**) (360 mg, 1.0 mmol) and 3-(Boc-amino) propyl bromide (**4**) (500 mg, 2.1 mmol) were dissolved in 20 mL of DMF. Cs_2CO_3 (1 g, 3.0 mmol) was added to the solution, and the reaction mixture was stirred at RT overnight. After filtration, the solvent was removed under vacuum and the remaining mixture was loaded onto a 25 g C18 cartridge. The product was purified with a MeCN/water/TFA gradient (0/100/0.1 to 90/10/0.1). After lyophilization, 270 mg of product **5** was obtained in a 54% yield. ^{1}H NMR (400 MHz, $CDCl_3$): δ 8.68–8.37 (m, 2H), 8.02 (d, *J* = 9.1 Hz, 1H), 7.80 (s, 1H), 7.72–7.64 (m, 1H), 7.40 (d, *J* = 9.1 Hz, 1H), 4.94 (br s, 1H), 4.41–4.31 (m, 2H), 4.27–4.18 (m, 2H), 3.85 (s, 3H), 3.44–3.30 (m, 2H), 2.13–2.00 (m, 2H), 1.43 (s, 9H). ^{13}C NMR (100 MHz, $CDCl_3$): δ 170.1, 167.2, 158.4, 144.7, 142.3, 128.4, 126.1, 124.7, 119.1, 103.7, 79.5, 60.4, 52.5, 41.4, 37.7, 29.3, 28.4. ESI-MS *m*/*z*: calcd for $C_{21}H_{28}N_3O_6$ $[M + H]^+$, 418.5; found, 418.3.

tert-Butyl(*S*)-(3-((4-((2-(2-cyanopyrrolidin-1-yl)-2-oxoethyl)carbamoyl)quinolin-6-yl)oxy)propyl)carbamate (7)

Compound **5** (110 mg, 0.21 mmol) and LiOH (30 mg, 1.2 mmol) were stirred in 4 mL of H_2O/THF (1/1) for 6 h. After most of the THF was removed under vacuum, the mixture was loaded onto a 25 g C18 cartridge and eluted with a MeCN/water/TFA gradient (0/100/0.1 to 90/10/0.1) to remove the salts. After removal of the solvent and drying, product **6** was obtained and mixed with (*S*)-pyrrolidine-2-carbonitrile (53 mg, 0.4 mmol), HOBt (68 mg, 0.4 mmol), HBTU (152 mg, 0.4 mmol), and DIPEA (0.56 mL, 1.6 mmol) in dry DMF (10 mL). After 6 h, the solvent was removed under vacuum and the crude mixture was loaded onto a 25 g C18 cartridge (Silicycle, Canada). The product was purified

with a MeCN/water/TFA gradient (0/100/0.1 to 90/10/0.1). After lyophilization, 99 mg of **7** was obtained in an 80% yield. ^{1}H NMR (400 MHz, $CDCl_3$): δ 8.73 (s, 1H), 7.95 (d, *J* = 10.2 Hz, 1H), 7.68 (br s, 1H), 7.63–7.56 (m, 1H), 7.56–7.48 (m, 1H), 7.38–7.29 (m, 1H), 5.27 (br s, 1H), 4.84–4.72 (m, 1H), 4.46–4.35 (m, 1H), 4.33–4.20 (m, 1H), 4.17–4.09 (m, 2H), 3.78–3.64 (m, 1H), 3.59–3.46 (m, 1H), 3.36 (s, 2H), 2.38–2.17 (m, 4H), 1.42 (s, 9H), 1.35–1.27 (m, 2H). ^{13}C NMR (100 MHz, $CDCl_3$): δ 167.6, 167.5, 157.9, 156.2, 146.3, 130.2, 125.7, 123.7, 119.3, 118.0, 103.3, 79.0, 65.9, 46.8, 45.7, 42.2, 37.6, 29.8, 29.3, 28.4, 25.1. ESI-MS *m*/*z*: calcd for $C_{25}H_{32}N_5O_5$ $[M + H]^+$, 482.6; found, 482.3.

1-(6-((3-((4-((2-((*S*)-2-Cyanopyrrolidin-1-yl)-2-oxoethyl)carbamoyl)quinolin-6-yl)oxy)propyl)amino)-6-oxohexyl)-2-((*E*)-2-((*E*)-3-(2-((*E*)-3,3-dimethyl-5-(trioxidaneylthio)-1-(4-(trioxidaneylthio)butyl)indolin-2-ylidene)ethylidene)-2-(4-(trioxidaneylthio)phenoxy)cyclohex-1-en-1-yl)vinyl)-3,3-dimethyl-3*H*-indol-1-ium-5-sulfonate (**QCP01**)

Compound **7** (1 mg, 1.7 μmol) was treated with a 1 mL solution of TFA/methylene chloride (1/1) for 2 h. The solvent was removed under vacuum, and the remaining material was redissolved in 0.5 mL of DMF. To the solution, LI-COR IRdye 800CW-NHS ester (0.5 mg, 0.43 μmol) and DIPEA (10 μL) were added. After 2 h at ambient temperature, the solvent was removed and the product was purified by semi-preparative HPLC. 0.5 mg of the product was obtained in an 81% yield. HPLC conditions: Phenomenex, C18 Luna, 10μ, 10 mm × 250 mm column; gradient 90/10/0.1 to 80/20/0.1 water/acetonitrile/TFA over 15 min at a flow of 3 mL/min. The product was eluted at 10.1 min. ESI-MS *m*/*z*: calcd for $C_{66}H_{76}N_7O_{17}S_4^+$ $[M + H]^+$, 1366.4; found, 1366.8.

2,2′,2″-(10-(1-Carboxy-4-((3-((4-((2-((*S*)-2-cyanopyrrolidin-1-yl)-2-oxoethyl)carbamoyl)quinolin-6-yl)oxy)propyl)amino)-4-oxobutyl)-1,4,7,10-tetraazacyclododecane-1,4,7-triyl)triacetic Acid (**QCP02**)

Compound **7** (15 mg, 31.3 μmol) was treated with a 1 mL solution of TFA/methylene chloride (1/1) for 1 h. The solvent was removed under vacuum, and the remaining material was re-dissolved in 0.5 mL of DMF. To the solution, DIPEA (27 μL, 156.5 μmol) was added, followed by dropwise addition of

a solution of DOTA-GA(*t*-Bu)$_4$-NHS (25 mg, 31.3 µL) in 0.5 mL of DMF. The reaction mixture was stirred for 4 h at ambient temperature and then concentrated under vacuum. The *tert*-Bu-protected intermediate was deprotected *in situ* without further purification using a 1 mL mixture of TFA, H_2O, and triethylsilane (TES) (95:2.5:2.5). The reaction mixture was then concentrated and purified by semi-preparative HPLC to afford the product as a white solid (8.5 mg, 33% yield). HPLC conditions: Phenomenex, C18 Luna, 10µ, 10 mm × 250 mm column; mobile phase 95/5/0.1 to 75/25/0.1% water/acetonitrile/TFA over 20 min; flow 5 mL/min. **QCP02** was eluted at 11.8 min. HRMS (ESI) *m*/*z*: calcd for $C_{39}H_{54}N_9O_{12}$ $[M + H]^+$, 840.3892; found, 840.3885.

$^{113/115}$Indium(III) 2,2′,2″-(10-(1-Carboxy-4-((3-((4-((2-((*S*)-2-cyanopyrrolidin-1-yl)-2-oxoethyl) carbamoyl)quinolin-6-yl)oxy)propyl) amino)-4-oxobutyl)-1,4,7,10-tetraazacyclododecane-1,4,7-triyl) Triacetate ([In]**QCP02**)

To a solution of 2 mg (2.4 µmol) of **QCP02** in 1 mL of aqueous 0.2 M sodium acetate, a solution of $In(NO_3)_3$ (1.4 mg, 4.6 µmol) in 0.5 mL of water was added and warmed in a 60 °C bath for 30 min. After cooling to ambient temperature, the mixture was purified by semi-preparative HPLC. The product was obtained as a white solid (1.8 mg, 79% yield). ESI-MS *m*/*z*: calcd for $C_{39}H_{51}N_9O_{12}In$ $[M + H]^+$, 952.7; found, 952.5. HPLC conditions: Phenomenex, C18 Luna, 10µ, 10 mm × 250 mm column; mobile phase 95/5/0.1 to 75/25/0.1 water/acetonitrile/TFA over 20 min; flow 5 mL/min. [In]**QCP02** was eluted at 14.0 min.

[^{111}In]2,2′,2″-(10-(1-Carboxy-4-((3-((4-((2-((*S*)-2-cyanopyrrolidin-1-yl)-2-oxoethyl)carbamoyl) quinolin-6-yl)oxy)propyl) amino)-4-oxobutyl)-1,4,7,10-tetraazacyclododecane-1,4,7-triyl)triacetate ([^{111}In]**QCP02**)

Briefly, a 20 µg **QCP02** solution in 20 µL of 0.2 M NaOAc was added to 10 µL of 170.2 MBq $^{111}InCl_3$ solution in 0.05 N HCl and adjusted to a final pH of 5.5–6. The mixture was heated in a water bath at 70 °C for 30 min and then diluted with 200 µL of water for HPLC purification. The solution was purified using a Phenomenex, C18 Luna, 5µ, 4.6 mm × 250 mm column (Torrance, CA) with a flow rate of 0.6 mL/min with water (0.1% TFA) (A) and MeCN (0.1% TFA) (B) as the eluting solvents. An

isocratic solution of 88% A and 12% B was utilized for purification, resulting in [^{111}In]**QCP02**, eluting at 19.3 min, followed by **QCP02** at 21.3 min. 118.4 MBq of the labeled compound was obtained in yields between 69 and 74%. The radiochemical purity was >95% as measured by HPLC. The obtained radioactivity was diluted with 20 mL of water and loaded onto activated Sep-Pak (WAT020515, Waters, Milford, MA). After the Sep-Pak was washed with 10 mL of water, [^{111}In]**QCP02** was eluted with 1.5 mL of ethanol. The ethanol was evaporated under a gentle stream of nitrogen (to a total volume of <50 µL) and diluted with saline to reduce the ethanol percentage to <10% for imaging and biodistribution studies.

FAP Inhibition Assay

The inhibitory activities of **QCP01** and [$^{113/115}$In]**QCP02** were determined using a fluorogenic FAP Assay Kit (BPS Bioscience, San Diego, CA). Briefly, the test compound (**QCP01**: 50–0.39 nM, [$^{113/115}$In]**QCP02**: 500–0.23 nM), the reactive substrate, and human recombinant FAP were loaded into a 96-well plate to initiate the enzymatic reaction. The reaction was left for 10 min at RT before the fluorescence was measured for 0.1 s per well with a VICTOR^3 V multilabel plate reader (PerkinElmer Inc., Waltham, MA) at an excitation wavelength of 355 nm and an emission wavelength of 460 nm. Data were normalized, and semi-log inhibition curves were generated in order to determine the half-maximal inhibitory concentrations (IC_{50} values) and subsequent enzyme inhibition constants (K_i) using the Cheng–Prusoff conversion[71]. Generation of semi-log inhibition curves and IC_{50} values was performed using GraphPad Prism software (San Diego, CA).

Analysis of the CCLE Database and TCGA Data

Messenger RNA (mRNA) expression data of FAP in human cell lines, generated by RNAseq analysis, were downloaded (9/17/19) from the CCLE database[72] and sorted by cell line “type”. All samples with no type or FAP measurement were excluded. *Z*-Scores were calculated using all cell lines as a reference, and samples were grouped by cancer cell type for visualization. To evaluate FAP expression in normal tissues and human tumors, pan-cancer normalized FAP RNAseq (Illumina HiSeq) gene expressions in normal tissues and primary tumors (downloaded 9/20/19) were

downloaded (10/22/19) for 18 TCGA cohorts and 32 TCGA cohorts, respectively, using the UCSC Xena platform[73].

Cell Lines

U87, SKMEL24, and NCIH2228 cell lines were identified from the CCLE as having high levels of FAP expression [FAP-positive (+)], whereas PC3, NCIH226, and HCT116 cells expressed very low levels of FAP [FAP-negative (−)]. FAP expression was further confirmed by flow cytometry with 10 µL of an allophycocyanin-conjugated anti-FAP antibody (Clone #427819, R&D Systems, Minneapolis, MN) and quantitative real-time polymerase chain reaction. All cell lines were purchased from American Type Culture Collection (ATCC, Manassas, VA).

Binding of imaging agents to FAP was assessed in six human cancer cell lines of different cancer types: glioblastoma (U87), melanoma (SKMEL24), prostate (PC3), NSCLC (NCIH2228), colorectal carcinoma (HCT116), and lung squamous cell carcinoma (NCIH226).

U87 cells were maintained in the *minimum essential medium* (MEM) (Corning Cellgro, Manassas, VA), containing 10% fetal bovine serum (FBS) (Sigma-Aldrich, St. Louis, MO) and 1% penicillin–streptomycin (Corning Cellgro), supplemented with sodium bicarbonate (Corning Cellgro), sodium pyruvate (Gibco, Gaithersburg, MD), and MEM non-essential amino acids (Gibco). SKMEL24 cells were maintained in MEM, containing 15% FBS and 1% penicillin–streptomycin, supplemented with sodium bicarbonate, sodium pyruvate, and MEM non-essential amino acids. PC3 cells were grown in Ham's F-12K medium (Corning Cellgro), supplemented with 10% FBS and 1% penicillin–streptomycin. NCIH2228, NCIH226, and HCT116 cells were cultured in the RPMI 1640 medium (Corning Cellgro), supplemented with 10% FBS and 1% penicillin–streptomycin. Cell cultures were maintained at 37 °C and 5% carbon dioxide (CO_2) in a humidified incubator.

Cellular Uptake Studies

For *in vitro* studies, cells were detached using 0.05% trypsin (Corning), re-suspended in 1 million cell aliquots in the binding buffer (1× PBS with 2 mM EDTA and 0.5% FBS), and incubated with various

concentrations (range: 50–0.78 nM) of **QCP01** for 1 h in the incubator. To assess specific uptake of **QCP01**, cells were preblocked with an FAP- and DPP-IV-specific inhibitor, Val-boroPro (Millipore Sigma, Burlington, MA), or a DPP-IV-specific inhibitor, sitagliptin (Santa Cruz Biotechnology, Inc., Dallas, TX), at various concentrations (range: 10^{-10} to 10^{-4} M). This was followed by incubation with 25 nM **QCP01** in the binding buffer for 1 h at 37 °C, and cellular uptake was terminated by washing cells with ice cold PBS (1×) three times. Cells were re-suspended in the binding buffer and transferred to a 96-well plate for imaging. Images were obtained on the LI-COR Pearl Impulse Imager (Lincoln, NE) using an excitation wavelength of 785 nm and detection of the emission wavelength at 800 nm. Images were analyzed using LI-COR Pearl Impulse Software (Version 2.0), and the fluorescence intensity was corrected for the background signal and normalized to the well area.

Cellular uptake of [^{111}In]**QCP02** was assessed by incubating cell aliquots (1 million) with 0.037 MBq [^{111}In]**QCP02** in saline for 30 min at 37 °C. Cells were washed three times with cold PBS (1×), and the radioactivity of the cell pellets was measured with a 1282 CompuGamma CS gamma well counter (Pharmacia/LKB Nuclear, Inc., Gaithersberg, MD). The cellular uptake is presented as a percent of incubated activity measured using sample aliquots. All cellular uptake and binding studies were performed in triplicate and repeated three times.

Mouse Xenograft Models

Animal studies were performed according to protocols approved by the Johns Hopkins University Animal Use and Care Committee. Male NOD/SCID mice, 6–8 weeks old, were purchased from the Johns Hopkins Immune Compromised Animal Core (Baltimore, MD). NOD/SCID mice were subcutaneously inoculated in the upper left and right flanks with 1 million FAP-positive U87 and FAP-negative PC3 cells in Hank's balanced salt solution (HBSS), respectively. Mice were monitored for tumor size and used for imaging or biodistribution when the size of the tumors reached 100–300 mm^3.

Small-Animal NIRF Imaging

NIRF images were obtained on the LI-COR Pearl Impulse Imager using an excitation wavelength of 785 nm and a detection wavelength of 800 nm. Mice utilized for imaging studies were anesthetized with 3% isoflurane (v/v) and maintained at 1.5% isoflurane for the imaging procedure. NOD/SCID mice bearing U87 and PC3 tumor xenografts were injected with 5 nmol of **QCP01***via* the tail vein, and images were obtained at 0.5, 1.5, 2.5, 5, 24, and 48 h post injection. Mice were sacrificed at various time points, and whole body images were obtained. Following this, organs of interest were harvested and imaged *ex vivo* on a Petri dish. Data were displayed and analyzed using LI-COR Pearl Impulse Software (Version 2.0).

Small-Animal SPECT-CT Imaging

For imaging studies, mice were induced with 3% isoflurane anesthesia and maintained at 1.5%. After mice were injected with 7.4 MBq [^{111}In]**QCP02** in 200 µL of saline, SPECT-CT imaging was carried out using a CT-equipped Gamma Medica-Ideas SPECT scanner (Northridge, CA) at the designated time points (1, 3, 6, 10, and 28 h) after [^{111}In]**QCP02** injection. A CT scan was performed at the end of each SPECT scan for anatomic co-registration. Obtained data sets were reconstructed using the provided Gamma Medica-Ideas software for final data visualization. Volume-rendered images were prepared using Amira 5.3.3 software (Visage Imaging, Inc., San Diego, CA).

Biodistribution

NOD/SCID mice bearing U87 and PC3 tumor xenografts were injected *via* the tail vein with 0.37 MBq [^{111}In]**QCP02** in 200 µL of saline. At 5 min, 30 min, 1 h, 3 h, 6 h, 10 h, and 28 h post injection, mice (n = 4) were sacrificed by CO_2 asphyxiation and blood was immediately collected by cardiac puncture. Additionally, the heart, lungs, liver, stomach, pancreas, spleen, fat, kidney, small intestine, large intestine, bladder, muscle, femur, and U87 and PC3 xenografts were collected for analysis. Each tissue was weighed, and the radioactivity was measured using an automated gamma counter. Radioactivity measurements were corrected for decay and compared with samples of a standard dilution of the initial dose to calculate the percentage injected dose per gram of tissue (% ID/g). For

blocking studies, mice (n = 4) were co-injected with non-radiolabeled **QCP02** (50 µg per mouse) and 0.37 MBq [^{111}In]**QCP02** in 200 µL of saline *via* the tail vein. At 6 h post injection, mice were sacrificed, tissues were collected, and the radioactivity was measured with the gamma counter.

Data Analysis

Data are expressed as mean ± standard deviation. Prism software (GraphPAD, San Diego, CA) was used for analysis, and the statistical significance was calculated using a two-tailed Student's *t*-test. A *P*-value <0.05 was considered significant.

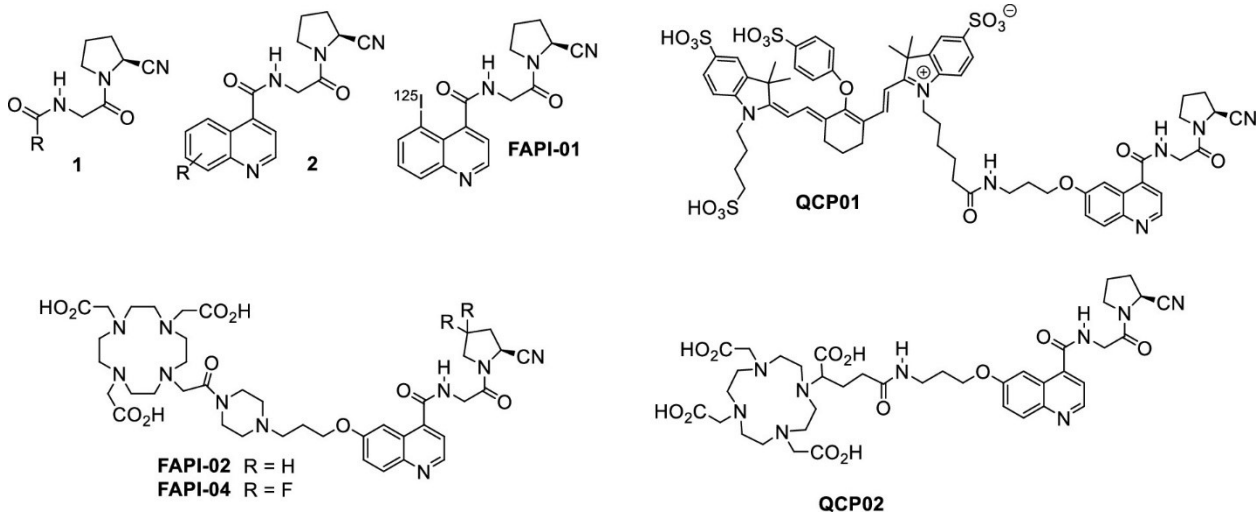

Figure 2-1. FAP Inhibitors

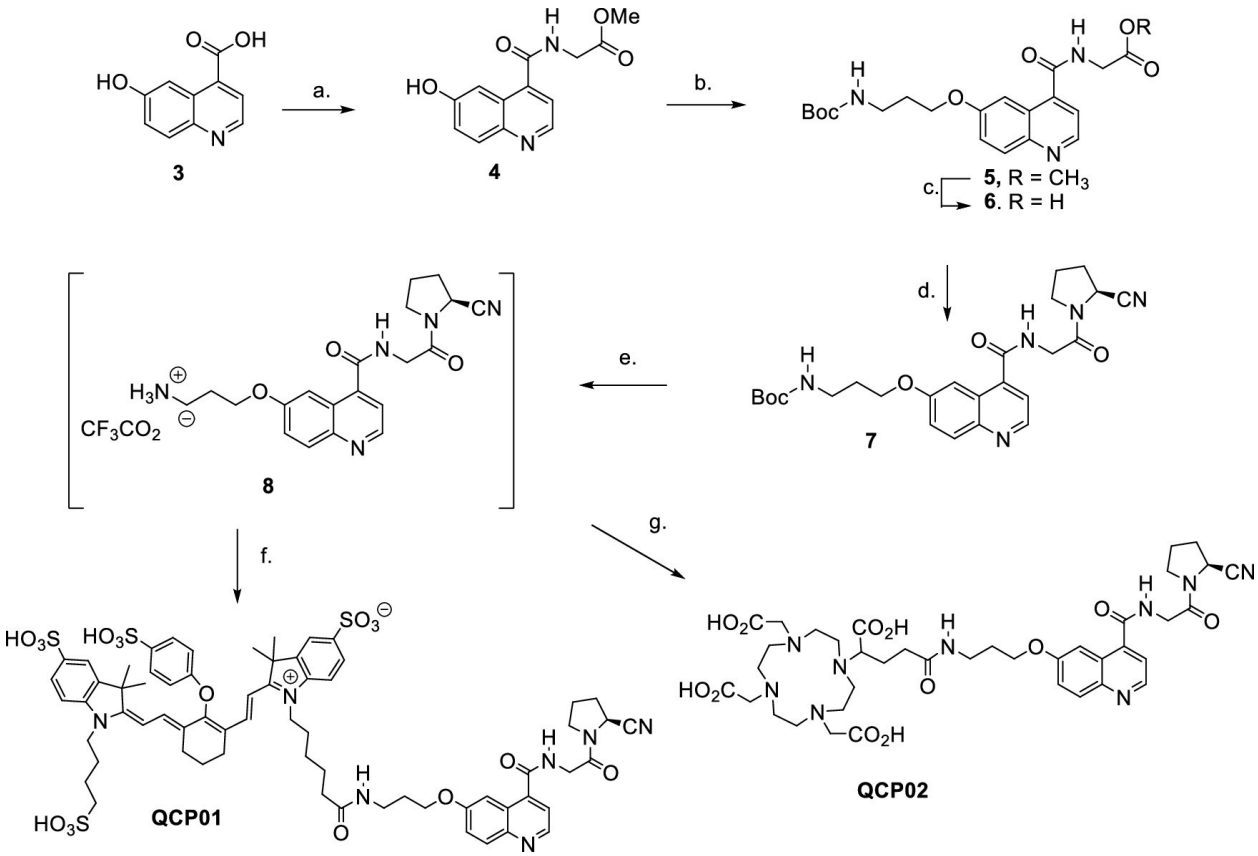

Figure 2-2. Chemical Synthesis of **QCP01** and **QCP02**[a]

[a]Reagents and conditions: (a) glycine methyl ester hydrochloride, HOBt, HBTU, $^{i}Pr_2NEt$, DMF, RT, 6 h, 76%; (b) 3-(Boc-amino) propyl bromide, Cs_2CO_3, DMF, RT, 16 h, 54%; (c) LiOH, H_2O/THF, RT, 6 h, 99%; (d) (*S*)-pyrrolidine-2-carbonitrile hydrochloride, HOBt, HBTU, $^{i}Pr_2NEt$, DMF, RT, 6 h, 80%; (e) TFA/CH_2Cl_2, RT, 1 h; (f) IRDye 800CW-NHS ester, $^{i}Pr_2NEt$, DMF, RT, 2 h, 81% (total yield e and f); (g) 1. DOTA-GA(*t*-Bu)$_4$-NHS, $^{i}Pr_2NEt$, DMF, RT, 4 h, 2. TFA/H_2O/TES, RT, 1 h, 35%.

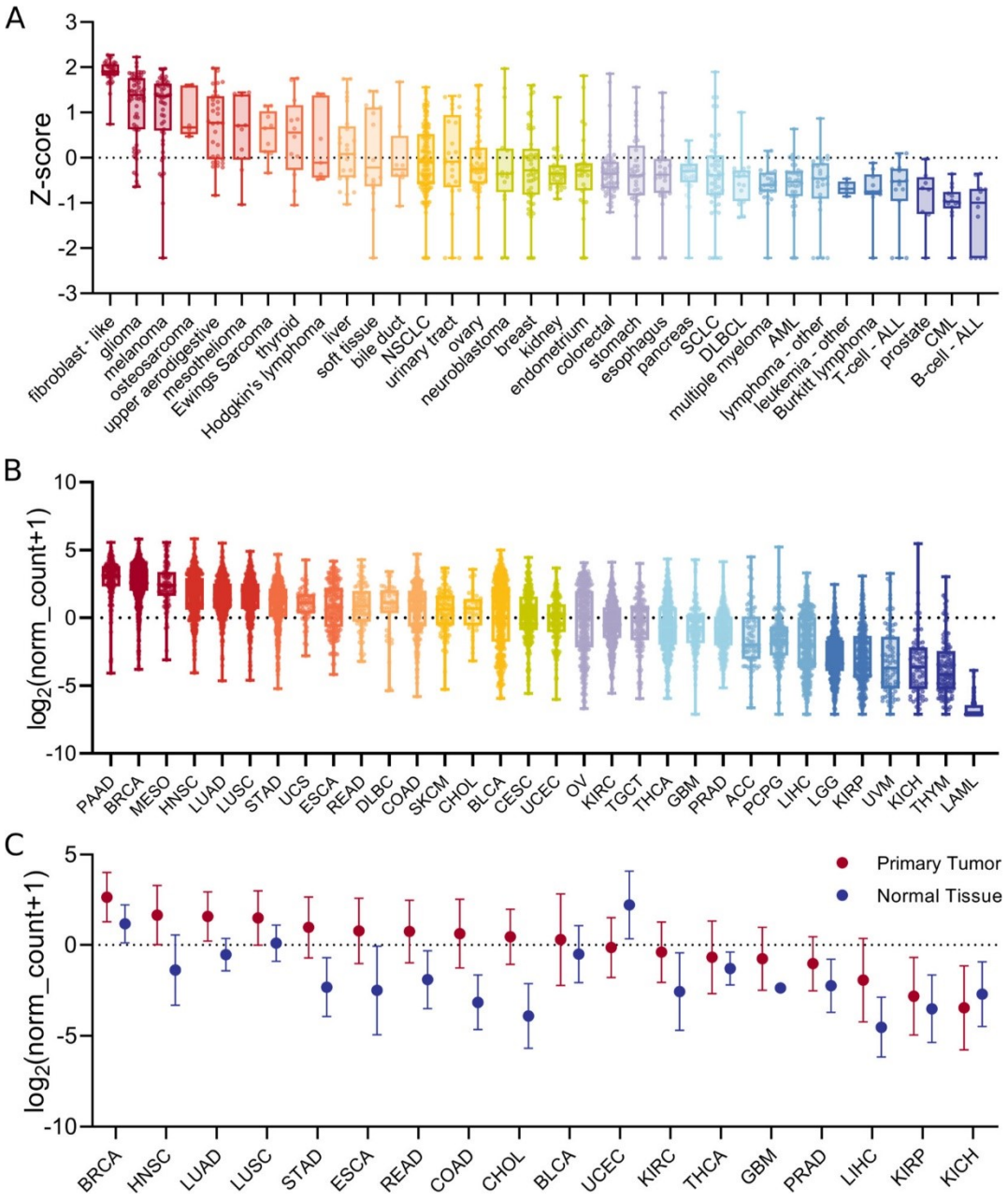

Figure 2-3. FAP expression in human cancers.

FAP mRNA expression in human cancer cell lines from the CCLE (A) and in human primary tumors from TCGA (B) was analyzed. FAP mRNA expression in primary tumors and normal tissues from TCGA data was also analyzed (C); NSCLC = non-small-cell lung cancer; SCLC = small-cell lung cancer; DLBCL = diffuse large B-cell lymphoma; AML = acute myeloid leukemia; CML = chronic myelogenous leukemia; PAAD = pancreatic cancer; BRCA = breast cancer; MESO = mesothelioma; HNSC = head and neck cancer; LUAD = lung adenocarcinoma; LUSC = lung squamous cell carcinoma; STAD = stomach cancer; UCS = uterine carcinosarcoma; ESCA = esophageal cancer; READ = rectal cancer; DLBC = large-B-cell lymphoma; COAD = colon cancer; SKCM = melanoma; CHOL = bile duct cancer; BLCA = bladder cancer; CESC =

cervical cancer; UCEC = endometrioid cancer; OV = ovarian cancer; KIRC = kidney clear cell carcinoma; TGCT = testicular cancer; THCA = thyroid cancer; GBM = glioblastoma; PRAD = prostate cancer; ACC = adrenocortical cancer; PCPG = pheochomocytoma; LIHC = liver cancer; LGG = lower-grade glioma; KIRP = kidney papillary cell carcinoma; UVM = ocular melanomas; KICH = kidney chromophobe; THYM = thymoma; LAML = acute myeloid leukemia.

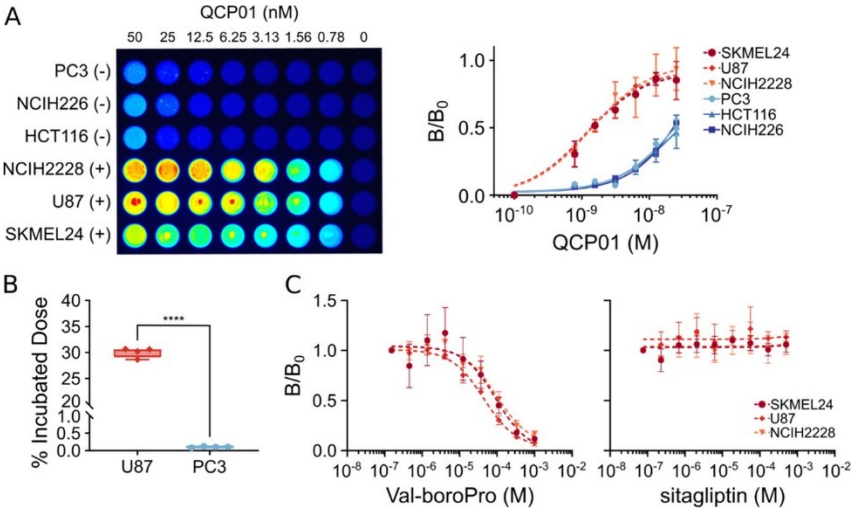

Figure 2-4. *In vitro* binding and specificity of **QCP01** and [^{111}In]**QCP02**.

(A) Cells incubated with various concentrations (range: 50–0.78 nM) of **QCP01** were imaged with the LI-COR Pearl Impulse Imager to assess binding of the agent in various FAP-positive (+) and FAP-negative (−) cell lines (left). Dose–response curves of **QCP01** binding in FAP-positive cell lines (NCIH2228, U87, and SKMEL24) and FAP-negative cell lines (PC3, NCIH226, and HCT116) were generated (right). (B) Cells were incubated with 0.037 MBq [^{111}In]**QCP02** and were washed with cold phosphate-buffered saline (PBS). The radioactivity of the cell pellets was measured and normalized to the incubated dose; ****, $P < 0.0001$. (C) Cells incubated with 25 nM **QCP01** were incubated with various concentrations of either a DPP-IV and FAP inhibitor, Val-boroPro, or a DPPIV-only inhibitor, sitagliptin. The binding of **QCP01** was measured, and semi-log inhibitor–response curves were generated for both Val-boroPro (left) and sitagliptin (right).

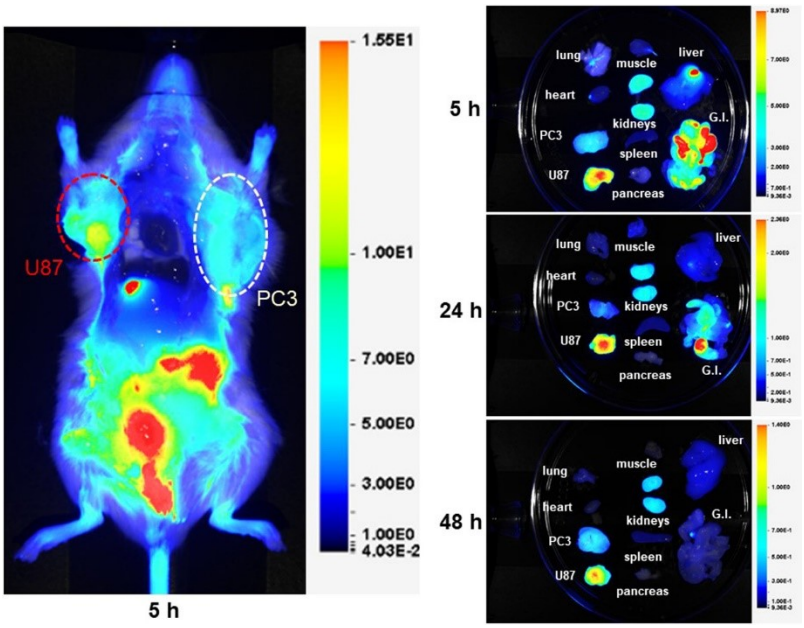

Figure 2-5. NIRF imaging of **QCP01** in a tumor-bearing mouse.

NOD/SCID mice bearing FAP-positive U87 (red) and FAP-negative PC3 (white) tumor xenografts (*n* = 4) were injected with 5 nmol of **QCP01***via* the tail vein, followed by serial NIRF imaging on the LI-COR Pearl Impulse Imager. Representative images of **QCP01** full body (left) distribution at 5 h after injection and organ-specific (right) distribution at 5, 24, and 48 h after injection are shown.

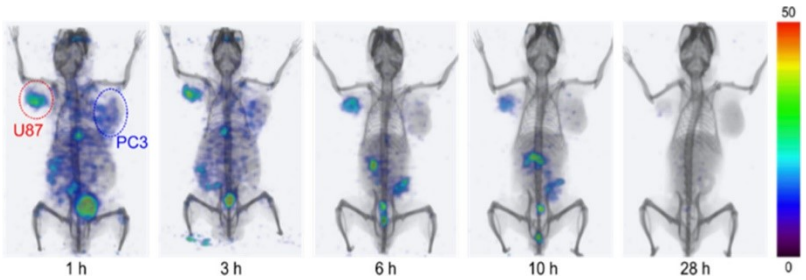

Figure 2-6. Serial SPECT-CT imaging of [^{111}In]**QCP02** in a tumor-bearing mouse.

A NOD/SCID mouse bearing FAP-positive U87 (red) and FAP-negative PC3 (blue) tumor xenografts was injected with 7.4 MBq [^{111}In]**QCP02** *via* the tail vein, followed by serial SPECT-CT imaging. Representative three-dimensional SPECT-CT images at various time points after injection (1, 3, 6, 10, and 28 h) are shown.

(A) HPLC Analysis of **QCP02**

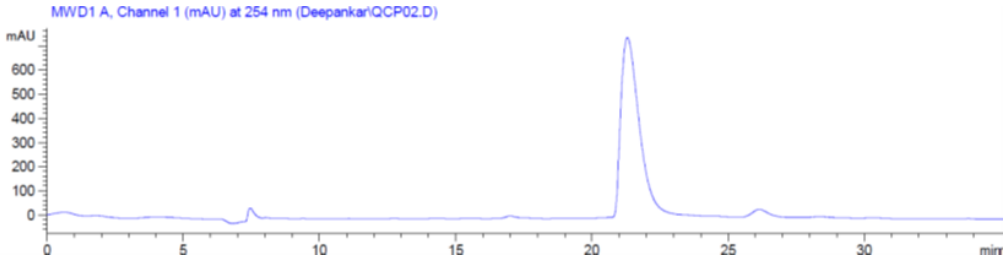

(B) HPLC Analysis of [$^{113/115}$In]**QCP02**

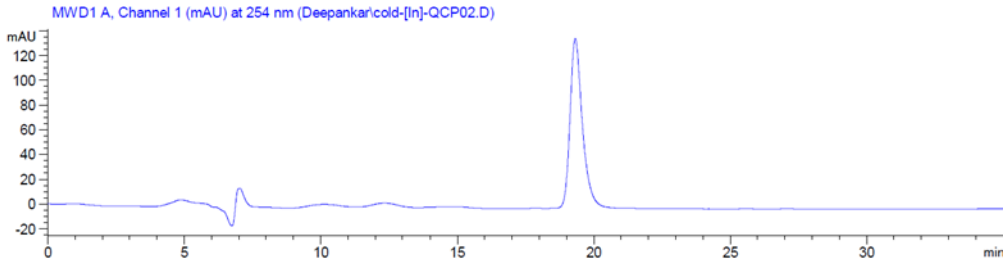

(C) Radio-HPLC analysis of [^{111}In]**QCP02**

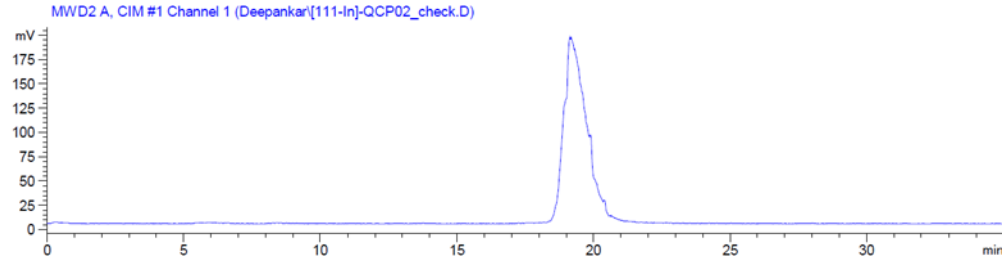

(D) HPLC and radio-HPLC analyses of spiked [$^{113/115}$In]**QCP02** and [^{111}In]**QCP02**

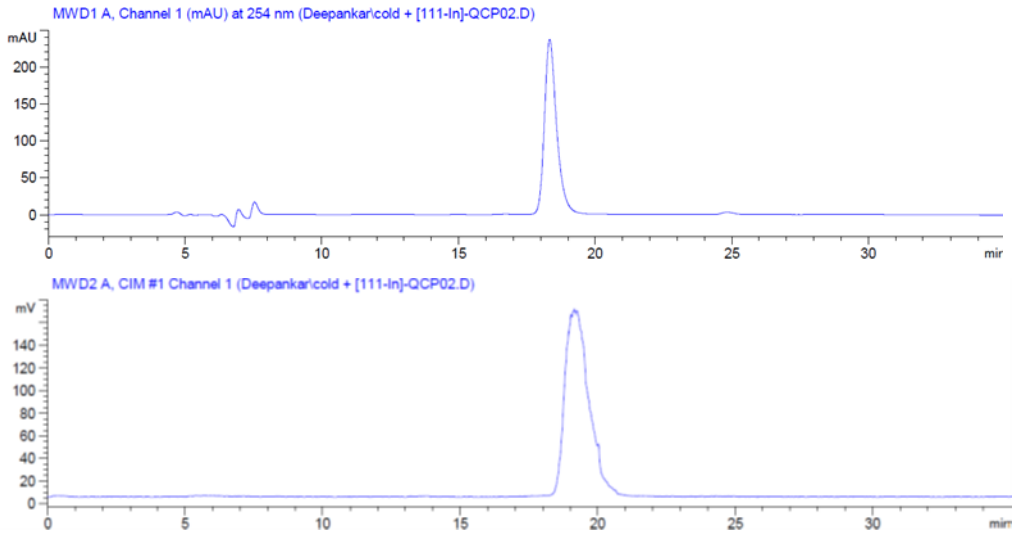

Supplemental Figure 2-1. (A) HPLC chromatogram of **QCP02** and (B) radio-HPLC chromatogram of [^{111}In]**QCP02**. HPLC purification was performed on an Agilent PrepStar system, equipped with a Agilent ProStar 325 UV-vis variable wavelength detector and a Bioscan Flow-count in-line radioactivity detector. The compounds were purified using a Phenomenex, C18 Luna, 5μ, 4.6 mm × 250 mm column with a flow rate of 0.6 mL/min with water (0.1% TFA) (A) and MeCN

(0.1% TFA) (B) as the eluting solvents. An isocratic solution of 88% A and 12% B was used for purification, resulting in **QCP02** eluting at 21.3 min (detection wavelength 254 nm), and [$^{113/115}$In]**QCP02** and/or [^{111}In]**QCP02** eluting at 19.3 min (detection wavelength 254 nm). Free ^{111}In elutes at 5 to 7 min. HPLC purification removes non-chelated precursor, enabling a higher effective specific radioactivity as this precursor also binds to FAP.

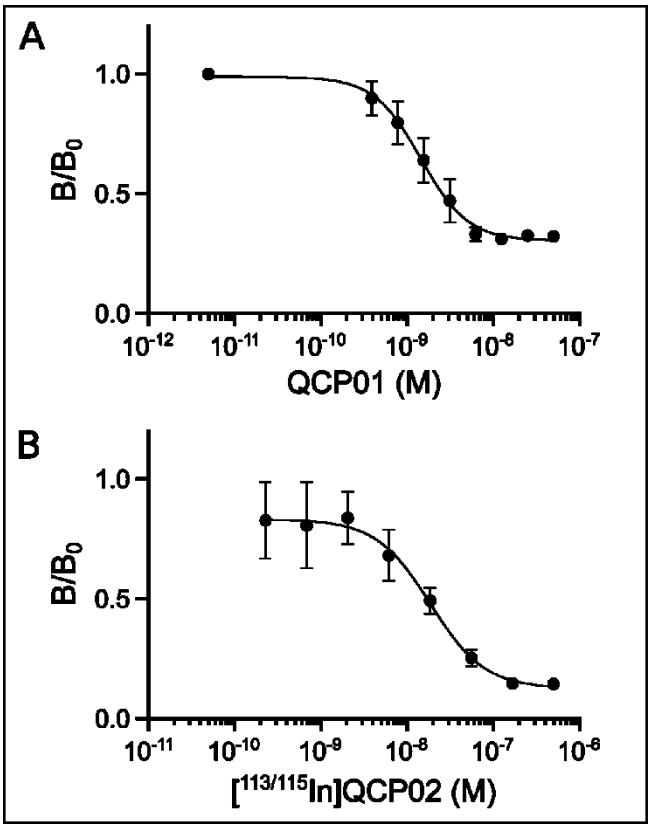

Supplemental Figure 2-2. Inhibitory activity of **QCP01** and [$^{113/115}$In]**QCP02** on human recombinant FAP.

Inhibitory activity of **QCP01** (A) and [$^{113/115}$In]**QCP02** (B) was determined using a fluorogenic FAP assay kit. Semi-log inhibitory curves of **QCP01** and [$^{113/115}$In]**QCP02** activity were generated and the determined Ki values were 1.26 nM (95% Confidence Interval (CI): 0.95 nM – 1.67 nM) and 16.2 nM (95% CI: 10.34 nM – 26.37 nM), respectively.

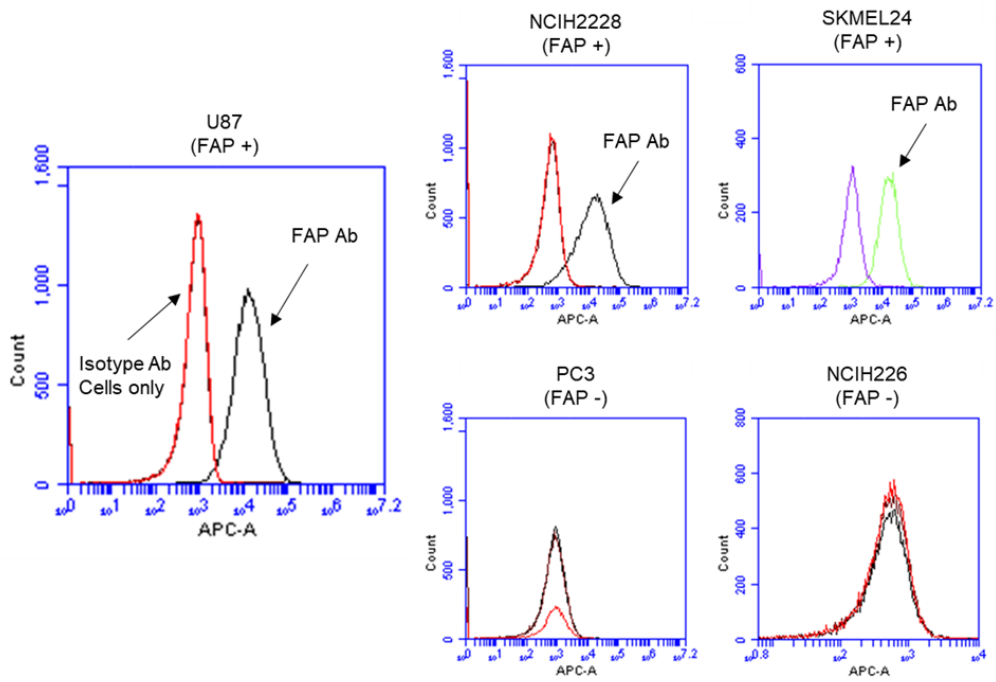

Supplemental Figure 2-3. FAP surface expression in FAP-positive and FAP-negative cell lines.

FAP surface expression on cancer cell lines were confirmed via flow cytometry. Cells incubated with anti-FAP antibody are shown in black (green for SKMEL24 data).

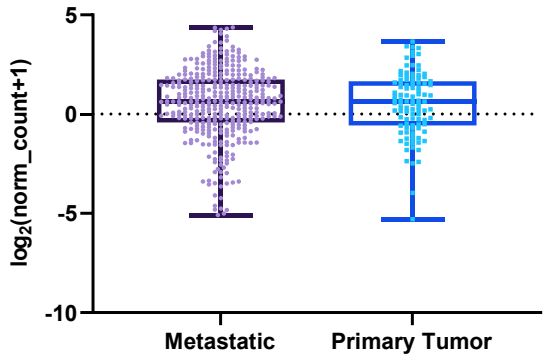

Supplemental Figure 2-4. FAP mRNA expression in metastatic and primary tumor human melanoma (SKCM) samples acquired from TCGA.

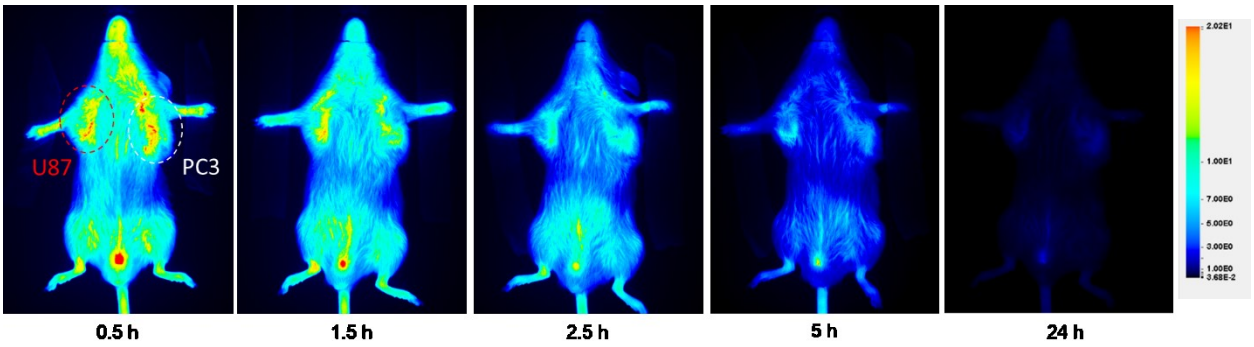

Supplemental Figure 2-5. Serial NIRF imaging of **QCP01** in tumor bearing mice.

NOD/SCID mice bearing FAP-positive U87 (red) and FAP-negative PC3 (white) tumor xenografts (n=4) were injected with 5 nmols of **QCP01** *via* the tail vein followed by serial NIRF-imaging on the LI-COR Pearl Impulse Imager. Representative images of **QCP01** full body distribution at various time points are shown.

Supplemental Table 2-1. *Ex vivo* biodistribution of [^{111}In]**QCP02** in tumor bearing mice**.**

Tissue	5 min (n=4)	30 min (n=4)	1 h (n=4)	3 h (n=4)	6 h (n=4)	6 h+block (n=4)	10 h (n=4)	28 h (n=3)
blood	4.77 ± 0.29	2.65 ± 0.35	2.51 ± 0.38	1.31 ± 0.09	0.73 ± 0.07	0.03 ± 0.01†	0.32 ± 0.04	0.05 ± 0.01
heart	1.95 ± 0.10	0.90 ± 0.51	1.06 ± 0.13	0.75 ± 0.05	0.45 ± 0.04	0.05 ± 0.02†	0.28 ± 0.02	0.11 ± 0.01
lungs	3.05 ± 0.38	1.78 ± 0.46	1.63 ± 0.27	1.00 ± 0.06	0.57 ± 0.10	0.08 ± 0.02†	0.31 ± 0.04	0.08 ± 0.01
liver	1.97 ± 0.13	1.11 ± 0.12	1.18 ± 0.17	1.01 ± 0.11	0.89 ± 0.07	0.37 ± 0.08†	0.80 ± 0.11	0.68 ± 0.10
stomach	1.93 ± 0.13	1.09 ± 0.12	0.95 ± 0.14	0.90 ± 0.41	0.43 ± 0.10	1.13 ± 1.14	0.26 ± 0.06	0.12 ± 0.02
pancreas	4.72 ± 0.69	3.98 ± 0.78	3.37 ± 0.25	2.38 ± 0.71	1.42 ± 0.09	0.08 ± 0.04†	0.69 ± 0.06	0.21 ± 0.04
spleen	1.02 ± 0.22	0.59 ± 0.14	0.72 ± 0.24	0.64 ± 0.03	0.60 ± 0.08	0.10 ± 0.03†	0.49 ± 0.09	0.41 ± 0.01
fat	0.70 ± 0.30	0.39 ± 0.13	0.32 ± 0.07	0.23 ± 0.08	0.26 ± 0.16	0.35 ± 0.60	0.09 ± 0.01	0.03 ± 0.02
kidney	3.90 ± 1.65	1.74 ± 0.12	1.49 ± 0.07	1.20 ± 0.16	0.99 ± 0.14	1.92 ± 0.75	0.70 ± 0.11	0.41 ± 0.08
sm. int.	3.42 ± 0.16	3.33 ± 1.28	1.93 ± 0.53	1.66 ± 0.83	0.68 ± 0.02	0.29 ± 0.32	0.52 ± 0.09	0.22 ± 0.03
lrg. int.	2.88 ± 1.05	1.66 ± 0.35	1.47 ± 0.12	1.65 ± 0.66	0.81 ± 0.21	1.39 ± 0.57	0.51 ± 0.24	0.25 ±0.08
bladder	8.14 ± 5.52	14.72 ± 15.7	11.57 ± 4.91	14.90 ± 11.63	12.93 ± 8.26	5.88 ± 7.79	3.30 ± 2.18	1.26 ± 1.42
muscle	2.30 ± 0.26	1.97 ± 0.35	2.00 ± 0.42	1.89 ± 0.48	0.91 ± 0.24	0.68 ± 1.14	1.47 ± 1.98	0.17 ± 0.07
femur	4.70 ± 0.43	3.95 ± 1.53	4.03 ± 0.73	4.31 ± 0.33	2.18 ± 0.39	1.47 ± 2.70	1.04 ± 0.22	0.58 ± 0.10
U87	11.30 ± 2.71**	18.16 ± 11.67*	16.09 ± 4.17***	9.75 ± 4.16*	7.63 ± 1.39***	0.55 ± 0.23*,†	4.53 ± 1.55*	1.30 ± 0.11***
PC3	4.52 ± 0.17	3.60 ± 1.85	4.12 ± 0.36	3.25 ± 0.40	2.10 ± 0.18	0.20 ± 0.09†	1.26 ± 0.24	0.58 ± 0.03

Results are expressed as mean percentage injected dose per gram (%ID/g) of tissue ± standard deviation.

Comparison of mean %ID/g of PC3 tumor versus U87 tumor (, $P < 0.05$; ** , $P < 0.001$; *** , $P < 0.0001$).

†Comparison of mean %ID/g of tissues at 6 h versus blocking ($P < 0.0001$).

Chapter 3: Examining brain inflammatory processes through kinetic modeling of radiotracers in human clinical studies: A first in human study of [^{18}F]FNDP

Summary:

The focus of this chapter is on the use of [^{18}]FNDP to study the distribution of soluble epoxide hydrolase (sEH) in the human brain. In this first in man study, we utilized positron emission tomography to study the distribution of [^{18}F]FNDP in 7 healthy human subjects. Using PMOD, we were able to use the time activity curves generated for the 10 regions of interest (ROIs) to characterize the binding of [^{18}F]FNDP to sEH using a two-tissue compartment model and Logan graphical analysis. We observed that binding of [^{18}F]FNDP was higher in human cerebellar cortex and thalamus relative to supratentorial cortical regions, aligning with the reported expression of sEH in human brain.

First-in-human neuroimaging of soluble epoxide hydrolase using [18F]FNDP PET

This work has been published and is reprinted here with permission from the *European Journal of Nuclear Medicine and Molecular Imaging.*

Coughlin JM, Slania S, Du Y, Shinehouse LK, Brosnan MK, Azad BB, Holt DP, Fan H, Lesniak WG, Minn I, Rowe SP, Dannals RF, Horti AG, Pomper MG. First-in-human neuroimaging of soluble epoxide hydrolase using [^{18}F]FNDP PET. Eur J Nucl Med Mol Imaging. 2021 Feb 13.

Abstract

Purpose

Soluble epoxide hydrolase (sEH) is an enzyme with putative effect on neuroinflammation through its influence on the homeostasis of polyunsaturated fatty acids and related byproducts. sEH is an enzyme that metabolizes anti-inflammatory epoxy fatty acids to the corresponding, relatively inert 1,2-diols. A high availability or activity of sEH promotes vasoconstriction and inflammation in local tissues that may be linked to neuropsychiatric diseases. We developed [^{18}F]FNDP to study sEH in vivo with positron emission tomography (PET).

Methods

Brain PET using bolus injection of [^{18}F]FNDP followed by emission imaging lasting 90 or 180 min was completed in healthy adults (5 males, 2 females, ages 40–53 years). The kinetic behavior of [^{18}F]FNDP was evaluated using a radiometabolite-corrected arterial plasma input function with compartmental or graphical modeling approaches.

Results

[^{18}F]FNDP PET was without adverse effects. Akaike information criterion favored the two-tissue compartment model (2TCM) in all ten regions of interest. Regional total distribution volume (V_T) values from each compartmental model and Logan analysis were generally well identified except for corpus callosum V_T using the 2TCM. Logan analysis was assessed as the choice model due to stability of regional V_T values from 90-min data and due to high correlation of Logan-derived regional V_T values with those from the 2TCM. [^{18}F]FNDP binding was higher in human cerebellar cortex and thalamus relative to supratentorial cortical regions, which aligns with reported expression patterns of the epoxide hydrolase 2 gene in human brain.

Conclusion

These data support further use of [^{18}F]FNDP PET to study sEH in human brain.

Introduction

Soluble epoxide hydrolase (sEH) is an enzyme expressed throughout the body, and plays a role in maintaining homeostasis of polyunsaturated fatty acids and their byproducts. That homeostasis may have an effect on immune signaling, as reviewed by Zarriello et al.[28] For example, polyunsaturated fatty acids can be metabolized to epoxy fatty acids (epoxyeicosatrienoic or epoxydocosapentaenoic acids) that promote vasodilatation and anti-inflammatory pathways, while the metabolism of polyunsaturated fatty acids through the cyclooxygenase pathway yields more inflammatory derivatives (prostaglandins). Since sEH is an enzyme that metabolizes anti-inflammatory epoxy fatty acids to the corresponding, relatively inert 1,2-diols, a high availability or activity of sEH may promote vasoconstriction and inflammation in local tissues[28,74]. That inflammatory microenvironment may foster and/or exacerbate pathologic changes in several clinical conditions[75,76], and therapies to block sEH activity are accordingly in various stages of development[28].

We developed *N*-(3,3-diphenylpropyl)-6-^{18}F-fluoronicotinamide ([^{18}F]FNDP) (Figure 3-1) for use with positron emission tomography (PET) to study the proposed link between high availability of sEH in the human brain and neurologic or psychiatric conditions[75,76]. [^{18}F]FNDP PET may also provide utility in assessing target engagement of drugs developed to block sEH activity in brain. [^{18}F]FNDP showed high binding specificity in CD-1 and sEH knockout mice[77]. In brains of *Papio anubis*, [^{18}F]FNDP demonstrated reversible radiotracer pharmacokinetics and [^{18}F]FNDP binding [total distribution volume (V_T)] was estimated well in 18 regions of interest (ROIs) using 90-min dynamic emission data with a radiometabolite-corrected arterial input function[77]. HPLC radiometabolite analyses in CD-1 mouse and baboon studies demonstrated evidence of two radiometabolites of [^{18}F]FNDP (parent [^{18}F]FNDP, retention time = 7.8 min; metabolite #1, retention time = 1–2 min; metabolite #2, retention time = 5.7 min). Sacrifice of the mice at 10 and 30 min post-injection (p.i.) of [^{18}F]FNDP revealed only a small (1.7%) presence of metabolite #1 in the brain at 30 min p.i., and no brain penetration of metabolite #2[78]. In baboon brains, [^{18}F]FNDP V_T was highest in insula, putamen, caudate, and amygdala, and intermediate in frontal and temporal cortices, as well as hippocampus[77,78]. Globus pallidus, white matter, hypothalamus, and thalamus had relatively lower [^{18}F]FNDP V_T estimates, and lowest [^{18}F]FNDP V_T occurred in cerebellum[77,78]. Pre-PET pharmacological treatment with a sEH inhibitor (nor-fluoro-FNDP) resulted in 95% blockade of the [^{18}F]FNDP binding in baboon brain[77]. Dose-dependent blockade in baboon brain was also found using AR-9281, a sEH inhibitor that is structurally dissimilar to FNDP[78]. Together, these blocking studies support high binding specificity of [^{18}F]FNDP.

Here, we report the first use of [^{18}F]FNDP PET in the healthy human brain. Since there are no known brain regions without sEH, quantitative binding was estimated using [^{18}F]FNDP imaging data with an arterial input function.

Materials and Methods

Human subject participation

This prospective study was approved by a Johns Hopkins Institutional Review Board. Healthy individuals between the ages of 35–55 years were recruited through local advertising and provided written, informed consent. Each subject completed a screening interview and blood work, electrocardiogram, and urine toxicology. Eligible participants were in stable health, with no clinical abnormality on the screening assessment or structural magnetic resonance imaging (MRI). Exclusion criteria included past neurological or psychiatric illness, history of substance abuse including marijuana (assessed by self-report and urine toxicology), recent infection, past head trauma with loss of consciousness, contraindication to MRI, or contraindication to PET with arterial line.

[^{18}F]FNDP PET in humans

Synthesis and injection of [^{18}F]FNDP

[^{18}F]FNDP was synthesized as previously described[79] and radiochemical purity was >95% at the end of each synthesis.

Brain PET image acquisition

PET data were acquired on a CPS/CTI High Resolution Research Tomograph (CPS Innovations, Inc., Knoxville, TN). Prior to scanning, a thermoplastic mask was molded to the participant's face for head fixation. A radial arterial catheter was placed for arterial blood sampling, and an intravenous catheter was inserted for radiotracer administration. A transmission scan was performed prior to the emission scan that began with bolus injection of [^{18}F]FNDP. Continuous emission data were collected for 180 min (N = 3) or 90 min (N = 4) p.i.

The PET data were binned into 30 frames (90-min scans, N = 4) or 48 frames (180-min scans, N = 3): 4 × 15 s, 4 × 30 s, 3 × 1 min, 2 × 2 min, 5 × 4 min, and 12 × or 30 × 5-min frames. Those data were reconstructed using the ordinary Poisson variant of the 3D ordered subsets expectation

maximization algorithm (with six iterations and 16 subsets)[80], without point spread function modeling, and with 2 mm Gaussian filtering. Each reconstructed image was 256 × 256 × 207 voxels, with voxel size: 1.22 × 1.22 × 1.22 mm^3.

Plasma analysis

Approximately 30–35 arterial blood samples (each 1 mL) were collected p.i. at the following time points: as fast as possible over 1.5 min; every 30 s between 1.5 and 3 min; every 2 min between 3 and 5 min; and every 5 min between 5 min to the end of the emission scan. Plasma was isolated by centrifugation at 4 °C (5 min at 2200 g) and radioactivity was counted using a 2480 WIZARD^2 gamma counter (PerkinElmer, Waltham, MA).

Larger (~4–6 mL) blood samples for analysis of parent [^{18}F]FNDP and its radiometabolites occurred at the following time points: before [^{18}F]FNDP injection for background measure, and p.i. at 5, 10, 20, 30, 45, 60, 75, and 90 min. Additional blood samples were obtained at 105, 120, 150, and 180 min p.i. for emission scans lasting 180 min, with ~100 mL total arterial blood volume obtained from participants who underwent 180-min scan duration. Parent [^{18}F]FNDP and its metabolites were analyzed using a reverse phase high-performance liquid chromatography (RP-HPLC) system composed of an Agilent Technologies (Santa Clara, CA) 1260 Infinity quaternary pump, a 1260 Infinity column compartment module, a 1260 Infinity UV detector, and Raytest GABI Star radiation detectors controlled by OpenLab CDS EZChrom (A.01.04) software. The RP-HPLC system was first standardized using [^{18}F]FNDP and a non-radioactive analog of the radiotracer prior to analysis. Plasma samples were loaded onto a 2-mL Rheodyne injector loop and directed to a capture column (packed with Phenomenex Strata-X 33-µm polymeric reverse phase sorbent) with 1% acetonitrile and 99% water mobile phase at 2 mL/min. The effluent from the capture column contained polar metabolites of [^{18}F]FNDP directed to detectors. After 2 min of elution, an analytical mobile phase (65% acetonitrile, 35% aqueous 0.06-M ammonium formate) was applied to elute the trapped non-polar metabolites and [^{18}F]FNDP to an analytical column (4.6 × 250 mm, XBridge Column, 5 µm) at 2 mL/min, which were then directed to detectors. RP-HPLC chromatograms were integrated to

provide percentage of parent [^{18}F]FNDP relative to detected radiometabolite peaks at each time point. Metabolite-corrected plasma time-activity curves (TACs) were derived by applying the percent parent [^{18}F]FNDP time-profiles from HPLC to the total plasma TACs after linear interpolation using PMOD (v3.7, PMOD Technologies Ltd., Zurich, Switzerland).

Plasma-free fraction (f_P) of [^{18}F]FNDP was assessed using plasma isolated from blood sampling prior to radiotracer injection. Plasma (1 mL) was incubated with 0.37 MBq of [^{18}F]FNDP for 5 min at room temperature. Then, three separate 150-µL aliquots of the mixture were applied to Centrifree membrane filters (Millipore, Burlington, MA) and centrifuged (20 min, 26,000g, 25 °C). To calculate f_P, 50-uL samples of elute and three 50-µL samples of plasma incubated with [^{18}F]FNDP were counted on an automated gamma counter (2480 WIZARD^2 gamma counter (PerkinElmer, Waltham, MA), with f_P = counts in ultrafiltrate relative to plasma.

Brain MRI acquisition and regional segmentation

Prior to PET, each participant completed a sagittal T1- weighted brain MRI sequence acquired using a 3 Tesla MAGNETOM Prisma scanner (Siemens, Malvern, PA, USA). Regions of interest (ROIs) were segmented from magnetization-prepared rapid gradient-echo data (spatial resolution 0.8 × 0.8 × 0.8 mm^3) using the FreeSurfer image analysis suite (http://surfer.nmr.mgh.harvard.edu/). The ten ROIs included a white matter region (corpus callosum), cortical regions (cerebellar, parietal, frontal, cingulate, occipital, and temporal cortices), and subcortical regions (thalamus, striatum, and hippocampus).

Kinetic analysis

PMOD was used for PET data processing and kinetic analyses, as well as pre-processing steps of motion correction and co-registration of PET and MRI data. Interframe motion correction was completed by rigid realignment of all frames of the reconstructed image to the 0–30-min mean PET image that was obtained by averaging frames 1 through 18. The 0–30-min mean image, and subsequently all motion-corrected PET frames, were co-registered to the individual's T1-weighted MRI using rigid transformations. Regional TACs were generated after applying the above ROIs to

the dynamic PET data that were transformed into MR space. Regional V_T[81] values were derived using the radiometabolite-corrected arterial input function with the one- or two-tissue compartment model (1TCM, 2TCM), or Logan graphical analysis[82]. Logan-derived V_T values were first evaluated using unfixed *t** and allowing a maximum error criterion of 10%, which guided the choice of fixed *t** =30 min (Supplemental Figure 3-1). For 1TCM and 2TCM, cerebral blood volume was set at 5% of brain volume when accounting for activity in the vasculature.

Model choice (1TCM v. 2TCM) was evaluated based on goodness of fit using the Akaike Information Criterion (AIC) and *F*-test[83,84]. The identifiability of V_T and other rate constants was assessed using the percent standard error from the theoretical parameter covariance matrix. Values assessed as identified "well" met criteria of % SE < 10%. For the three individuals with 180-min scans, regional V_T values were evaluated using varied, shortened scan durations down to 90-min data. In these analyses, V_T values derived from 180-min data were used as the standard for comparison. For each shortened scan duration (X), the relative bias values were expressed as $|V_{T\ X\ min} - V_{T\ 180\ min}|/V_{T\ 180\ min}$.

In order to visualize V_T of [^{18}F]FNDP across the healthy brain, a V_T parametric map was computed from the 90-min [^{18}F]FNDP dynamic PET data using Logan analysis (*t** = 30 min, *N* = 7) with the metabolite-corrected plasma input function. The V_T maps were then normalized using the PMOD's human brain normalization template derived from Statistical Parametric Mapping software (SPM8; Wellcome Centre for Human neuroimaging, UCL, London) and averaged to generate a mean V_T parametric map.

Statistical analysis

Microsoft Excel (Microsoft 365) was used for statistical analyses. Quantitative results are presented as mean ± standard deviation (SD) unless otherwise noted. The correlation between continuous V_T values derived from different approaches (1TCM, 2TCM, Logan graphical analysis) was evaluated using linear regression analysis.

Results

Radiotracer injection and plasma analysis

Seven participants (5 males, 2 females, ages 40–53 years, median 52 years) underwent [^{18}F]FNDP PET (Table 3-1). Molar radioactivity was 1592 ± 1289 GBq/μmol (range 466– 4025 GBq/μmol) at the time of injection. The mean administered mass and radioactivity of [^{18}F]FNDP were 0.13 ± 0.09 μg (range 0.03–0.26 μg) and 355.7 ± 25.6 MBq (range 309.0–378.1 MBq), respectively. Injection of [^{18}F]FNDP did not yield adverse effects and there were no clinical changes in pre- versus post-injection laboratory (blood, electrocardiogram) results.

Plasma activity peaked within 90 s p.i. and decreased to <5% of the peak by 5 min (Figure 3-2a for representative curve). The mean parent fraction at 180 min p.i. ($N = 3$) was 16.6 ± 6.5%, and at 90 min p.i. ($N = 7$, Figure 3-2b) was 27.2 ± 6.9%. f_P was 1.5 ± 0.2% ($N = 7$). Radio-RP-HPLC chromatograms recorded for the plasma collected at 180 min post-injection of [^{18}F]FNDP showed elution of (1) a polar radiometabolite species not retained on the capture column, (2) a radiometabolite that was retained on the capture column, and (3) parent [^{18}F]FNDP that is more lipophilic than species #2 as demonstrated by ~2 min longer retention time (Figure 3-2c).

Modeling results

[^{18}F]FNDP uptake across the brain ROIs is shown in Figure 3-3. TACs in corpus callosum peaked earlier (~2.5–3.5 min) compared to other regions that peaked ~7 min. Highest peak radioactivity concentration (standardized uptake value, SUV) occurred in cerebellar cortex, and the lowest SUV peak was observed in corpus callosum.

Visually, the 1TCM and 2TCM each fit the regional data well (Supplemental Figure 3-2). AIC favored the 2TCM in all ten ROIs ($P < 0.001$) (Supplemental Table 3-1). The *F*-test also confirmed that the 2TCM showed significantly better fit ($\alpha = 0.05$) compared to the 1TCM in 59 out of 70 TACs (84.3%). Overall, model selection criteria supported the 2TCM as preferred. Well-identified rate constants and

V_T values from each compartmental model and Logan analysis are summarized in Table 3-2. The 2TCM identified K_1 and V_T well for all ROIs except for V_T in corpus callosum that had poor identifiability in four of seven participants, as well as V_T in hippocampus and striatum in two separate individuals. Rate constants from the 2TCM other than K_1 were moderately or poorly identified (with larger % SE) across all ten ROIs. The 1TCM identified well K_1, k_2, and V_T for all ROIs. Using 90-min data (N = 7), V_T values derived from each model (1TCM, 2TCM) and Logan graphical analysis were highest in cerebellar cortex, thalamus, striatum, and hippocampus, with intermediate V_T values in other cortical ROIs, and lowest V_T in corpus callosum. This pattern of high cerebellar binding is generally consistent with the reported expression pattern of the EPHX2 transcript (encoded by the gene for sEH) that is higher in cerebellum relative to hippocampus, thalamus, and cortex in human brain [85] (Supplemental Table 3-2). After excluding data from corpus callosum due to the relative, poor identifiability of V_T, as well as the one case of poorly identified V_T in each of hippocampus and striatum (Table 3-2), regional V_T values were well correlated between each method: $V_{T\ 2TCM}$ = 1.07 $V_{T\ 1TCM}$ - 0.08, R^2 = 0.99; $V_{T\ Logan,\ t^*\ 30\ min}$ = 0.97 $V_{T\ 2TCM}$ + 0.02, R^2 = 0.99; $V_{T\ Logan,\ t^*\ 30\ min}$ = 1.03 $V_{T\ 1TCM}$ – 0.07, R^2 = 0.99 (Supplemental Figure 3-3). Parametric images of Logan-derived V_T from 90-min emission data are shown in Figure 3-4.

Time stability of V_T

Using data from the three healthy individuals with 180-min data, Logan-derived V_T values from data shortened to 90 min were within 4% of the V_T values obtained using the full 180-min data (Supplemental Figure 3-4). The minimum scan time needed to achieve stability in Logan-derived V_T value for each ROI is listed in Supplemental Table 3-3.

Discussion

We present first human neuroimaging data that support further use of [^{18}F]FNDP PET to estimate availability of sEH, which may be locally elevated in neuropsychiatric disorders including affective illness or schizophrenia[75]. [^{18}F]FNDP PET was without adverse effects, and peak brain radioactivity

concentrations (SUV) ranged from ~2.4–3.4 for all ROIs except corpus callosum, which had a lower peak value (SUV ~1.5).

Regional V_T values were identified well using each model except when using the 2TCM to estimate V_T in the corpus callosum. The 2TCM was favored over the 1TCM by AIC and the *F*-test. Using 1TCM or 2TCM, K_1 was identified well in all ROIs, and ranged between 0.14 and 0.19 mL cm^{-3} min^{-1} in all regions except corpus callosum that had lower K_1 (0.07 or 0.08 mL cm^{-3} min^{-1} using 1TCM or 2TCM, respectively). Logan graphical analysis produced regional V_Ts that agreed with those estimated from both the 2TCM and 1TCM, supporting its use in computing V_T in future [^{18}F]FNDP PET studies. Time stability analysis indicated that a 90-min scan time is adequate for Logan graphical analysis to produce accurate regional V_T values.

V_T values derived using each model were highest in cerebellar cortex, thalamus, and hippocampus (listed in sequentially decreasing order), across the ten ROIs that included five cortical brain regions. These human imaging data suggest a different pattern of sEH distribution in human brain compared to that of baboon, since we found evidence of relatively low sEH in baboon cerebellum using [^{18}F]FNDP PET[77,78]. We note that our human imaging results are generally consistent with reported, higher consensus normalized expression levels of the epoxide hydrolase 2 gene (*EPHX2*) in human cerebellum, thalamus, and hippocampal formation compared to cerebral cortex[85]. We acknowledge that the scope of this work did not include the identification of the chemical structures of radiometabolite species. However, the pattern of decline after the single peak in the human time-activity curves suggests an absence of brain-penetrant radiometabolites, and previous work using [^{18}F]FNDP in mice revealed only minute (<2%) presence of a radiometabolite in brain[78]. Since binding in corpus callosum was relatively low, investigation of the degree of displaceable binding in this region should be studied further. Future work is also needed to evaluate for possible effects of sex or age on [^{18}F]FNDP binding in human brain that could not be adequately tested in this small sample.

Conclusion

[^{18}F]FNDP PET is a promising technique for studying soluble epoxide hydrolase in human brain in vivo. These data support the use of Logan analysis to derive regional [^{18}F]FNDP V_T values using 90-min emission data in healthy human brain.

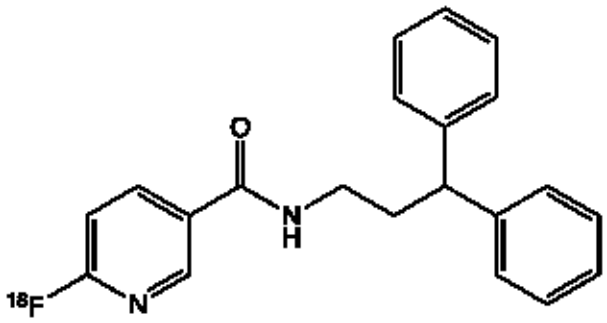

Figure 3-1. Chemical Structure of [^{18}F]FNDP

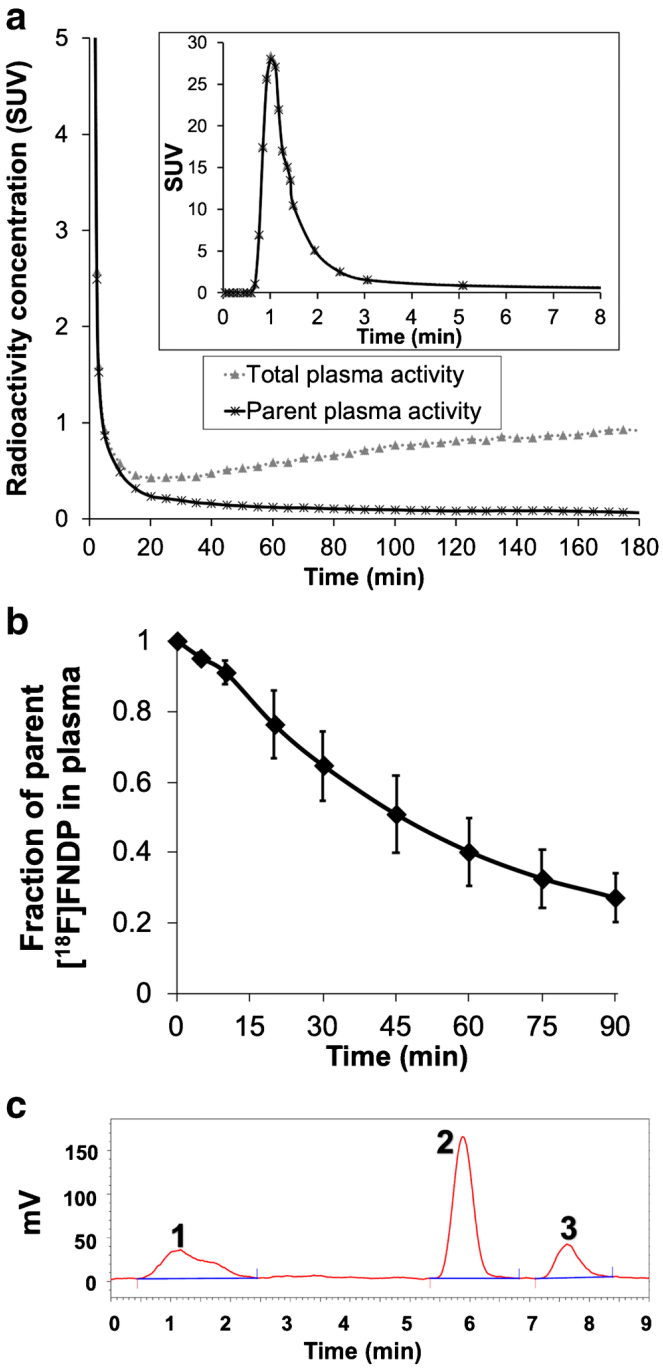

Figure 3-2. Plasma profile of parent [^{18}F]FNDP and its radiometabolites in healthy individuals.

a Total activity concentration (in SUV) in plasma and parent [^{18}F]FNDP activity in plasma in a subject who underwent a 180-min emission scan. **b** Fraction of parent [^{18}F]FNDP in plasma over a 90-min emission scan ($N = 7$), shown as mean ± standard deviation. **c** Radio-RP-HPLC chromatogram recorded for the plasma collected at 180 min post-injection of [^{18}F]FNDP, showing elution of (1) a polar radiometabolite species not retained on the capture column (26%); (2) a radiometabolite that was retained on the capture column (58%); and (3) parent [^{18}F]FNDP (16%) that is more lipophilic than species #2 as demonstrated by ~2 min longer retention time

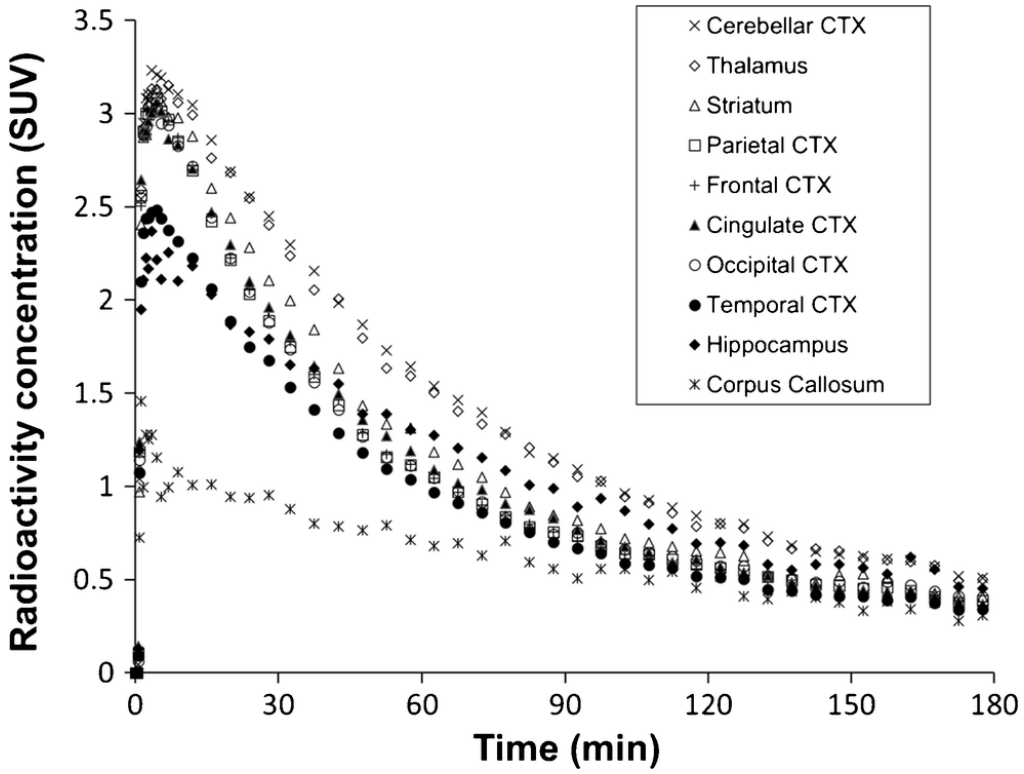

Figure 3-3. Regional radioactivity time-activity curves (TACs) in a representative healthy human participant. Activity concentrations are shown in SUV. Regions in the legend are listed from highest to lowest peak activity

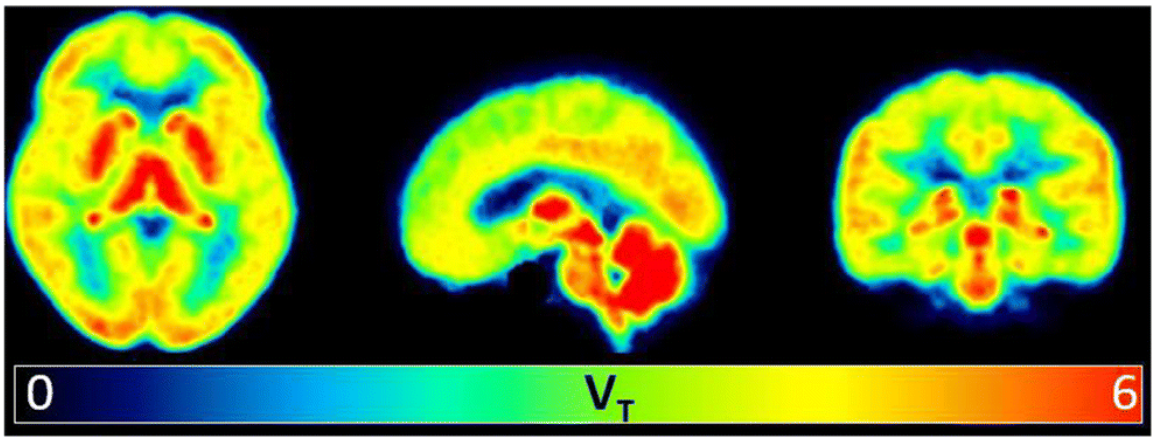

Figure 3-4. Mean parametric map of the total distribution volume (V_T) of [^{18}F]FNDP.

For each of the healthy participants ($N = 7$), a V_T parametric map was computed from the 90-min [^{18}F]FNDP dynamic PET data using Logan analysis ($t^* = 30$ min) with the metabolite-corrected plasma input function. The V_T maps were then normalized to a SPM8 brain template and averaged to generate a mean V_T parametric map. V_T is in units of mL cm^{-3}

Table 3-1. Clinical characteristics of 7 healthy human participants.

Age (years)	48.7 ± 4.9[a]
Sex (Male/Female)	5/2
Race (Caucasian/African American)	3/4
Body mass index	28.0 ± 3.2[a]

[a]Presented as mean ± standard deviation

Table 3-2. Modeling of [^{18}F]FNDP PET data from 90-min emission scans (N = 7) identified well the kinetic parameters and total distribution volume (V_T) values using the one-tissue compartment model (1TCM) in all regions.

K_1 and V_T values were well identified using a two-tissue compartment model (2TCM) in most regions, and V_T values using Logan analysis were well identified in all regions

	1TCM			2TCM					Logan
ROI	K_1 (mL cm^{-3} min^{-1})	k_2 (min^{-1})	V_T (mL cm^{-3})	K_1 (mL cm^{-3} min^{-1})	k_2 (min^{-1})	k_3 (min^{-1})	k_4 (min^{-1})	V_T (mL cm^{-3})	V_T (mL cm^{-3})
Thalamus	0.17 ± 0.02	0.03 ± 0.01	6.15 ± 0.83	0.19 ± 0.03	0.07 ± 0.03	0.10 ± 0.06	0.07 ± 0.02	6.48 ± 0.93	6.30 ± 0.91
Striatum	0.17 ± 0.02	0.03 ± 0.01	5.45 ± 0.68	0.18 ± 0.03	0.06 ± 0.03	0.06 ± 0.06	0.07 ± 0.04	5.72 ± 0.78[a]	5.49 ± 0.70
Hippocampus	0.13 ± 0.02	0.02 ± 0.00	5.57 ± 0.81	0.15 ± 0.03	0.06 ± 0.03	0.07 ± 0.04	0.06 ± 0.03	5.98 ± 0.99[a]	5.79 ± 0.87
Corpus Callosum	0.07 ± 0.01	0.02 ± 0.00	2.96 ± 0.47	0.08 ± 0.02	0.06 ± 0.02	0.05 ± 0.02	0.03 ± 0.01	3.24 ± 0.36[b]	3.34 ± 0.62
Cerebellar CTX	0.17 ± 0.02	0.03 ± 0.00	6.59 ± 0.87	0.20 ± 0.03	0.08 ± 0.05	0.14 ± 0.14	0.07 ± 0.02	6.91 ± 0.94	6.70 ± 0.92
Temporal CTX	0.14 ± 0.02	0.03 ± 0.01	4.32 ± 0.65	0.15 ± 0.03	0.07 ± 0.03	0.07 ± 0.08	0.06 ± 0.03	4.59 ± 0.73	4.41 ± 0.68
Occipital CTX	0.18 ± 0.02	0.04 ± 0.01	4.60 ± 0.67	0.19 ± 0.03	0.08 ± 0.03	0.07 ± 0.06	0.07 ± 0.02	4.84 ± 0.71	4.73 ± 0.70
Cingulate CTX	0.17 ± 0.02	0.04 ± 0.01	4.64 ± 0.66	0.18 ± 0.03	0.07 ± 0.04	0.07 ± 0.07	0.07 ± 0.03	4.88 ± 0.71	4.72 ± 0.72
Frontal CTX	0.16 ± 0.02	0.04 ± 0.01	4.37 ± 0.57	0.18 ± 0.03	0.08 ± 0.04	0.09 ± 0.09	0.09 ± 0.04	4.54 ± 0.60	4.43 ± 0.61
Parietal CTX	0.17 ± 0.02	0.04 ± 0.01	4.54 ± 0.62	0.18 ± 0.03	0.08 ± 0.04	0.08 ± 0.07	0.08 ± 0.03	4.74 ± 0.65	4.63 ± 0.63

Presented as mean ± standard deviation for each estimated parameter. Identifiability of each parameter was assessed as percentage standard error < 10% and when not met the value was excluded: [a]N = 6, [b]N = 2. Region of interest, ROI; cortex, CTX

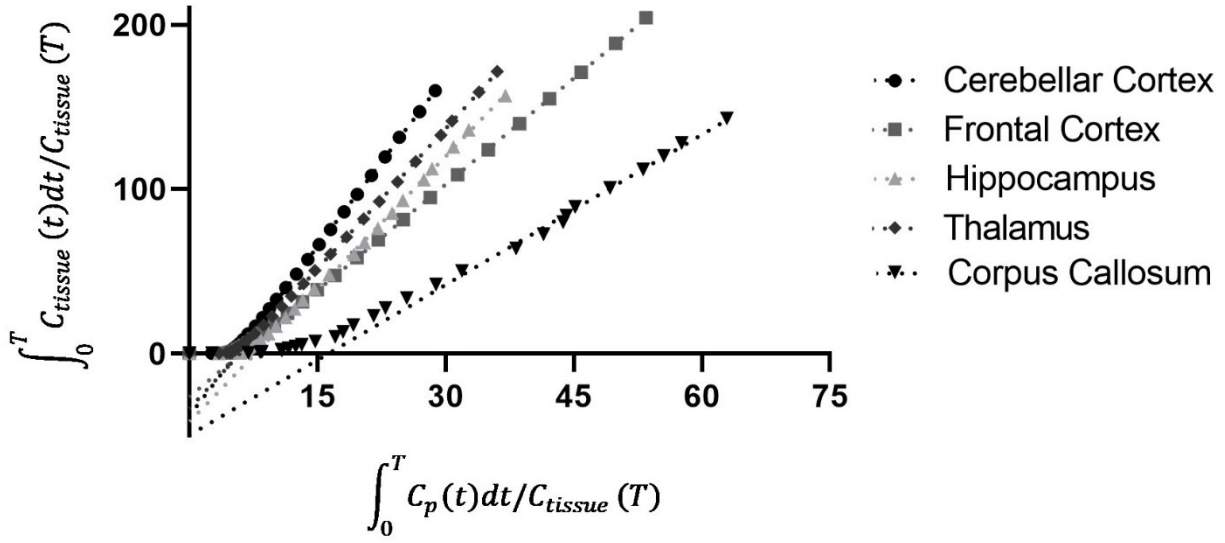

Supplemental Figure 3-1. Logan graphical analysis of healthy control data.

Logan graphical analysis with fixed t*=30 min demonstrates reasonable linearity as shown for representative regions from a healthy control.

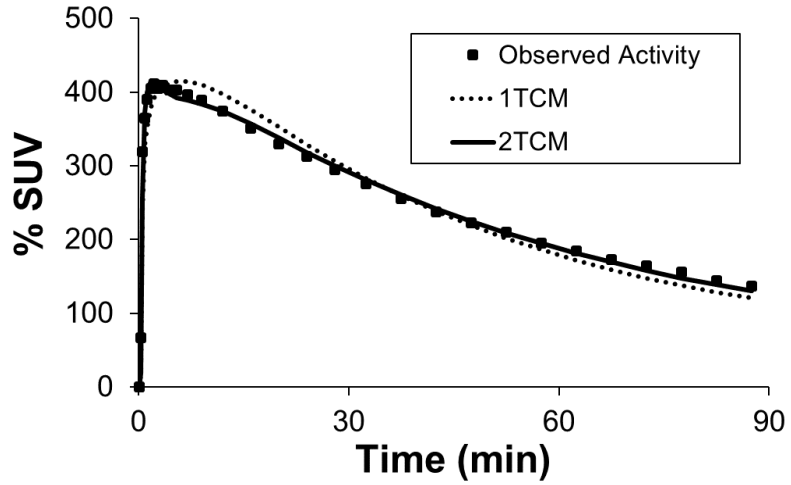

Supplemental Figure 3-2. Typical time activity curve and model fits (1TCM, 2TCM) in cerebellar cortex from a representative individual.

Observed activity (squares) and model curves (dotted curve, 1TCM; solid line curve, 2TCM) are shown.

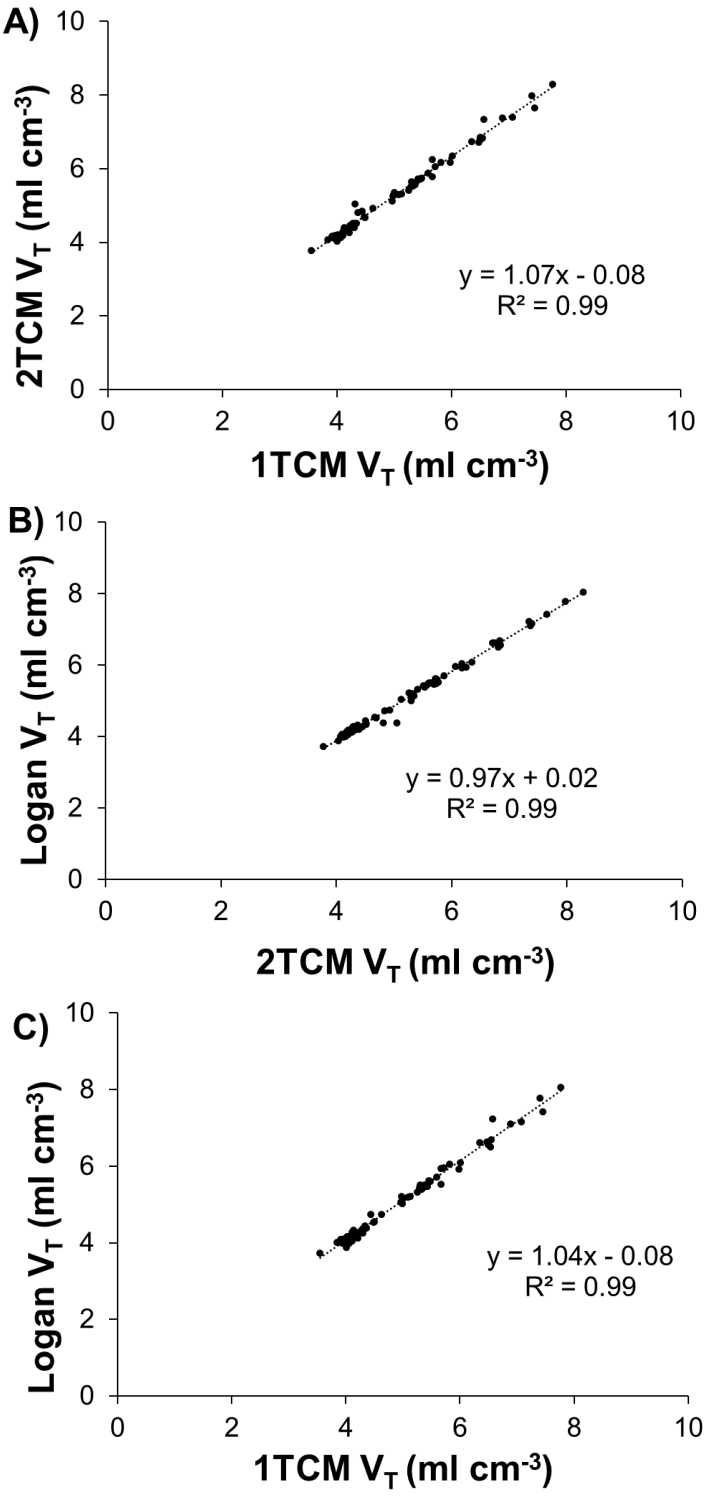

Supplemental Figure 3-3. Relationship between [^{18}F]FNDP binding outcomes including comparison of A) 1TCM V_T with 2TCM V_T; B) 2TCM V_T with Logan V_T; and C) 1TCM V_T with Logan V_T.

Corpus callosum V_T values and one case of V_T in each of hippocampus and striatum were excluded due to poor identifiability.

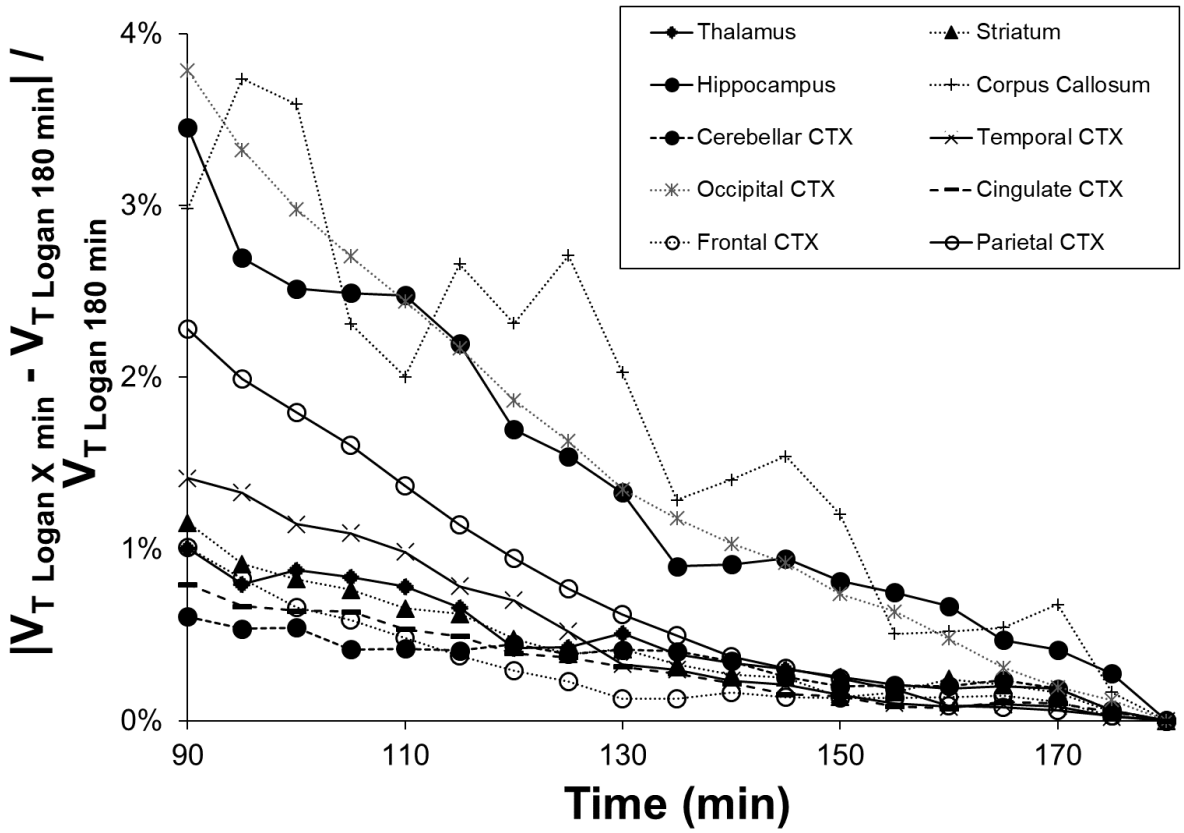

Supplemental Figure 3-4. Assessment of the relative stability in [^{18}F]FNDP regional Logan-derived total distribution volume (V_T) values from 180 min of data compared to values produced from truncated (by five min intervals down to 90 min) scan duration (*N*=3).

V_T estimates are in units of mL cm^{-3}. The percent of the absolute difference between the V_T values from 180 minutes of data and V_T values from shortened scan duration are plotted for each of the ten regions of interest. Cortex, CTX.

Supplemental Table 3-1. Comparison of the goodness of fit assessed by Akaike information criterion (AIC) values from each compartmental model applied to 90 min dynamic [^{18}F]FNDP PET data from seven healthy human participants.

ROI	1TCM*	2TCM*
Thalamus	29.00 ± 15.21	10.00 ± 24.15
Striatum	28.13 ± 11.81	21.07 ± 15.72
Hippocampus	36.75 ± 14.19	23.88 ± 18.06
Corpus Callosum	72.55 ± 7.67	67.00 ± 12.41
Cerebellar CTX	26.00 ± 12.46	4.17 ± 25.03
Temporal CTX	35.62 ± 13.82	23.66 ± 23.48
Occipital CTX	33.12 ± 17.30	12.70 ± 27.43
Cingulate CTX	38.24 ± 14.51	23.10 ± 27.24
Frontal CTX	35.55 ± 16.64	20.68 ± 29.50
Parietal CTX	34.56 ± 15.66	16.06 ± 29.25

*AIC values are presented as mean ± standard deviation. Region of Interest, ROI; One-tissue compartment model, 1TCM; Two-tissue compartment model, 2TCM; Cortex, CTX. Paired t-test $P < 0.001$.

Supplemental Table 3-2. Among the regions of interest (ROIs) in this study, highest [^{18}F]FNDP binding (V_T) was found in cerebellar cortex, consistent with reported higher expression levels of EPHX2 in cerebellum relative to other ROIs evaluated.

ROI	Logan V_T	Regional consensus normalized expression level of EPHX2[a]
Cerebellar CTX	6.7 ± 0.9	5.6[b]
Hippocampus	5.8 ± 0.9	4.1
Thalamus	6.3 ± 0.9	3.9
Cerebral CTX	4.6 ± 0.2[c]	3.3

Logan graphical analysis used t^* = 30 min. [a]Using the online Human protein atlas [85], consensus normalized expression levels of the EPHX2 RNA transcript in brain are presented and were derived by combining data from two transcriptomics datasets. Of the 10 brain regions with consensus normalized expression levels, [^{18}F]FNDP binding was assessed in four similar ROIs (listed). [b]The human protein atlas reports data from total cerebellum, whereas the imaging study used cerebellar cortex. [c][^{18}F]FNDP binding across cerebral cortex binding was derived by calculating the average of [^{18}F]FNDP V_T values from temporal, occipital, cingulate, frontal, and parietal cortices. V_T is in mL cm^{-3}.

Supplemental Table 3-3. The minimum scan duration needed to achieve stable [^{18}F]FNDP total distribution volume (V_T) values using 180 min "gold-standard" duration (N = 3).

Region of Interest	Minimum Scan Duration (min)
Thalamus	60
Striatum	60
Hippocampus	60
Corpus Callosum	85
Cerebellar Cortex	60
Temporal Cortex	60
Occipital Cortex	70
Cingulate Cortex	60
Frontal Cortex	60
Parietal Cortex	60

Stability of V_T was assessed as < 5% absolute percent difference between [^{18}F]FNDP V_T derived from 180 min data and V_T from shortened data (down to 60 min). Logan graphical analysis (t^* = 30 min) was used to estimate regional V_T.

Chapter 4: Examining brain inflammatory processes through kinetic modeling of radiotracers in human clinical studies: A study of [^{18}F]XTRA in extrathalamic regions

Summary:

The focus of this chapter is on the first in man study of [^{18}F]XTRA to study the distribution of the α4β2 nicotinic acetylcholine receptor (α4β2-nAChR) in the human brain. In this study, we utilized positron emission tomography to study the distribution of [^{18}F]XTRA in 17 healthy, non-smoking adults. Using PMOD, we were able to use the time activity curves generated for the 10 regions of interest (ROIs) to characterize the binding of [^{18}F]XTRA to α4β2-nAChR using a two-tissue compartment model and Logan graphical analysis. Additionally, we used total distribution volumes (V_T) generated from Logan graphical analysis to test the relationship between age and binding in the hippocampus.

^{18}F-XTRA PET for enhanced imaging of the extrathalamic α4β2 nicotinic acetylcholine receptor

This work has been published and is reprinted here with permission from *The Journal of Nuclear Medicine.*

Coughlin JM, Slania S, Du Y, Rosenthal HB, Lesniak WG, Minn I, Smith GS, Dannals RF, Kuwabara H, Wong DF, Wang Y, Horti AG, Pomper MG. ^{18}F-XTRA PET for Enhanced Imaging of the Extrathalamic α4β2 Nicotinic Acetylcholine Receptor. J Nucl Med. 2018 Oct;59(10):1603-1608.

Abstract

Reduced density of the α4β2 nicotinic acetylcholine receptor (α4β2-nAChR) in the cortex and hippocampus of the human brain has been reported in aging and patients with neurodegenerative disease. This study assessed the pharmacokinetic behavior of ^{18}F-(−)-JHU86428 (^{18}F-XTRA), a new radiotracer for in vivo PET imaging of the α4β2-nAChR, particularly in extrathalamic regions of interest in which the α4β2-nAChR is less densely expressed than in thalamus. ^{18}F-XTRA was also used to evaluate the α4β2-nAChR in the hippocampus in human aging.

Methods:

Seventeen healthy nonsmoker adults (11 men, 6 women; age, 30–82 y) underwent PET neuroimaging over 90 or 180 min in a high-resolution research tomograph after bolus injection of ^{18}F-XTRA. Methods to quantify binding of ^{18}F-XTRA to the α4β2-nAChR in the human brain were compared, and the relationship between age and binding in the hippocampus was tested.

Results:

^{18}F-XTRA rapidly entered the brain, and time–activity curves peaked within 10 min after injection for extrathalamic regions and at approximately 70 min in the thalamus. The 2-tissue-compartment model (2TCM) predicted the regional time–activity curves better than the 1-tissue-compartment model, and total distribution volume (V_T) was well identified by the 2TCM in all ROIs. V_T values estimated using Logan analysis with metabolite-corrected arterial input were highly correlated with those from the 2TCM in all regions, and values from 90-min scan duration were on average within 5% of those values from 180 min of data. Parametric images of V_T were consistent with the known distribution of the α4β2-nAChR across the brain. Finally, an inverse correlation between V_T in the hippocampus and age was observed.

Conclusion:

Our results extend support for use of ^{18}F-XTRA with 90 min of emission scanning in quantitative human neuroimaging of the extrathalamic α4β2-nAChR, including in studies of aging.

Introduction

Nicotinic acetylcholine receptors (nAChRs) are pentameric ligand–gated ion channels, of which the α4β2 and α7 are the most abundant subtypes in the human brain. The loss of activity of even a small quantity of neuronal nAChRs can have wide-ranging effects on neurotransmission across neural circuits[86]. Altered density of the α4β2-nAChR is linked to several neurodegenerative disorders[26,87–89]. Additionally, postmortem work using ^{3}H-epibatidine[90] and some in vivo human imaging, including that using 2-^{18}F-fluoro-A-85380 (2-^{18}F-FA) with PET[89,91], suggest diminished availability of the α4β2-nAChR in human aging. The binding of 2-^{18}F-FA in the hippocampus and thalamus inversely correlated with performance on a cognitive task of processing speed in a cohort of elderly healthy participants[92].

There is need for α4β2-nAChR–targeting radiotracers with faster pharmacokinetics and high specific uptake in brain tissue outside the thalamus (extrathalamic regions such as the cortex and striatum)[93,94], in which the α4β2-nAChR is less densely expressed[95]. ^{18}F-(−)-JHU86428 (^{18}F-XTRA)[96,97] is among such recently developed radioligands[97–99] and has promising in vitro binding characteristics, including subnanomolar binding affinity (K_i = 0.06 nM) and improved lipophilicity (Log$D_{7.4}$ = 0.67) over that of 2-^{18}F-FA[97]. ^{18}F-XTRA also showed stable, high binding estimates in extrathalamic regions of the baboon brain in vivo[96].

This study assessed use of ^{18}F-XTRA with PET imaging in the human brain, particularly in extrathalamic regions of interest (ROIs). Estimates of total distribution volume (V_T) generated using kinetic modeling methods with arterial input function and using alternative scan durations were compared. Finally, we investigated the correlation between age and V_T in the hippocampus, a region in which low availability of the α4β2-nAChR may be linked to subtle deficits in cognition even in otherwise healthy older individuals[92].

Materials and Methods

Human Subjects

This prospective study was approved by a Johns Hopkins Institutional Review Board, and all subjects provided written informed consent. Seventeen healthy adult (≥18 y) participants were recruited through local advertising. Each subject completed a screening interview and laboratory testing (blood counts, metabolic panel, coagulation studies), electrocardiogram, and urine toxicology. Eligible participants had stable health with no clinical abnormality on the screening assessment and structural MRI. Exclusion criteria included nicotine use in the past year, past psychiatric or neurologic illness, history of substance abuse including marijuana (assessed by self-report and urine toxicology), medication known to affect acetylcholine signaling, current psychotropic medication use, contraindication to MRI, or contraindication to PET imaging with arterial line.

All older (≥50 y) participants were also assessed with neuropsychologic testing that included the Clinical Dementia Rating scale[100] to ensure a global Clinical Dementia Rating of 0, consistent with normal cognition. Since the apolipoprotein ε4 (APOE ε4) allele may play a role in aberrant cholinergic signaling[101] that may be linked to altered α4β2-nAChR availability[102], older participants were assessed for APOE ε4 carrier status using methods described previously[103].

Human Brain Imaging

Synthesis of 18F-XTRA.

^{18}F-XTRA was synthesized as previously described[96]. Radiochemical purity was greater than 99%, with high specific radioactivity (1,586 ± 937 GBq/μmol) at the time of injection. The mean administered mass and radioactivity of ^{18}F-XTRA were 0.08 ± 0.04 μg (range, 0.03–0.17 μg) and 335 ± 38.3 MBq (range, 235–387 MBq), respectively. There were no adverse or clinically detectable pharmacologic effects, and no significant changes in vital signs, laboratory results, or electrocardiograms were observed.

Brain PET Image Acquisition.

All participants wore a thermoplastic facemask to minimize head movement and underwent both radial arterial line and antecubital venous catheter insertion. PET scans were acquired using a High-Resolution Research Tomograph (Siemens Healthcare) with 2.5-mm reconstructed image resolution[104]. Each emission scan started at the time of bolus intravenous injection of ^{18}F-XTRA, with continuous list-mode data collection for 90 (*n* = 10) or 180 (*n* = 7) min. Imaging data were reconstructed using methods described in the supplemental materials (available at http://jnm.snmjournals.org).

Plasma Sampling.

Measurement of the arterial plasma input function was conducted through collection of 35–50 blood samples (1 mL), obtained after injection using the previously published protocol[103]. Samples from 120 to 180 min after injection were collected every 10 min. Plasma was immediately isolated from whole blood using centrifugation. Radioactivity was counted in a cross-calibrated γ-well-counter. The

fraction of parent radioligand in plasma was determined by high-performance liquid chromatography (HPLC) with blood sampling as previously described[103], with additional blood sampling at 105, 120, 150, and 180 min after injection for 180-min scans.

The modified column-switching HPLC method[105] used a Waters reverse phase XBridge BEH C18 5 μM 4.6 × 150 mm analytic column, with an analytic mobile phase (45% acetonitrile and 55% aqueous solution of 0.1% ammonium hydroxide) at 2 mL/min. The HPLC system was standardized using nonradioactive XTRA and ^{18}F-XTRA before analysis of plasma samples, which were spiked with 10 μL of XTRA (1 mg/mL) for each run. Metabolite-corrected plasma time–activity curves were obtained by applying percentage parent ligand time profiles, generated by HPLC analysis, to the total plasma time–activity curves after linear interpolation in PMOD (version 3.7; PMOD Technologies Ltd.).

MRI Acquisition.

T1-weighted brain MRI at 3 T was acquired for each participant using methods identical to those as previously described[103], to obtain a 0.8 × 0.8 × 0.8 mm 3-dimensional image with a magnetization-prepared rapid gradient-echo sequence.

PET Image Analysis and Volumes of Interest.

PET image processing, including motion correction and kinetic analysis, was conducted using PMOD as previously described[103]. PET time–activity curves were generated for 10 ROIs that were segmented from each MR image using the FreeSurfer image analysis suite (http://surfer.nmr.mgh.harvard.edu/). ROIs included the thalamus, striatum, hippocampus, corpus callosum, as well as cerebellar, temporal, occipital, cingulate, frontal, and parietal cortices. Total intracranial volume was also defined using FreeSurfer for generating regional volume ratio values (ROI volume normalized to total intracranial volume).

Derivation of Rate Constants and V_Ts.

V_T[81] for each ROI was derived using the metabolite-corrected arterial input function and compartmental modeling (1-tissue-compartment model with 3 parameters [1TCM]; 2-tissue-compartment model with 5 parameters [2TCM]) or Logan graphical analysis[82]. In compartmental modeling, nonlinear least-squares analysis was performed, with the Marquardt algorithm for parameter estimation[106]. Logan-derived V_T values were determined using ordinary least squares after transformation of the PET data with t* = 45 min. The contribution of cerebral blood volume was set at 5% of brain volume. As in other recent PET imaging of this target[96,107], reference-tissue models were not applied because there is no clearly identified human brain region devoid of the α4β2-nAChR.

Statistics

Compartmental model fitting was assessed by visual inspection of the model fit to the time–activity curves and by relative goodness of fit using the Akaike information criterion[108]. The standard errors of nonlinear least-square estimates of rate constants and V_T from modeling were computed from the covariance matrix in PMOD and expressed as the coefficient of variation (% COV)[109]. Regional V_T estimates from variable scan durations were evaluated using the 180-min acquisition as the reference for comparison of V_T values from data shortening (shortened to 90 min). For each duration, denoted X, relative bias values were expressed as $|V_{TX} – V_{T\ 180\ min}|/V_{T\ 180\ min}$.

The relationship between V_T in the hippocampus and age was tested using Spearman rank-order correlation analysis because age was not normally distributed across the study population. Secondary analyses testing the relationship between age and V_T in the other 9 ROIs were also explored.

Statistical analyses were performed using SPSS Statistics (version 23.0; IBM Corp.). Data were checked for outliers[110], and descriptive statistics were obtained. Normality of the data was assessed

using the Shapiro–Wilk test. Data are presented as mean ± SD, and significance was set to a *P* value less than 0.05 unless otherwise noted.

Results

Human Subjects

Seventeen healthy nonsmokers (11 men, 6 women; age, 30–82 y; median age, 60 y; interquartile range, 37 y) underwent PET neuroimaging with ^{18}F-XTRA (Table 4-1). All older participants (*n* = 10) had a global Clinical Dementia Rating of 0, and none of the participants was an APOE ε4 carrier. ROI volumes and volume ratios from the study population are presented in Supplemental Table 4-1.

Plasma Analysis

Plasma activity peaked within 90 s after injection and decreased to less than 5% of the peak by 20 min (Figure 4-1A). HPLC easily isolated ^{18}F-XTRA (retention time, 7.5 min) from its radiolabeled metabolites, which were more polar and well resolved from the parent compound. ^{18}F-XTRA represented 21.8% ± 10.7% of total plasma activity by 90 min (Supplemental Figure 4-1) and 15.2% ± 10.5% by 180 min.

Determination of V_T

^{18}F-XTRA readily entered the brain and, for extrathalamic ROIs, activity peaked within 10 min after injection and then declined over the remaining 90- or 180-min scan duration (Figure 4-1B). Highest peak uptake occurred in the thalamus at approximately 70 min after injection except in 1 individual (a 76-y-old Caucasian man) whose thalamic activity peaked just before the end of the 90-min emission scan. Activity in the thalamus washed out gradually after the peak. The lowest uptake was observed in the corpus callosum.

Across the entire population, the kinetic behavior of ^{18}F-XTRA over the 90-min scan in each ROI yielded a visually better fit using the 2TCM compared with the 1TCM (Figure 4-1C for representative data) except for within the thalamus of the aforementioned individual who had unusually late, 90-min peak thalamic activity that did not converge for either compartmental model. Those outlier data were

excluded from further analyses, and when all other 90 min of continuous data were used, the Akaike information criterion favored the 2TCM in all 10 ROIs (Supplemental Table 4-2). The 2TCM identified V_T well (COV < 5%) for all ROIs except for the thalamus, which had a COV of 5.4% (Table 4-2). K_1 was also identified well (COV < 5%) using the 2TCM. The other rate constants from the 2TCM were identified with COV values of approximately 8%–22% for k_2 and 9%–24% for k_3/k_4 across all 10 ROIs. All V_T estimates (compartmental modeling, Logan) using 90-min emission data were highest in the thalamus and were more homogeneous across regions of the striatum, hippocampus, and cortical ROIs. V_T was lowest in the corpus callosum.

When 90-min data were used, values of regional V_T from Logan analysis correlated well with those of the 2TCM (Figure 4-2). Regional V_T values generated using Logan analysis from the 90-min continuous scans were also within 5% of the V_T values obtained using 180 min of continuous data from the same 7 individuals (Figure 4-3; Supplemental Table 4-3). Parametric images of V_T derived using Logan analysis from 90-min emission scans demonstrated binding of ^{18}F-XTRA throughout the brain (Figure 4-4).

Correlation Between Age and VT in Hippocampus

An inverse correlation between age and ^{18}F-XTRA V_T in hippocampus (*rho* = −0.589, $P = 0.014$) was found (Supplemental Figure 4-2). Secondary analyses revealed no significant correlation between age and V_T in other ROIs after applying correction for multiple comparisons ($P < 0.005$ after Bonferroni adjustment for all 10 ROIs). There was also no correlation between body mass index and V_T in any of the ROIs. One-way ANOVA analysis revealed no effect of sex or race on V_T. There was no correlation between age and volume or volume ratio for any of the 10 ROIs.

Discussion

PET imaging using newly developed radiotracers that have superior specificity for the α4β2-nAChR and faster brain kinetics over previously used radioligands[111] may further our understanding of changes in cholinergic activity over the course of cognitive decline[112]. Here we present the first

human neuroimaging data using PET and ^{18}F-XTRA, a radiotracer with promising physical[97] and in vivo[96] characteristics.

^{18}F-XTRA readily accessed the brain in 17 healthy participants, all of whom underwent PET for 90 or 180 min. The highest uptake was in the thalamus, with relatively lower uptake in the striatum, hippocampus, and cortex and lowest uptake in the corpus callosum, consistent with direct assessment in postmortem tissue[87]. After exclusion of thalamic data from 1 individual in whom thalamic activity peaked toward the end of the 90-min scan, V_T values were well estimated using the 2TCM and 90-min acquisition, especially in extrathalamic regions. The 2TCM was favored over the 1TCM by goodness of fit and Akaike information criterion. The 2TCM V_T and K_1 values were well identified (COV < 5%) in all extrathalamic regions and reasonably identified (COV = 5.4%) in the thalamus. K_1 was also high (K_1 > 0.48 mL cm^{-3} min^{-1} in all cortical and subcortical ROIs; K_1 = 0.30 mL cm^{-3} min^{-1} in corpus callosum), consistent with high radiotracer delivery. Overall, the observed high uptake into the brain, fast pharmacokinetics, and ability to estimate V_T in extrathalamic regions with a 90-min scan supports further use of ^{18}F-XTRA in clinical research.

This initial evaluation of ^{18}F-XTRA in healthy humans revealed a negative correlation between age and V_T in the hippocampus. Since amyloid plaque may negatively influence expression of this receptor[102], all elderly (≥50-y-old) participants were evaluated for APOE ε4 carrier status. Those older individuals lacked even 1 APOE ε4 allele and were therefore at relatively low risk for having high amyloid burden. There was also no correlation between age and hippocampal volume or volume ratio among these participants. Together, our results suggest that ^{18}F-XTRA PET may be sufficiently sensitive to measure the hypothesized loss of α4β2-nAChR availability over aging in extrathalamic regions[89–91], particularly the hippocampus, in which reduced expression of the β2 subunit may account for the lower α4β2-nAChR binding in the elderly[113]. This aging effect was not found using ^{18}F-nifene with PET, but this study population consisted of only 8 subjects (age, 21–69 y)[114].

^{18}F-XTRA V_T estimates were higher in most human extrathalamic brain regions than V_T values from bolus injection of other recently developed radiotracers with fast pharmacokinetics, such as (−)-^{18}F-flubatine[107,115] and ^{18}F-AZAN[116]. Since V_T represents the sum of both specific binding and nondisplaceable uptake[81], we note the limitation that a displacement study, such as using nicotine, is needed to compare specific binding patterns between recently developed radiotracers. Limited blocking studies in baboons using ^{18}F-XTRA PET after subcutaneous administration of cytisine, a selective partial agonist at the α4β2-nAChR, support the specificity of this radiotracer for its target[96]. Although ^{18}F-XTRA also has high affinity for the α6 nicotinic receptor subunit[97], central receptors containing the α6 subunit are relatively limited in distribution (retina, catecholaminergic nuclei) compared with the widespread, higher density of the α4β2-nAChR[117]. We also note that thalamic data from 1 individual among the 17 participants did not peak until close to the end of the 90-min scan, rather than peaking at approximately 70 min. Since we saw a similar, late peak in thalamic data in 1 of 5 baboons[96], a conservative approach for studying the α4β2-nAChR in the human thalamus may use longer ^{18}F-XTRA scan duration (180 min) or use an alternative radiotracer that has not shown outlier thalamic pharmacokinetics, such as ^{18}F-AZAN[116].

Conclusion

^{18}F-XTRA is a promising new radiotracer for measuring the human cerebral α4β2-nAChR in vivo. Analysis by the 2TCM using ^{18}F-XTRA data from 90-min scan duration is sufficient to estimate V_T in extrathalamic ROIs, such as the cerebral cortex, hippocampus, and striatum. ^{18}F-XTRA PET is also a promising tool for further study of the effect of aging on the availability of the α4β2-nAChR, particularly in the hippocampus of the human brain in vivo.

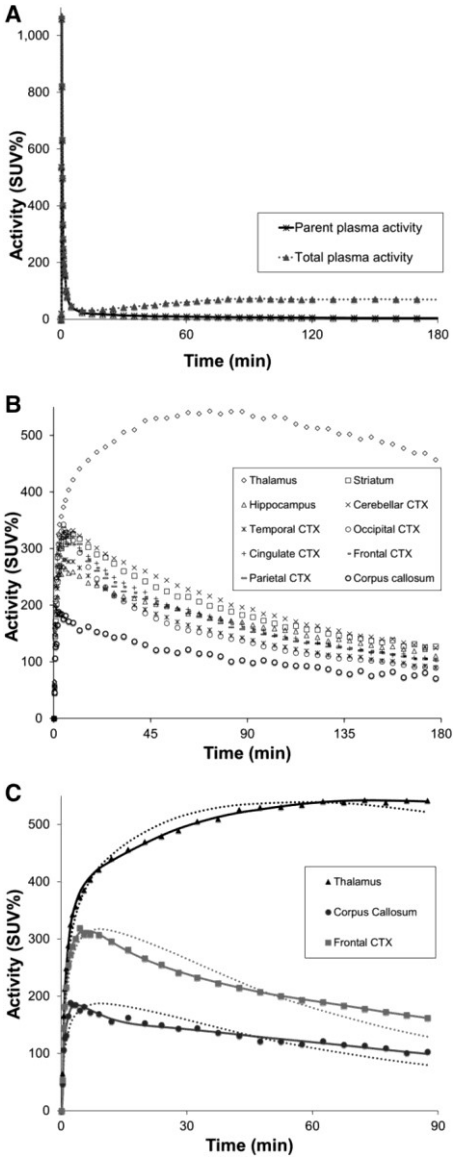

Figure 4-1. Time–activity curves from ^{18}F-XTRA imaging in a representative subject who underwent 180 min of continuous emission imaging.

(A) Radioactivity curves in total plasma and in the portion of unmetabolized ^{18}F-XTRA parent are shown with activity shown as percentages of injected dose per mL plasma normalized to body weight in grams (SUV%). (B) Radioactivity curves spanning 180 min in 10 ROIs are shown. Time–activity curves are shown as percentages of injected dose per cm^3 tissue normalized to body weight in grams (SUV%). (C) The 2TCM showed better fit to observed tissue time–activity curves than the 1TCM in all ROIs. Observed activity (data in shapes) and model curves (solid curve, 2TCM; dotted curve, 1TCM) over 90 min from thalamus, frontal cortex, and corpus callosum are shown. CTX = cortex.

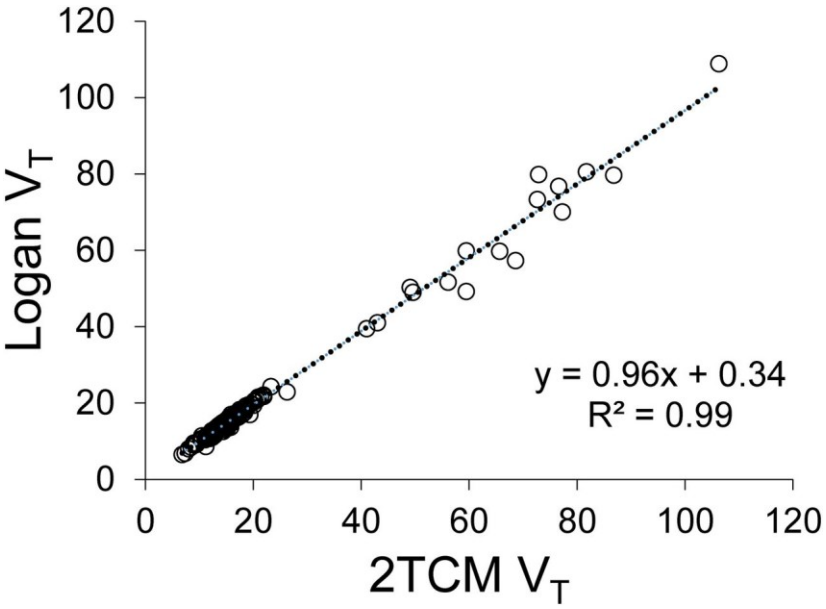

Figure 4-2. Comparison between ^{18}F-XTRA regional V_T values using 2TCM and Logan graphical analysis using 90-min data from 17 healthy individuals.

After exclusion of outlier thalamic data from 1 individual, regional V_T values from 2TCM were highly correlated with those from the Logan method (Spearman *rho* = 0.986, *P* = 0.000). Results from secondary regression analysis are also shown. V_T is in units of mL cm^{-3}.

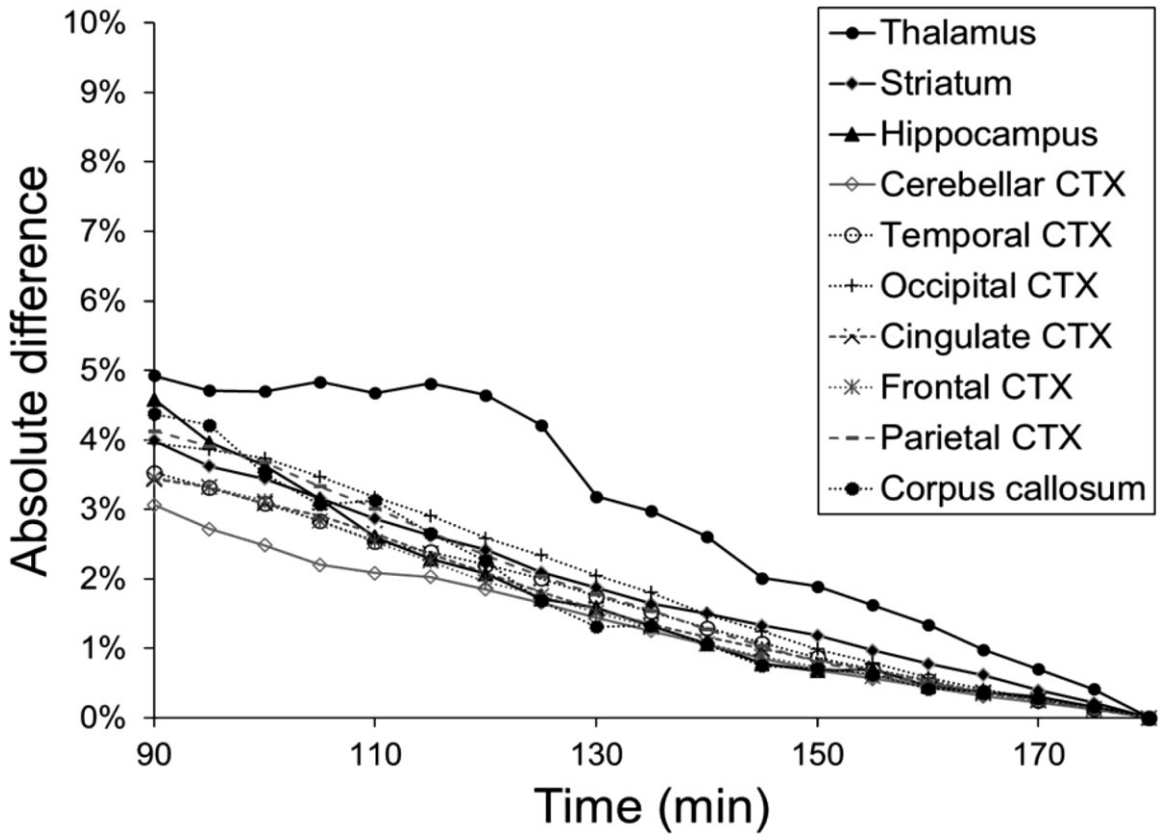

Figure 4-3. Assessment of relative stability in ^{18}F-XTRA regional V_T values from 180 min of data compared with values produced from truncated (by 5-min intervals down to 90 min) scan duration.

Data from 7 healthy individuals who underwent 180-min emission scans were included. V_T estimates are in units of mL cm^{-3}. Percentage of absolute difference between V_T values from 180 min of data and V_T values from shortened scan duration are plotted for each of the 10 ROIs. CTX = cortex.

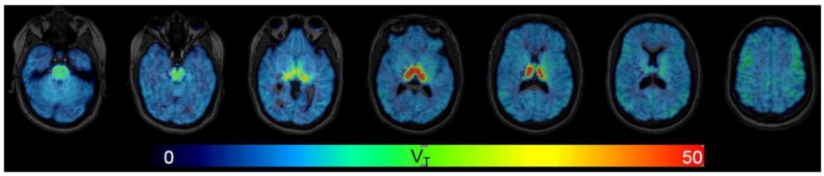

Figure 4-4. Parametric images of V_T of ^{18}F-XTRA, estimated using Logan graphical analysis with metabolite-corrected arterial input function and 90-min data from 1 representative healthy participant.

Transaxial views of PET/MR images demonstrate high V_T values in thalamus and lower V_T values in other cortical and subcortical regions. There is no apparent region without binding of ^{18}F-XTRA.

Table 4-1. Clinical and Demographic Characteristics of 17 Healthy Human Participants

Characteristic	Mean or number
Mean age ± SD (y)	56.7 ± 19.6
Sex (male/female)	11/6
Race (Caucasian/African American/Asian)	9/7/1
Mean body mass index ± SD	26.3 ± 3.2

Table 4-2. Kinetic Parameters and Total Distribution Volume (V_T) Values Estimated with 2TCM, Along with V_T Values Estimated Using 1TCM and Logan Analysis for ^{18}F-XTRA PET Imaging in Humans (n = 17)

	2TCM					
ROI	**K_1 (mL cm^{-3} min^{-1})**	**k_2 (min^{-1})**	**k_3/k_4 (unitless)**	**V_T (mL cm^{-3})**	**1TCM, V_T (mL cm^{-3})**	**Logan, V_T (mL cm^{-3})**
Thalamus*	0.61 ± 0.10 (2.9 ± 1.6)	0.15 ± 0.11 (22.2 ± 12.0)	13.0 ± 8.1 (21.8 ± 11.2)	66.6 ± 17.4 (5.4 ± 9.7)	57.7 ± 13.4 (3.5 ± 1.1)	64.1 ± 18.4 (2.6 ± 1.0)
Striatum	0.52 ± 0.09 (1.8 ± 1.0)	0.07 ± 0.02 (9.6 ± 5.9)	1.29 ± 0.50 (13.6 ± 7.9)	17.3 ± 3.4 (4.6 ± 4.0)	14.5 ± 1.9 (2.6 ± 0.5)	16.7 ± 2.9 (1.1 ± 0.6)
Hippocampus	0.48 ± 0.07 (2.5 ± 1.3)	0.12 ± 0.05 (11.8 ± 5.9)	2.92 ± 1.22 (12.1 ± 5.9)	15.6 ± 1.9 (3.6 ± 2.6)	12.9 ± 1.5 (3.8 ± 0.6)	15.6 ± 2.0 (1.8 ± 0.5)
Cerebellar cortex	0.52 ± 0.07 (1.6 ± 0.9)	0.08 ± 0.03 (10.4 ± 5.2)	1.80 ± 0.53 (13.3 ± 6.5)	17.6 ± 3.0 (2.3 ± 2.9)	15.8 ± 2.3 (2.4 ± 0.5)	17.7 ± 3.1 (0.6 ± 0.3)
Temporal cortex	0.49 ± 0.08 (1.8 ± 1.3)	0.10 ± 0.05 (10.1 ± 7.6)	1.66 ± 1.01 (12.6 ± 8.1)	13.7 ± 2.2 (2.4 ± 2.5)	12.2 ± 1.9 (2.6 ± 0.5)	13.6 ± 2.3 (0.7 ± 0.3)
Occipital cortex	0.56 ± 0.09 (1.7 ± 1.3)	0.11 ± 0.04 (7.7 ± 6.0)	1.60 ± 0.80 (9.4 ± 6.4)	13.4 ± 2.1 (2.5 ± 2.3)	11.5 ± 1.9 3.2 ± 0.6)	13.2 ± 2.3 (0.7 ± 0.3)
Cingulate cortex	0.59 ± 0.09 (2.5 ± 1.6)	0.13 ± 0.08 (12.5 ± 7.8)	2.35 ± 1.56 (13.9 ± 7.1)	15.7 ± 2.9 (2.4 ± 2.3)	14.0 ± 2.4 (3.0 ± 0.5)	15.8 ± 3.1 (0.7 ± 0.3)
Frontal cortex	0.56 ± 0.08 (2.1 ± 1.5)	0.12 ± 0.07 (10.5 ± 7.9)	2.30 ± 1.65 (12.0 ± 7.2)	15.8 ± 3.1 (2.5 ± 2.4)	13.8 ± 2.5 (2.9 ± 0.5)	15.6 ± 3.3 (0.8 ± 0.5)
Parietal cortex	0.57 ± 0.09 (1.8 ± 1.2)	0.11 ± 0.05 (9.1 ± 6.2)	1.94 ± 1.07 (10.9 ± 6.1)	15.1 ± 2.7 (2.5 ± 2.4)	13.1 ± 2.3 (3.1 ± 0.6)	15.0 ± 3.0 (0.7 ± 0.3)
Corpus callosum	0.30 ± 0.06 (4.1 ± 1.8)	0.12 ± 0.06 (21.0 ± 8.5)	3.15 ± 2.12 (23.5 ± 9.9)	10.1 ± 1.7 (4.7 ± 4.5)	8.8 ± 1.5 (3.4 ± 0.7)	9.8 ± 1.6 (3.5 ± 2.0)

* One individual had poor fit for data from thalamus using all models tested, and these outlier data from thalamus of this individual were excluded. Regional V_T values were generated using metabolite-corrected arterial input function and 90-min dynamic data.

Data are mean ± SD, with %COV for each estimated parameter in parentheses.

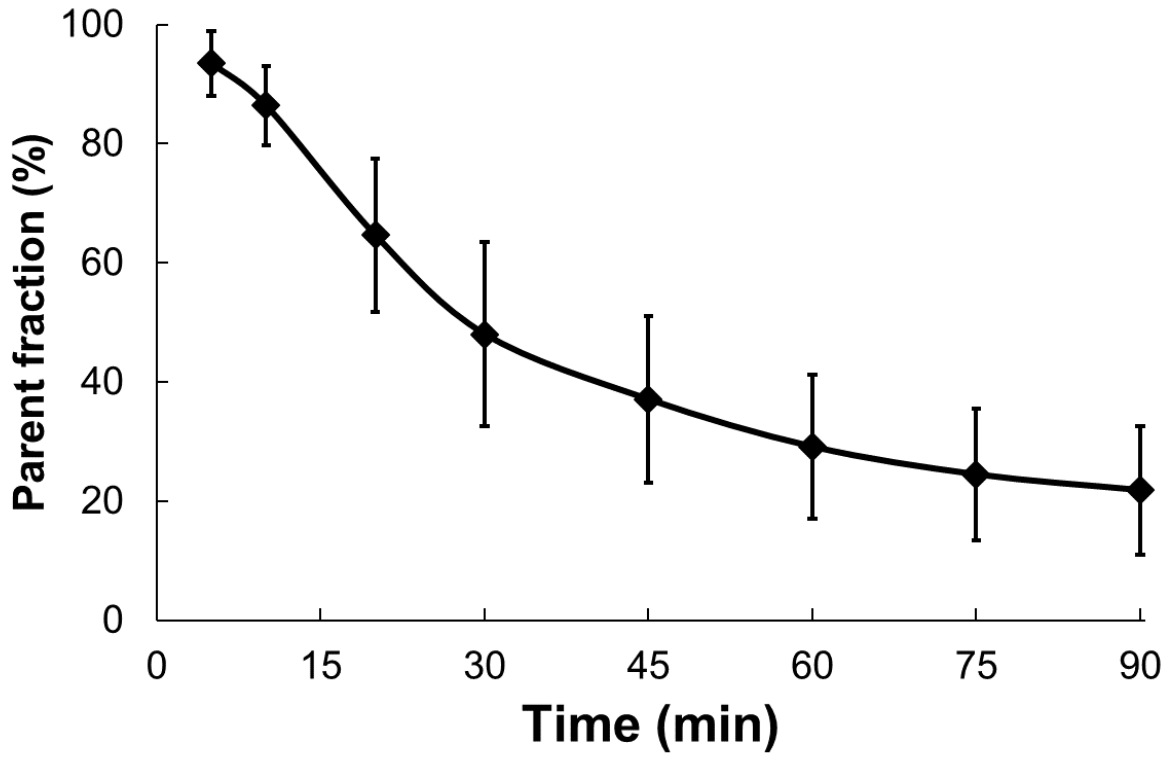

Supplemental Figure 4-1. [^{18}F]XTRA parent fraction (%) plotted over the 90 minute scan duration. Mean data (black diamonds) are plotted from the 17 healthy individuals at each measured time point, with error bars reflecting the population standard deviations.

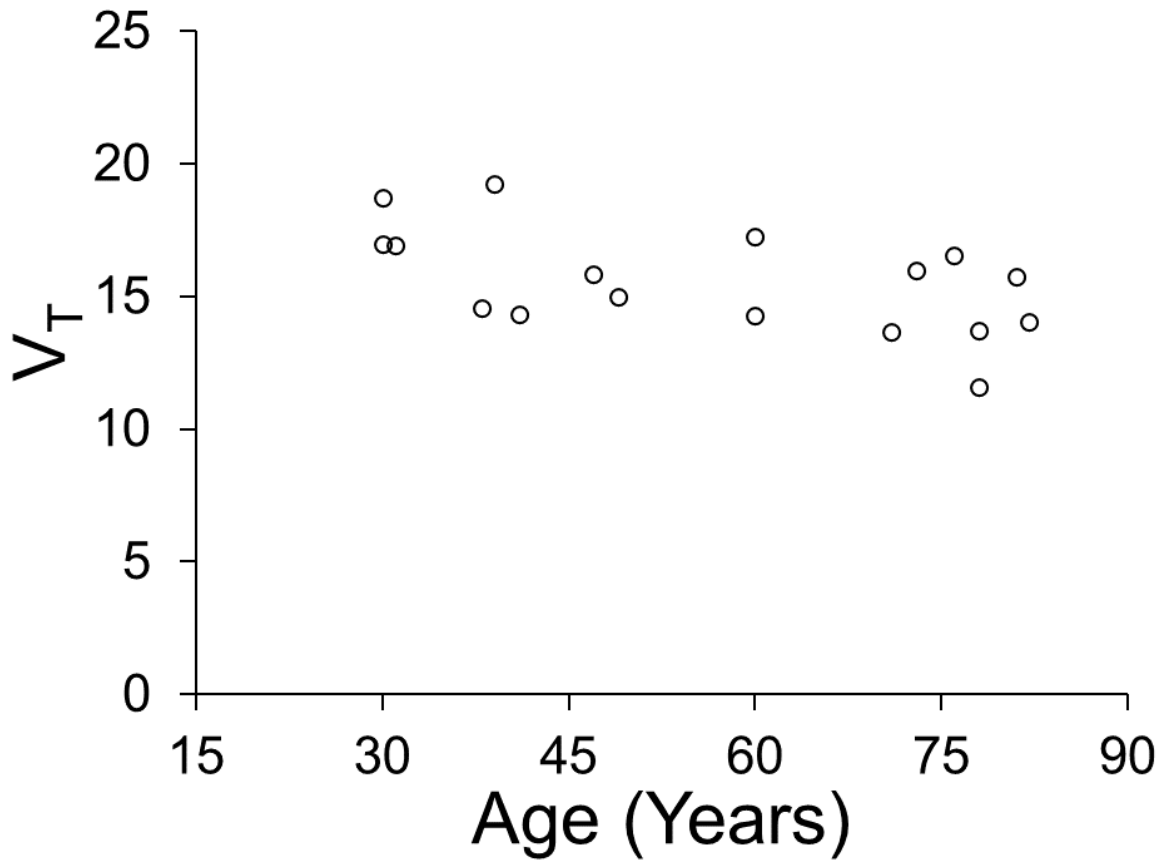

Supplemental Figure 4-2. Scatter plot of [^{18}F]XTRA total distribution volume values (V_T) in the hippocampus from 17 healthy individuals plotted against age.

Regional V_T was estimated using metabolite-corrected arterial input function and Logan analysis (t* = 45 minutes) from 90 minute [^{18}F]XTRA data. Using Spearman's rank-order correlation analysis, there was an inverse correlation between age and regional [^{18}F]XTRA V_T in hippocampus (*rho* = -0.589, *P* = 0.014). V_T is in units of mL cm^{-3}.

Supplemental Table 4-1. Regional volume measurements within the study population of 17 healthy individuals.

ROI	ROI Volume*	ROI Volume Ratio*
Thalamus	15.5 ± 1.8	0.010 ± 0.001
Striatum	18.3 ± 2.4	0.012 ± 0.002
Hippocampus	8.3 ± 0.8	0.005 ± 0.001
Cerebellar CTX	101 ± 10.5	0.066 ± 0.006
Temporal CTX	89.9 ± 9.1	0.058 ± 0.005
Occipital CTX	44.2 ± 5.9	0.029 ± 0.003
Cingulate CTX	19.6 ± 2.9	0.013 ± 0.002
Frontal CTX	165 ± 15.7	0.107 ± 0.006
Parietal CTX	106 ± 10.4	0.068 ± 0.004
Corpus Callosum	3.4 ± 0.3	0.002 ± 0.000
Total ICV	1544 ± 126.7	N/A

*Presented as Mean ± Standard Deviation. ROI volume is in units of cm^3. Volume relative to total intracranial volume (ICV) is defined as volume ratio and is unitless. Region of Interest, ROI; Cortex, CTX; Intracranial Volume, ICV.

Supplemental Table 4-2. Akaike's Information Criterion values from compartmental modeling applied to 90 minutes dynamic [^{18}F]XTRA PET imaging data in humans (N=17).

ROI	1TCM*	2TCM*
Thalamus	-11.4 ± 22.3	-58.1 ± 28.3
Striatum	38.4 ± 15.9	-26.0 ± 30.6
Hippocampus	58.4 ± 11.3	-14.0 ± 25.9
Cerebellar CTX	32.5 ± 16.1	-40.6 ± 35.1
Temporal CTX	42.4 ± 14.3	-32.6 ± 37.1
Occipital CTX	56.6 ± 14.6	-29.3 ± 37.5
Cingulate CTX	50.1 ± 12.6	-18.2 ± 30.3
Frontal CTX	49.4 ± 13.8	-26.9 ± 32.7
Parietal CTX	52.8 ± 14.8	-27.3 ± 34.4
Corpus Callosum	48.6 ± 15.3	10.5 ± 20.9

*Presented as Mean ± Standard Deviation. Region of Interest, ROI; One-tissue compartment model, 1TCM; Two-tissue compartment model, 2TCM; Cortex, CTX.

Supplemental Table 4-3. The absolute percent difference between [^{18}F]XTRA regional total distribution volume (V_T) values calculated from 90 minutes and from 180 minutes of dynamic data from the same individuals (N = 7).

ROI	Difference between V_T estimates*
Thalamus	4.93 ± 6.29%
Striatum	3.99 ± 4.12%
Hippocampus	4.59 ± 4.42%
Cerebellar CTX	3.07 ± 2.96%
Temporal CTX	3.53 ± 3.09%
Occipital CTX	3.95 ± 3.15%
Cingulate CTX	3.43 ± 3.21%
Frontal CTX	3.46 ± 2.78%
Parietal CTX	4.13 ± 3.04%
Corpus Callosum	4.38 ± 5.43%

Presented as Mean ± Standard Deviation. Regional V_T values in units of mL cm^{-3} were generated using Logan analysis with metabolite-corrected arterial input function and t = 45 minutes. Region of Interest, ROI; Cortex, CTX.

Chapter 5: Examining brain inflammatory processes through kinetic modeling of radiotracers in human clinical studies: A study of [^{18}F]ASEM in healthy aging

Summary:

The focus of this chapter is on the use of [^{18}F]ASEM to study the distribution of the alpha7 nicotinic acetylcholine receptor (α7-nAChR) in healthy aging. In this study, we utilized positron emission tomography to study the distribution of [^{18}F]ASEM in 25 healthy adult volunteers. Using PMOD, we were able to use the time activity curves generated for the 9 regions of interest (ROIs) to characterize the binding of [^{18}F]ASEM to α7-nAChR using a one-tissue compartment model and Logan graphical analysis. We used total distribution volumes (V_T) generated from Logan graphical analysis to test the relationship between age and V_T in the ROIs. Additionally, in a subset of healthy volunteers age 50 and older, we used Logan graphical analysis V_T to test the relationship between V_T and various neuropsychological measures.

The distribution of the alpha7 nicotinic acetylcholine receptor in healthy aging: An in vivo positron emission tomography study with [^{18}F]ASEM

This work has been published and is reprinted here with permission from *Neuroimage.*

Coughlin JM, Du Y, Rosenthal HB, Slania S, Min Koo S, Park A, Solomon G, Vranesic M, Antonsdottir I, Speck CL, Rootes-Murdy K, Lerner A, Rowe SP, Wang Y, Lesniak WG, Minn I, Bakker A, Smith GS, Dannals RF, Kuwabara H, Horti A, Wong DF, Pomper MG. The distribution of the alpha7 nicotinic acetylcholine receptor in healthy aging: An in vivo positron emission tomography study with [^{18}F]ASEM. Neuroimage. 2018 Jan 15;165:118-124.

Abstract

Altered function of the alpha7 nicotinic acetylcholine receptor (α7-nAChR) is implicated in several neuropsychiatric diseases. Nevertheless, studies of the human cerebral α7-nAChR even in healthy aging are limited in number and to postmortem tissue.

Methods

The distribution of the cerebral α7-nAChR was estimated in nine brain regions in 25 healthy volunteers (ages 21–86 years; median 57 years, interquartile range 52 years) using [^{18}F]ASEM with positron emission tomography (PET) imaging. Regional total distribution volume (V_T) measurements were calculated using the Logan method from each subject's 90 min dynamic PET data and their metabolite-corrected plasma input function. Spearman's rank or Pearson's correlation analysis was used depending on the normality of the data. Correlation between age and regional 1) volume relative to intracranial volume (volume ratio) and 2) [^{18}F]ASEM V_T was tested. Correlation between regional volume ratio and [^{18}F]ASEM V_T was also evaluated. Finally, the relationship between

[^{18}F]ASEM V_T and neuropsychological measures was investigated in a subpopulation of 15 elderly healthy participants (those 50 years of age and older). Bonferroni correction for multiple comparisons was applied to statistical analyses.

Results

A negative correlation between tissue volume ratio and age was observed in six of the nine brain regions including striatum and five cortical (temporal, occipital, cingulate, frontal, or parietal) regions. A positive correlation between [^{18}F]ASEM V_T and age was observed in all nine brain regions of interest (ROIs). There was no correlation between [^{18}F]ASEM V_T and volume ratio in any ROI after controlling for age. Regional [^{18}F]ASEM V_T and neuropsychological performance on each of eight representative subtests were not correlated among the well-performing subpopulation of elderly healthy participants.

Conclusions

Our results suggest an increase in cerebral α7-nAChR distribution over the course of healthy aging that should be tested in future longitudinal studies. The preservation of the α7-nAChR in the aging human brain supports the development of therapeutic agents that target this receptor for use in the elderly. Further study of the relationship between α7-nAChR availability and cognitive impairment over aging is needed.

Introduction

The alpha7 nicotinic acetylcholine receptor (α7-nAChR) is expressed on neurons and has functional roles in synaptic transmission, neurotransmitter release, intracellular signaling, and synaptic plasticity that collectively mediate cognitive function[118]. Human post-mortem studies support altered distribution of the cerebral α7-nAChR in neuropsychiatric illness, including studies of schizophrenia[119,120] and Alzheimer's disease[121]. Since there is evidence implicating the α7-nAChR in various disease processes, the utility of new therapies targeting the α7-nAChR is being evaluated in

patient populations with cognitive or affective symptoms[122–128]. Nevertheless, our understanding of the availability of the α7-nAChR even in healthy aging is incomplete since studies of human brain tissue that focus on this receptor subtype are limited in number and to a narrow selection of examined regions[129]. New techniques designed to image the α7-nAChR in vivo promise to help elucidate changes in the distribution of the cerebral α7-nAChR in healthy aging and disease [130,131].

A radioligand for imaging the α7-nAChR, [^{18}F]ASEM, was developed by our group[130] and has shown promising pharmacokinetic characteristics in early human neuroimaging studies using positron emission tomography (PET)[132,133]. [^{18}F]ASEM enters the brain rapidly and within 15–30 min after intravenous (IV) bolus radiotracer injection the standardized uptake values peak around 3.0–4.5 before gradual decline in all regions. Two recent studies using this radiotracer in human neuroimaging support the use of graphical analysis (plasma reference graphical analysis [PRGA], multilinear analysis method [MA1]) to derive the primary binding outcome, regional total distribution volume (V_T), using data from at least 90 min of dynamic imaging[132,133]. The test-retest variability of [^{18}F]ASEM human PET data was 10.8 ± 5.1% and 11.7 ± 9.8% across the brain regions tested in these two independent studies of healthy controls.

Here, we aimed to use [^{18}F]ASEM PET-based neuroimaging in a new group of healthy individuals to investigate the availability of the α7-nAChR within the context of healthy aging. We focused on the binding of [^{18}F]ASEM in nine regions, including those suspected to have lower (thalamus, frontal cortex) or unchanged (hippocampus, striatum) availability of the α7-nAChR in the aged brain based on limited results using α-bungarotoxin or assay of mRNA in human postmortem tissue[134–137]. Since decline in cholinergic signaling is seen across the lifespan and may be linked to compensatory re-distribution of the α7-nAChR or to cognitive deficits in elderly individuals, we also assessed the relationship between regional [^{18}F]ASEM V_T and 1. Regional brain volume as well as 2. Cognitive performance, the latter among the subset of participants who were 50 years of age or older.

Materials and Methods

Human Subjects

A Johns Hopkins Institutional Review Board approved this study and all participants provided written informed consent. Use of [^{18}F]ASEM is conducted under a FDA exploratory IND. Healthy adult (over age 18 years) participants were recruited through local advertising. Each subject completed a careful clinical interview and physical assessment with screening blood work, electrocardiogram (EKG), and urine toxicology. Eligibility criteria included stable health, with no clinical abnormality on a screening health assessment and the structural magnetic resonance imaging (MRI). Exclusion criteria included nicotine use, any current or past psychiatric or neurological illness (including history of head injury with loss of consciousness), history of recreational substance abuse including marijuana (assessed by self-report and urine toxicology), prescribed medication known to affect acetylcholine signaling (including but not limited to anticholinergic and certain $5HT_3$ anti-emetic medications), any current psychotropic medication use, contraindication to MRI (i.e. implanted metal, claustrophobia), or contraindication to PET imaging with arterial line placement (i.e. clotting factor deficiency, pregnancy/breast feeding, prior radiation exposure). Participants completed the Mini Mental State Examination (MMSE)[138] to assess global cognitive performance. Older participants (age 50 years and older) in this study were also assessed using a battery of neuropsychological tests. We chose to focus on eight representative subtests from this comprehensive battery to characterize performance of these elderly participants across the neurocognitive domains of attention [Digit Span Forwards from Wechsler Adult Intelligence Scale Third Edition[139]; Delis-Kaplan Executive Functioning System (DKEFS)[140] Number Sequencing Time], working memory [DKEFS Number-Letter Sequencing Time], language [DKEFS Category Fluency], executive function [DKEFS Letter Fluency], visuospatial ability [Clock Drawing Test[141]], and verbal learning and memory [California Verbal Learning Test (CVLT)[142] Total Recall from Trials 1–5; CVLT Long Delay Free Recall].

DNA Extraction and Genotyping

A blood sample was collected from those participants age 50 years and older for DNA extraction (PureGene® Blood Core Kit C, Qiagen, Valencia, CA) according to manufacturer's instructions. Genotyping of the two single nucleotide polymorphisms (SNPs) that determine the three possible alleles of the gene for apolipoprotein E, *APOE*, was completed using TaqMan genotyping assays (rs429358: cat# 4351379, rs7412: cat# 4351379, Applied Biosytems, Foster City, CA) on a CFX96 Touch™ Real-Time PCR Detection System (Bio-Rad, Hercules, CA). Analyses of the six different *APOE* genotypes: *ε*2/*ε*2, *ε*3/*ε*3, *ε*4/*ε*4, *ε*2/*ε*3, *ε*2/*ε*4, and *ε*3/*ε*4 were completed using the CFX Manager™ Software (Bio-Rad, Hercules, CA). Individuals with at least one *ε*4 allele were categorized as APOE *ε*4 carriers.

In Vivo Brain Imaging

Radiotracer synthesis and PET acquisition

[^{18}F]ASEM was synthesized as previously described by one-step microwave radiosynthesis via the corresponding nitro-precursor[143], and met all U.S. Pharmacopeia Convention Chapter <823> acceptance testing criteria. Radiochemical purity at end of synthesis was >98% with high specific radioactivity (2306 ± 2164 GBq/μmol) at the time of IV bolus radiotracer injection and onset of the dynamic listmode PET acquisition. The average injected dose of radioactivity was 510.1 ± 41.0 MBq with injected mass of 0.19 ± 0.17 μg.

PET acquisition

A thermoplastic mask was fitted to each subject's face for immobilization and positioning of the head during scanning. PET continuous listmode data were acquired using a High Resolution Research Tomograph scanner (HRRT, Siemens Healthcare, Knoxville,TN), an LSO-based, dedicated brain PET scanner with <2.5 mm reconstructed image resolution[104]. Four participants (two females with ages 26 and 82 years, and two males with ages 25 and 67 years) underwent data collection for 120 min. This longer scan time was used to validate further the use of a 90 min emission scan. Ninety min of continuous listmode data were acquired from each subsequent participant. One hundred and

twenty min of listmode data were binned into 36 frames (four 15 s, four 30 s, three 1 min, two 2 min, five 4 min, and eighteen 5 min frames). Ninety min of listmode data were binned using the same frame protocol with six less 5 min frames (total of 30 frames). The data were then reconstructed using the iterative ordinary-Poisson ordered-subset expectation-maximization algorithm (6 iteration and 16 subsets, 2 mm post-smoothing), with correction for radioactive decay, dead time, attenuation, scatter and randoms[80]. The attenuation maps were generated from 6 min transmission scans performed with a ^{137}Cs point source prior to the emission scans. The reconstructed image volume spanned 31 cm × 31 cm transaxially and 25 cm axially. The image matrix consisted of 256 × 256 x 207 voxels and a voxel size of 1.22 × 1.22 × 1.22 mm^3.

Plasma sampling

All participants underwent radial arterial line placement prior to radiotracer injection. Measurement of the arterial plasma input function was conducted through collection of 35–50 blood samples (1 mL) that were obtained at the following intervals after bolus radiotracer injection (p.i.): as fast as possible for the initial 1.5 min p.i., every 30 s between 1.5 and 3 min p.i., once at 5 min p.i., and then every 5 min for the duration of the 90 or 120 min continuous emission scan. The fraction of parent radioligand in plasma was determined by high performance liquid chromatography (HPLC) analysis from collection of 3–6 mL blood samples before radiotracer injection (background) and at 5, 10, 20, 30, 45, 60, 75, and 90 min p.i. Scans lasting 120 min had additional blood sampling for metabolite measurements at 105 and 120 min p.i.

Briefly, the modified column-switching HPLC method[105] used an Agilent Technologies system containing a 1 260 Infinity quaternary pump, a 1 260 Infinity column compartment module, a 1260 Infinity UV detector, and a Bioscan radiation detector that was controlled by OpenLab CDS EZChrom (A.01.04) software. Each plasma sample (1–2 mL) was loaded onto a 4 mL Rheodyne injector loop and was initially directed to the capture column (packed with Phenomenex Strata-X 33 µm polymeric reversed phase sorbent) and detectors using 1% acetonitrile and 99% water mobile phase at 2 mL/min to detect polar metabolites. After 2 min of elution, an analytical mobile phase

composed of 40% acetonitrile and 60% aqueous triethylamine at a concentration of 0.1 M and pH = 7.1 (adjusted with phosphoric acid) was applied to elute trapped non-polar metabolites and parent radiotracer onto an analytical column (Waters, reverse phase XBridge BEH C18 5 µM 4.6 × 250 mm) at 2 mL/min.

Measurement of Plasma Free Fraction (f_P)

Plasma Free Fraction (f_P) was measured using rapid equilibrium dialysis (RED). Plasma samples were isolated by centrifugation from one blood sample obtained from each participant before radiotracer injection. A 300 µL sample of plasma was spiked with 3 µCi of [^{18}F]ASEM and added into the sample chamber of Single-Use RED Plate with Inserts (Thermo Scientific, Rockford, IL, USA) with an 8 K molecular-weight cutoff. 500 µL of PBS was added to the buffer chamber and the plate was incubated on an Incubating Microplate Shaker (Fisher Scientific, Waltham, MA, USA) at 37 °C for 4 h. 100 µL of plasma and 100 µL of PBS were transferred to a clean tube. All samples were measured in triplicate. The radioactivity was measured using a 2 480 WIZARD^2 Gamma Counter (Perkin Elmer, Waltham, MA, USA) to obtain the radioactivity in the plasma (C_P) and buffer (C_U). The free, unbound fraction (f_P) was calculated as: $f_P = C_U/C_P$ x 100 (%).

MRI acquisition

MR structural T1-weighted imaging was acquired on a Siemens MAGNETOM Prisma or on a Siemens MAGNETOM Trio 3 Tesla scanner (Malvern, PA, USA) with a Trio head matrix 12-channel head coil or Prisma head/neck 20-channel head coil, to obtain a 0.8 × 0.8 × 0.8 mm^3 3-dimensional (3D) Magnetization-Prepared Rapid Gradient-Echo (MP-RAGE) sequence.

Data Analysis and Statistics

Image processing

The software package PMOD (v3.7, PMOD Technologies Ltd, Zurich, Switzerland) was used in the initial PET image processing and kinetic analysis. Inter-frame motion correction was applied post-reconstruction using the motion correction function in PMOD. First, a static reference frame was generated by averaging the frames corresponding to the 30–60 min p.i. Second, the motion

correction was accomplished by rigid matching of the dynamic data to the reference image frame by frame. PET-MRI co-registration was completed as previously described[144]. Cortical reconstruction and volumetric segmentation of T1-weighted MR images were performed with the FreeSurfer image analysis suite (http://surfer.nmr.mgh.harvard.edu/). Nine regions of interest (ROIs) were selected for this study: thalamus, striatum, hippocampus, cerebellar cortex, temporal cortex, occipital cortex, cingulate cortex, frontal cortex and parietal cortex. Total intracranial volume (ICV) was also defined using FreeSurfer, for use in analyses exploring the correlation between age and ROI volume normalized to ICV, herein referred to as regional volume ratio. Correlation between regional volume ratio and binding of [^{18}F]ASEM was also tested. PET time-activity curves (TACs) were generated for all subjects using the ROI definitions.

Calculation of regional total distribution volume (V_T)

The primary PET-based regional binding outcome was total distribution volume, V_T, defined as the ratio of the concentration of the radioligand in brain tissue to that in plasma at equilibrium[81]. The kinetics of [^{18}F]ASEM can be modeled using graphical analysis[132,133]. Here, V_T within each ROI was estimated using Logan graphical analysis[82] with fixed t* = 45 min, which was chosen for its computational simplicity and independence from assumed compartmental characteristics of the data. Regional V_T values generated using Logan analysis with metabolite-corrected arterial input function from 120 min dynamic scans among four participants were compared to V_T values obtained with data shortening down to 90 min in order to validate further the proposed use of 90 min of continuous PET data. Since the 1TCM yields equal[133] or improved[132] model suitability compared to two-tissue compartmental modeling (2TCM), regional V_T values from the Logan method were compared to those generated using one-tissue compartmental modeling (1TCM) using 90 min data for all 25 individuals. Compartmental modeling used a fixed blood volume of 5%. Plasma free fraction (f_P) was measured for 18 of the 25 subjects, with mean ± standard deviation (SD) = 0.05 ± 0.01. Regional V_T corrected for f_P (V_T/f_P) was calculated as a secondary outcome measure for those individuals with measured f_P.

Statistical Analysis

Statistical analyses were performed using SPSS Statistics (Version 23.0, IBM Corp., Armonk, NY, USA). Data were checked for outliers, and descriptive statistics were obtained. Normality of the data was assessed using the Shapiro-Wilk test. The relationships between 1) regional [^{18}F]ASEM V_T values and age (as well as other descriptive variables) and 2) ROI volume ratios and age were tested using Spearman's rank-order correlation analysis since age was found to not be normally distributed across the study population. These analyses were repeated for the secondary binding outcome, regional V_T/f_P.

The threshold for significance for all statistical tests involving regional V_T and regional volume measures accounted for the nine ROIs using a Bonferroni adjusted alpha level of 0.0056 per test (approximately = 0.05/9). The threshold for significance in all statistical tests involving the eight representative neuropsychological tests was set as $P < 0.0063$ (approximately = 0.05/8). Data were expressed as mean ± SD unless otherwise noted.

Results

Human Subject Participation

Twenty-five healthy participants, ranging in ages from 21 to 86 (median 57; interquartile range 52) years participated in [^{18}F]ASEM PET neuroimaging (Table 5-1). Participants had 13–23 years of education. Four of the 25 participants (ages 27.75 ± 5.12 years, range 21–33 years) did not complete the MMSE on the morning of the PET due to late addition of this test variable. MMSE scores among 21 participants ranged from 27 to 30 out of 30 possible points (29.38 ± 0.92). There was no correlation between MMSE and age. All 15 older (defined as age 50 years or older) participants completed the neuropsychological assessment (Table 5-2). Increasing age was not associated with poorer cognitive performance on any of the eight representative tests (Supplemental Table 5-1). Three of the 15 elderly individuals were found to be APOE ε4 carriers.

Regional Volumes

ROI volumes as well as ICV are presented in Table 5-3. Spearman's rank-order correlation analyses revealed negative correlation between regional volume ratio and age in striatum, temporal cortex, occipital cortex, cingulate cortex, frontal cortex, and parietal cortex (Table 5-3,Figure 5-1).

[^{18}F]ASEM PET imaging

Regional V_T values generated using Logan analysis with metabolite-corrected arterial input function from 90 min continuous scans were within 5% of the V_T values obtained using 120 min of continuous [^{18}F]ASEM data (Supplemental Figure 5-1,Supplemental Table 5-2). Using 90 min data, regional V_T values from the Logan method were comparable to V_T values estimated using the 1TCM (Table 5-4). Furthermore, regional V_T values from the Logan method highly correlated with those from using the 1TCM (Spearman's rho = 0.945, $P < 0.001$) (Supplemental Figure 5-2).

Spearman's rank-order correlation analyses revealed no correlation between K_1 and age in all nine regions of interest. Regional V_T values generated using Logan analysis with metabolite-corrected arterial input function from 90 min scan duration were used in all other correlation analyses hereafter, unless otherwise stated.

Spearman's rank-order correlation analyses revealed positive correlation between [^{18}F]ASEM regional V_T values and age in all nine ROIs (Table 5-4,Figure 5-2). Secondary analyses revealed positive correlation between V_T/f_P and age in striatum and parietal cortex (Supplemental Table 5-3), and f_P did not correlate with age. There was no correlation between [^{18}F]ASEM V_T in any of the ROIs and sex, race, body mass index, years of education, or MMSE score. There was no correlation between [^{18}F]ASEM V_T and volume ratio in any ROI after controlling for age (Supplemental Table 5-4). Finally, post hoc analyses revealed positive correlation between [^{18}F]ASEM V_T estimates from the 1TCM and age in six of the nine ROIs (Supplemental Table 5-5).

Among the 15 individuals age 50 years and older, there was no significant correlation found between [^{18}F]ASEM V_T in any ROI and performance on any of the eight representative cognitive measures after Bonferroni correction. However, without correction for multiplicity, a negative correlation ($P < 0.05$) between the DKEFS Number Sequencing Time, a test of attention, and [^{18}F]ASEM V_T in occipital cortex ($rho = -0.534$, $P = 0.040$) was observed, reflecting a trend of poorer performance in those with lower binding in this region (Supplemental Figure 5-3).

Discussion

The relationship between cognitive decline in healthy aging and cholinergic dysfunction is likely related to complex underlying factors that may include loss of cholinergic projections, deficits in acetylcholine signaling with secondary effects on other neurotransmitter release, or changed distribution of nicotinic receptor subtypes[113]. Converging evidence from pharmacological studies and animal models suggests the important role of the α7-nAChR in cognitive function[145]. The ability to estimate the distribution of the α7-nAChR *in vivo* using [^{18}F]ASEM with PET imaging may help elucidate the hypothesized link between cerebral α7-nAChR availability and cognitive decline, even over the healthy human lifespan[130,131].

In the present study, we assessed the relationship between the availability of the α7-nAChR and healthy aging. Using non-parametric (Spearman's rank) correlation analysis, a positive correlation between [^{18}F]ASEM V_T and age was observed in all nine ROIs, which included cortical and subcortical regions. Consistent with previously reported regional decreases in brain volume over normal aging [146–148], we observed a negative correlation between the tissue volume ratio and age in several of these ROIs, namely striatum, temporal cortex, occipital cortex, cingulate cortex, frontal cortex, and parietal cortex. There was no correlation between [^{18}F]ASEM V_T and volume ratio in any ROI after controlling for age. While this study is limited by small sample size, our results support the promising utility of [^{18}F]ASEM neuroimaging to examine the relationship between the distribution of the α7-nAChR, onset of regional brain atrophy, and related clinical changes over the course of

healthy aging. Furthermore, these results suggest a link between higher cerebral availability of the α7-nAChR with aging that may prove important to our understanding of cholinergic signaling over the lifespan. Specifically, these results suggest an increase in the cerebral α7-nAChR, perhaps as a compensatory response to lower acetylcholine signaling, over the course of healthy aging that should be tested in animal models and future longitudinal studies. The preservation of the α7-nAChR over normal aging supports the development of therapeutic agents that target this receptor for treatment of cognitive dysfunction in the elderly.

This study benefits from several methodological strengths including a larger sample size of [^{18}F]ASEM neuroimaging data from healthy individuals compared to two other recent studies[132,133]. [^{18}F]ASEM neuroimaging data from this new group of 25 healthy individuals spanning ages 21–86 years showed that use of the Logan graphical method with metabolite-corrected arterial input function, like other methods of graphical analysis[132,133], yields regional V_T estimates that are similar to those from the preferred compartmental tissue model, the 1TCM[132], using 90 min of continuous dynamic emission data. One hundred and twenty min of emission data were acquired from four (two young and two elderly) of our 25 healthy participants and data shortening showed that V_T estimates from a 90 min scan duration were within 5% of the values estimated from a 120 min scan duration for all ROIs. The methodological design also included careful assessment of neuropsychological performance in those individuals who were 50 years old or older in order to probe the relationship between distribution of [^{18}F]ASEM binding and cognitive performance in late aging. This small subpopulation of 15 elderly controls showed no correlation between performance on the selected neuropsychological subtests and increasing age. Similarly, there were no significant correlations found between regional [^{18}F]ASEM V_T values and cognitive measures among this well-performing population of healthy participants. Nevertheless, the observed trend of a negative correlation between performance on the DKEFS Number Sequencing, a test of attention, and [^{18}F]ASEM V_T in occipital cortex should be tested further in larger studies of aging individuals with more varied

neuropsychological performance given the hypothesized key role of the α7-nAChR in modulating tasks of sustained attention[149].

There are some important methodological and biological factors that should be considered and further investigated in future [^{18}F]ASEM PET imaging studies in aging and disease. First, we defined regional V_T as our primary binding outcome. Since only free radioligand enters brain, we also measured f_P, and calculated regional V_T/f_P as a secondary outcome measure. The values obtained for f_P were 5 ± 1% and therefore very similar to those reported in six healthy participants (7.7 ± 1.3%) by Hillmer et al. However, the correlation between [^{18}F]ASEM binding and age was only observed in striatum and parietal cortex using V_T/f_P as the binding outcome. Since f_P is an independent measurement and may introduce further noise from plasma data, it is possible that [^{18}F]ASEM lacks sensitivity to detect changes in V_T/f_P in all affected ROIs over aging, especially in the setting of small sample size. On the other hand, the limited number of postmortem studies to-date do not report evidence of higher availability of the α7-nAChR in elderly cases[129]. Since amyloid burden in the brain may also be associated with upregulated cerebral expression of the α7-nAChR[150,151], the effect of this potential synergistic relationship should be examined in future *in vivo* or *in vitro* studies. Since there were only three individuals found to be APOE4 carriers in this population, we could not sufficiently test for this effect that could be a focus of future studies. Second, it is important to note that [^{18}F]ASEM PET signal is only an indirect measure of the α7-nAChR in the living brain. Our results support further *in vitro* experiments of the α7-nAChR directly, in carefully selected postmortem tissue from individuals of all ages.

Conclusions

By demonstrating a positive correlation between [^{18}F]ASEM binding and age in several brain regions of healthy individuals, we support future use of [^{18}F]ASEM PET to examine the relationship between altered distribution of the α7-nAChR and clinical changes even over healthy aging. Since there is interest in targeting this receptor subtype to prevent or ameliorate cognitive deficits, human studies using [^{18}F]ASEM in individuals with more robust impairment in cognitive performance will inform

further the lack of observed relationship between [^{18}F]ASEM V_T and performance on neuropsychological tests among elderly participants reported here. [^{18}F]ASEM PET continues to demonstrate promise as a research tool for testing the relationship between altered availability of the cerebral α7-nAChR in clinical populations, toward guiding therapies targeted to this receptor subtype.

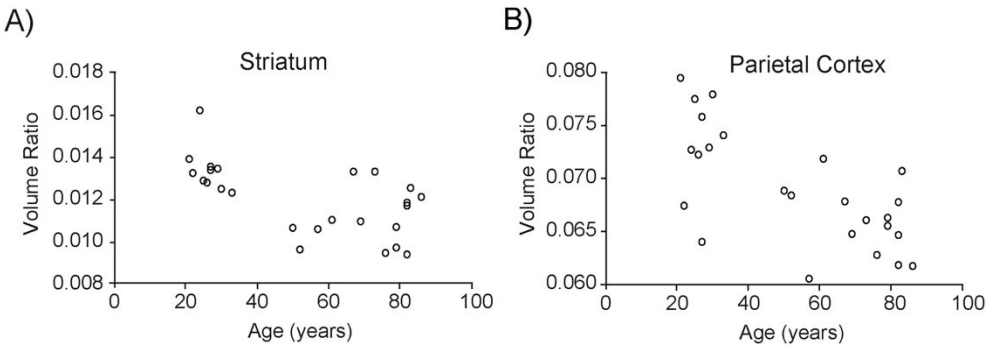

Figure 5-1. Scatter plots of regional volume relative to total intracranial volume (volume ratio) plotted against age. Spearman's rank-order correlation analyses revealed negative correlation between regional volume ratio (unitless) and age in six (striatum, temporal cortex, occipital cortex, cingulate cortex, frontal cortex, and parietal cortex) of the nine regions of interest. Individual data points are shown for two representative regions including A) Striatum (*rho* = −0.605, *P* = 0.001) and B) Parietal Cortex (*rho* = −0.627, *P* = 0.001). Significance was set at *P* < 0.0056 using Bonferroni correction for the nine regions tested.

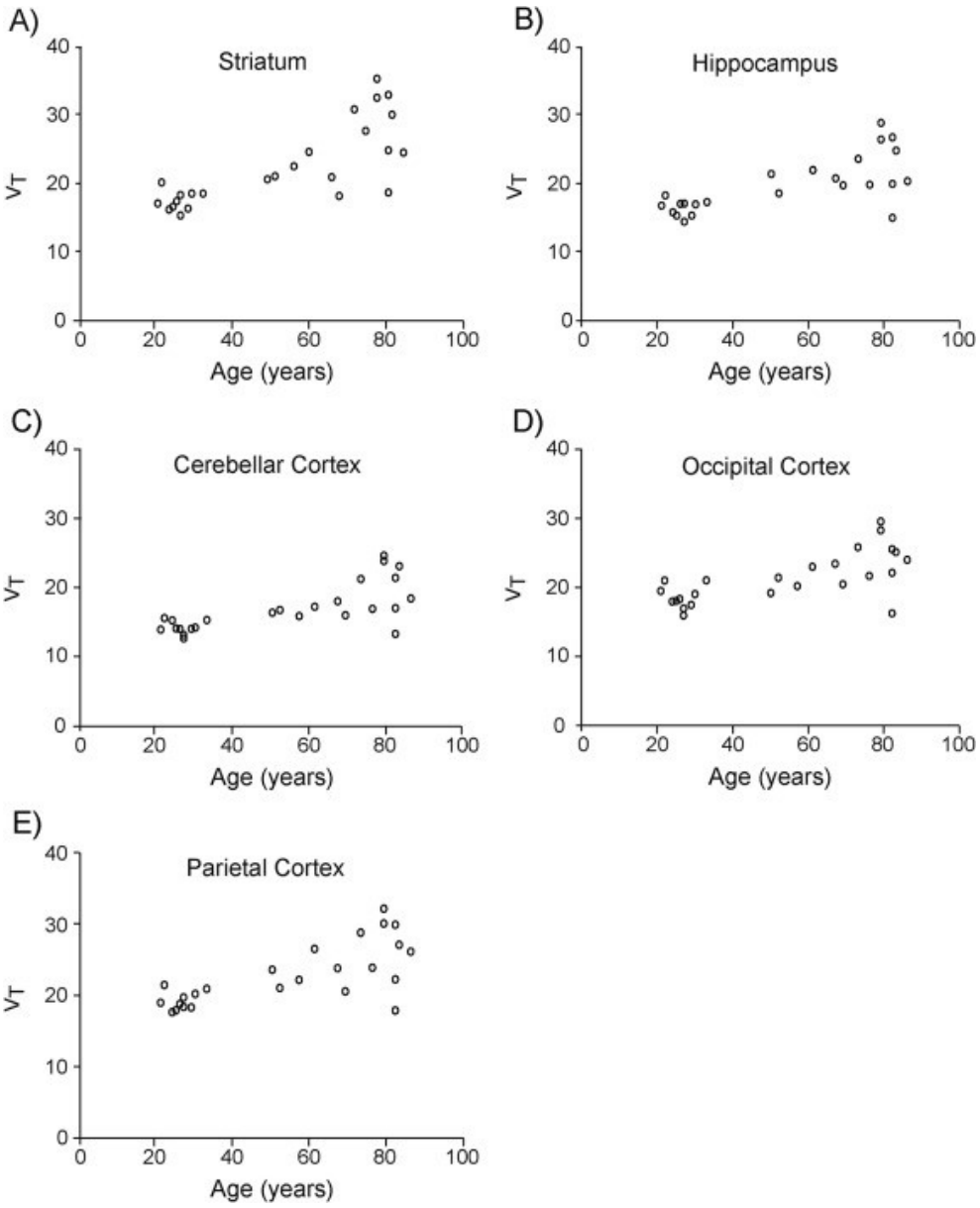

Figure 5-2. Scatter plots of regional [^{18}F]ASEM total distribution volume values (V_T) plotted against age. Regional V_T was estimated using metabolite-corrected arterial input function and Logan analysis (t* = 45 min) from 90 min [^{18}F]ASEM data. Individual data points are shown for five representative regions including A) Striatum, B) Hippocampus, C) Cerebellar Cortex, D) Occipital Cortex and E) Parietal Cortex that were selected from the nine regions studied. Using Spearman's rank-order correlation analysis, all regions of interest in this study showed positive correlation between age and regional [^{18}F]ASEM V_T ($P < 0.0056$, which marks significance after applying Bonferroni correction for the nine regions tested). V_T is in units of mL cm^{-3}.

Table 5-1. Clinical and demographic characteristics of 25 healthy human participants.

Age (Years)	53.68 ± 24.59[a]
Sex (Male/Female)	15/10
Race (Caucasian/African-American)	18/7
Body Mass Index	24.61 ± 3.32
Education (Years)	16.96 ± 2.37

[a]Results are presented as Mean ± Standard Deviation unless otherwise indicated.

Table 5-2. Neuropsychological performance in 15 elderly healthy control subjects.

Test	Elderly Controls[a,b]
Digit Span Forwards[139]	7.2 (0.8) 6-8
DKEFS[140] Number Sequencing Time (seconds)	36.6 (8.3) 19-47
DKEFS Number-Letter Sequencing Time (seconds)	97.7 (53.4) 41.4-272.0
DKEFS Category Fluency (Total number of words generated over 60 s)	39.2 (7.3) 29-57
DKEFS Letter Fluency (Total number of words generated over 60 s)	45.9 (11.1) 31-70
Clock Drawing Test[141]	9.3 (1.1) 6-10
CVLT[142] Total number of words recalled - Sum of Trials 1-5	57.3 (10.5) 41-76
CVLT Long Delay Free Recall (Total number of words recalled – Single Trial)	12.4 (2.9) 7-16

[a]Elderly healthy controls were defined as those participants age 50 years and older and all completed the neuropsychological assessment that included these eight representative tests.

[b]Scores presented as Mean (Standard Deviation) and range. California Verbal Learning Test, CVLT; Delis-Kaplan Executive Functioning System, DKEFS).

Table 5-3. Regional volume measurements within the study population of 25 healthy individuals and correlation between age and regional volume ratio.

ROI	ROI Volume[a]	ROI Volume Ratio[a]	Rho (*P* value)[b]
Thalamus	15.25 ± 1.96	0.010 ± 0.001	-0.438 (0.029)
Striatum	18.05 ± 2.21	0.012 ± 0.002	-0.605 (0.001)*
Hippocampus	8.48 ± 0.80	0.006 ± 0.001	-0.242 (0.243)
Cerebellar CTX	104.83 ± 16.06	0.070 ± 0.009	-0.304 (0.140)
Temporal CTX	92.37 ± 13.20	0.061 ± 0.007	-0.737 (<0.001)*
Occipital CTX	42.98 ± 5.17	0.029 ± 0.003	-0.562 (0.003)*
Cingulate CTX	19.44 ± 3.31	0.013 ± 0.001	-0.710 (<0.001)*
Frontal CTX	165.69 ± 22.78	0.110 ± 0.009	-0.758 (<0.001)*
Parietal CTX	103.95 ± 13.60	0.069 ± 0.005	-0.627 (0.001)*
Total ICV	1509.79 ±169.20	N/A	N/A

*$P < 0.0056$, which marks significance after applying Bonferroni correction for the nine regions tested.

[a]Presented as Mean ± Standard Deviation. ROI volume is in units of cm^3. Volume relative to total intracranial volume (ICV) is defined as volume ratio and is unitless.

[b]Spearman's rank correlation analysis was applied to each test of correlation between age and ROI volume ratio. Cortex, CTX; Region of Interest, ROI.

Table 5-4. K_1 and Total Distribution Volume (V_T) values estimated with the one-tissue compartmental model (1TCM), along with V_T values and Correlation between age and regional V_T estimated using Logan analysis (t* =45 minutes) for [^{18}F]ASEM PET imaging in humans (N=25).

	1TCM		Logan	
ROI	**K_1[a] (mL cm^{-3} min^{-1})**	**V_T[a] (mL cm^{-3})**	**V_T[a] (mL cm^{-3})**	**Rho (*P* value)[b]**
Thalamus	0.36 ± 0.06	21.44 ± 4.68	22.78 ± 5.15	0.591 (0.002)*
Striatum	0.35 ± 0.06	21.82 ± 5.96	22.60 ± 5.97	0.778 (< 0.001)*
Hippocampus	0.27 ± 0.05	17.92 ± 3.38	19.77 ± 3.97	0.666 (< 0.001)*
Cerebellar CTX	0.36 ± 0.06	16.17 ± 3.32	16.92 ± 3.44	0.718 (< 0.001)*
Temporal CTX	0.30 ± 0.05	21.20 ± 3.68	22.30 ± 3.94	0.621 (0.001)*
Occipital CTX	0.38 ± 0.07	20.34 ± 3.48	21.44 ± 3.66	0.652 (< 0.001)*
Cingulate CTX	0.35 ± 0.06	20.78 ± 3.31	21.85 ± 3.51	0.610 (0.001)*
Frontal CTX	0.36 ± 0.07	20.62 ± 4.16	21.45 ± 4.19	0.581 (0.002)*
Parietal CTX	0.36 ± 0.06	21.70 ± 4.18	22.78 ± 4.35	0.670 (< 0.001)*

*P < 0.0056, which marks significance after applying Bonferroni correction for the nine regions tested.

[a]Presented as Mean ± Standard Deviation. Regional V_T values were generated using metabolite-corrected arterial input function and 90 minute dynamic data.

[b]Spearman's rank correlation analysis was applied to each test of correlation between age and regional V_T generated using Logan analysis. Cortex, CTX; Region of Interest, ROI.

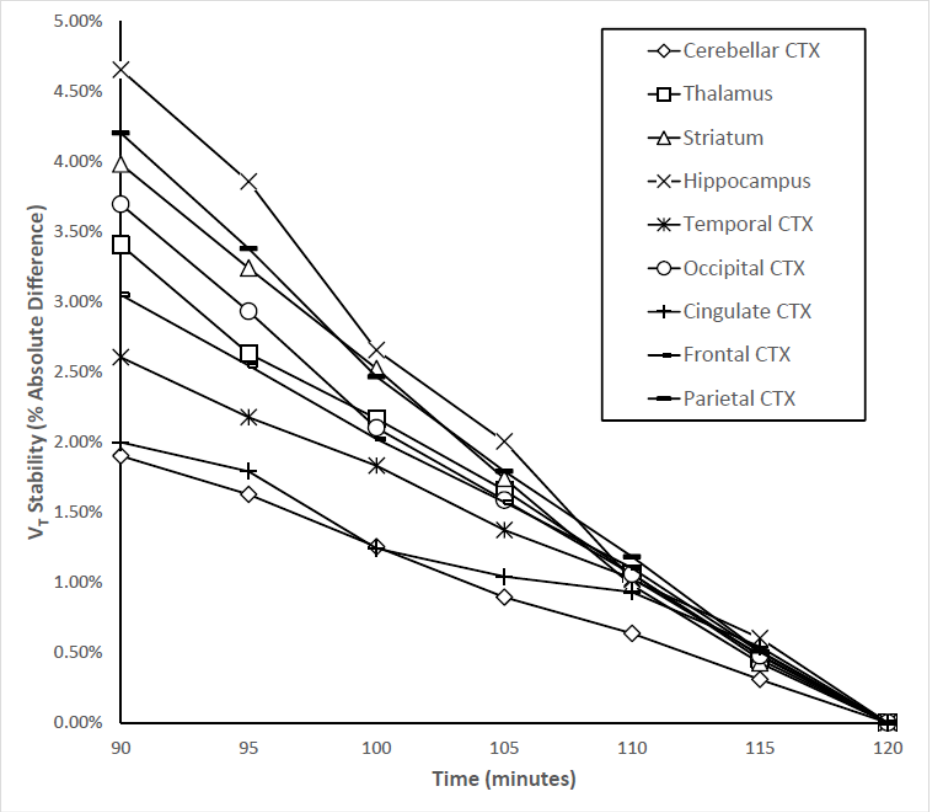

Supplemental Figure 5-1. Assessment of the relative stability in [^{18}F]ASEM regional total distribution volume (V_T) values calculated from 120 minutes of continuous data compared to values produced when the data is truncated by five minute intervals down to 90 minutes of continuous data.

Data from four healthy individuals were included and V_T estimates were in units of mL cm^{-3}. The percent of the absolute difference between the V_T values from 120 minutes of data and V_T values from shortened scan duration are plotted for each of the nine regions of interest. Cortex, CTX.

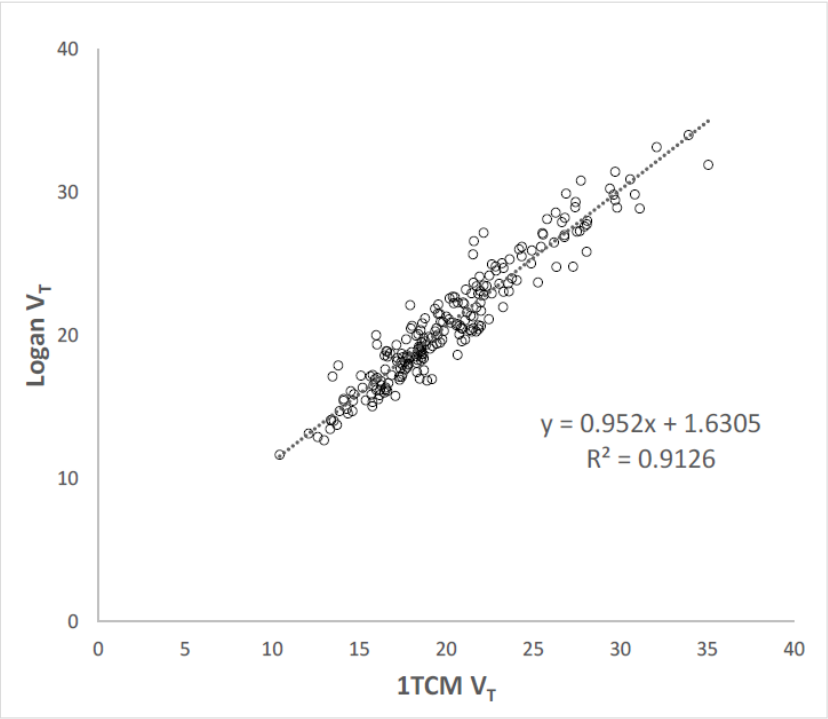

Supplemental Figure 5-2. Comparison between [^{18}F]ASEM regional total distribution volume (V_T) values using 1TCM and Logan graphical analysis using 90 minute data from 25 healthy individuals.

Regional V_T values from the 1TCM were highly correlated with those from the Logan method (Spearman's *rho* = 0.945, $P < 0.001$). Results from secondary regression analysis are also shown. V_T is in units of mL cm^{-3}.

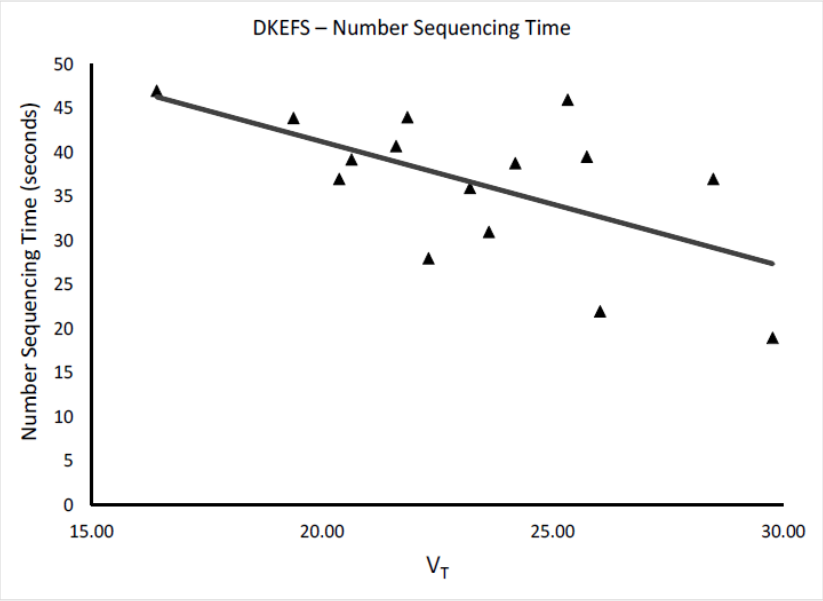

Supplemental Figure 5-3. Scatter plots of timed performance on the Delis-Kaplan Executive Functioning System (DKEFS) Number Sequencing Time test plotted against [^{18}F]ASEM V_T in the Occipital Cortex.

Data was collected from 15 elderly (age 50 years and older), healthy individuals. Regional V_T values were estimated using Logan graphical analysis from 90 minute [^{18}F]ASEM data. Spearman's rank correlation analysis was applied. The negative correlation between timed performance and V_T (*rho* = -0.534, *P* = 0.040) did not survive statistical significance (*P* < 0.0063, which marks significance after applying Bonferroni correction for the eight representative neuropsychological tests). A line from secondary regression analysis is also shown. V_T is in units of mL cm^{-3}.

Supplemental Table 5-1. No significant correlation was observed between age and neuropsychological test performance among 15 healthy individuals who were age 50 years or older.

	Neuropsychological Tests							
	Attention		WM	Lang	Exec	Visuospatial ability	Verbal Learning and Memory	
	DSF	#	#-Let	Cat	LF	CDT	Recall	Delay
Age	0.121	0.103	0.077	0.166	-0.058	0.176	0.121	0.286

[a]Spearman's rank was used to test correlation between age and each neuropsychological test and the value for *rho* is presented. No significant correlation was observed even using a threshold of significance of $P < 0.05$, which does not account for multiple comparisons. Working Memory, WM; Language, Lang; Executive Function, Exec; Digit Span Forward, DSF; Delis-Kaplan Executive Functioning System (DKEFS) Number Sequencing Time, #; DKEFS Number-Letter Sequencing Time, #-Let; DKEFS Category Fluency, Cat; DKEFS Letter Fluency, LF; Clock Drawing Test, CDT; CVLT Total Recall Trials 1-5, Recall; CVLT Long Delay Free Recall, Delay.

Supplemental Table 5-2. The absolute percent difference between [^{18}F]ASEM regional total distribution volume (V_T) values calculated from 90 minutes of dynamic data and the values from 120 minutes of dynamic data from the same individuals (N = 4).

ROI	Difference between V_T estimates[a]
Thalamus	3.41 ± 4.30%
Striatum	3.98 ± 3.80%
Hippocampus	4.65 ± 4.36%
Cerebellar CTX	1.90 ± 1.98%
Temporal CTX	2.61 ± 3.60%
Occipital CTX	3.69 ± 3.51%
Cingulate CTX	2.00 ± 2.28%
Frontal CTX	3.05 ± 3.21%
Parietal CTX	4.20 ± 3.96%

[a]Presented as Mean ± Standard Deviation. Regional V_T values in units of mL cm^{-3} were generated using Logan analysis with metabolite-corrected arterial input function and a fixed t* at 45 minutes. Cortex, CTX; Region of Interest, ROI.

Supplemental Table 5-3. Correlation between age and regional [^{18}F]ASEM Total Distribution Volume corrected for plasma free fraction (V_T/f_P).

ROI	V_T/f_P[a]	Rho (*P* value)[b]
Thalamus	519.36 ± 138.31	0.571 (0.013)*
Striatum	532.45 ± 147.54	0.674 (0.002)**
Hippocampus	456.77 ± 111.29	0.573 (0.013)*
Cerebellar CTX	394.70 ± 96.56	0.587 (0.010)*
Temporal CTX	509.66 ± 114.43	0.557 (0.016)*
Occipital CTX	495.68 ± 113.75	0.564 (0.015)*
Cingulate CTX	502.25 ± 106.32	0.380 (0.120)
Frontal CTX	493.97 ± 115.60	0.625 (0.006)*
Parietal CTX	524.68 ± 123.33	0.648 (0.004)**

[a]V_T/f_P was measured in 18 of 25 total healthy individuals and presented as Mean ± Standard Deviation. [b]Spearman's rank correlation analysis was applied to each test of correlation between age and V_T/f_P. Cortex, CTX; Region of Interest, ROI. **P* < 0.05, which does not account for multiple comparisons in these exploratory analyses. ***P* <0.0056, which marks significance after applying Bonferroni correction for the nine regions tested. V_T/f_P is in units of mL cm^{-3}.

Supplemental Table 5-4. Lack of correlation between regional [^{18}F]ASEM Total Distribution Volume (V_T) and regional volume ratio after controlling for age among 25 healthy individuals.

ROI	Rho (*P* value)[a]
Thalamus	-0. 123 (0.568)
Striatum	-0.202 (0.344)
Hippocampus	0.070 (0.746)
Cerebellar CTX	0.015 (0.946)
Temporal CTX	0.023 (0.914)
Occipital CTX	0.431 (0.035)*
Cingulate CTX	0.296 (0.161)
Frontal CTX	0.252 (0.236)
Parietal CTX	-0.046 (0.832)

[a]Pearson's correlation analysis was applied to test correlation between regional V_T (in units of mL cm^{-3}) and the volume ratio (volume relative to intracranial volume, unitless), controlling for age. Cortex, CTX; Region of Interest, ROI. Results from each region did not meet the criteria for significance (P <0.0056, which marks significance after applying Bonferroni correction for the nine regions tested). *P < 0.05, which does not account for multiple comparisons.

Supplemental Table 5-5. Correlation between age and regional V_T estimated using the one-tissue compartmental model (1TCM) for [^{18}F]ASEM PET imaging in humans (N=25).

ROI	Rho (*P* value)[a]
Thalamus	0.534 (0.006)
Striatum	0.704 (<0.001)*
Hippocampus	0.630 (0.001)*
Cerebellar CTX	0.652 (<0.001)*
Temporal CTX	0.513 (0.009)
Occipital CTX	0.554 (0.004)*
Cingulate CTX	0.548 (0.005)*
Frontal CTX	0.519 (0.008)
Parietal CTX	0.559 (0.004)*

Regional V_T values in units of mL cm^{-3} were generated using metabolite-corrected arterial input function and 90 minute dynamic data. [a]Spearman's rank correlation analysis was applied to each test of correlation between age and regional V_T generated using 1TCM. Cortex, CTX; Region of Interest, ROI. *P < 0.0056, which marks significance after applying Bonferroni correction for the nine regions tested.

Chapter 6: Synthesis and initial *in vitro* assessment of peptide-based agents targeting death receptor 5

Summary:

This chapter is focused on the development of peptide-based agents targeting death receptor 5 (DR5). It details the synthesis of four peptide candidates from peptide design to solid state peptide synthesis and then finally to the cyclization of peptide candidates. These peptides were then tested for their ability to bind DR5 via flow cytometry in colorectal cancer cells.

Introduction

A member of the tumor necrosis factor (TNF) receptor superfamily, death receptors (DRs) can trigger apoptosis pathways upon binding of TNF-related apoptosis-inducing ligand (TRAIL). Binding of TRAIL to the receptors allows them to trigger both intrinsic and extrinsic apoptosis pathways[152]. These death receptors fall in to two categories, death domain containing receptors and decoy receptors[153]. In humans, there are two death domain containing receptors, TRAIL-R1 (DR4) and TRAIL-R2 (DR5), that upon binding with TRAIL, form a death inducing signaling cascade and trigger apoptosis. The three decoy receptors in humans, TRAIL-R3, TRAIL-R4, and osteoprotegerin (OPG), can bind TRAIL but due to a lack of or truncated death domain, they are unable to trigger apoptosis. These decoy receptors are seen to inhibit TRAIL-mediated apoptosis by binding TRAIL and lowering the concentration of TRAIL available to bind DR4 and DR5[154].

TRAIL-based therapies have been highly studied in cancer, due to the attractive potential of TRAIL to trigger apoptosis through extrinsic pathways[155]. This lead to clinical studies using recombinant TRAIL which, although showing broad tolerability in humans, failed to show any robust therapeutic benefit in humans due to its short half-life and TRAIL-resistance in cancer[156,157]. To overcome the short-half life of TRAIL, our collaborators have developed a PEGylated recombinant human TRAIL ($TRAIL_{PEG}$)[158–160], that has shown promising therapeutic potential and has a > 16 fold longer half-life in monkeys compared to human TRAIL[33]. Recently, they have discovered a new therapeutic potential for TRAIL in non-cancer related diseases, including liver fibrosis, rheumatoid arthritis, and scleroderma[30,33,161]. While these studies show promising results, they lack an effective mechanism to monitor disease intervention non-invasively, slowing down the progress of this potentially life-saving therapy.

To enable assessment of such therapy, I endeavor to image engagement of death receptor 5 (DR5), the receptor through which TRAIL-mediated effects occur[5], directly. Imaging of DR5 *in vivo* will also provide a powerful tool to assess not only fibrosis but in a variety of conditions in which the extrinsic

apoptotic pathway is involved, including rheumatological conditions[162], diabetes[163], and cardiovascular disease[164]. Our colleagues have identified a new set of peptides that are specifically targeted toward DR5. The coupling of imaging moieties with targeted peptides has proved to be an effective strategy that establishes a specific and targeted molecular imaging approach to monitoring disease[7]. I intend to use this approach to functionalize novel DR5-targeted peptide candidates and assess the ability of these candidates to bind DR5 in *in vitro.*

Methods

General Procedures

Solvents of analytical or HPLC grade were purchased from commercial sources and were used as received. Fluorenylmethyloxycarbonyl-*S*-acetamidomethyl-L-cysteine 4-alkoxybenzyl alcohol resin (Fmoc-L-Cys(Acm) Wang resin), Fmoc-L-Cys(Acm)-OH, and Fmoc-protected amino acids were purchased from Chem Impex Intl. Inc (Wood Dale, IL). Arginine was protected with 2,2,4,6,7-pentamethyldihydro-benzofuran-5-sulfonyl (Pbf). Asparagine, glutamine, and histidine were protected with trityl (Trt). Aspartic acid and glutamic acid were protected with β-tert-butyl (OtBu). Lysine and Tryptophan were protected with tert-butyloxycarbonyl (Boc). Serine, threonine, and tyrosine were protected with *tert*-butyl (tBu). Ethyl cyano(hydroxyamino)acetate (Oxyma) was purchased from CEM. 6-Carboxyfluorescein (6-FAM) was purchased from Astatech. All other reagents were purchased from Sigma Aldrich. Low-resolution electrospray ionization-mass spectrometry (ESI-MS) data were obtained using an Agilent Technologies 1260 series LCMS Single Quad System connected to a variable wavelength detector.

Solid State Peptide Synthesis of Acm-protected peptides

Linear peptide synthesis was carried out on a CEM Liberty Blue Automated peptide synthesizer using a traditional Fmoc protection strategy at a reaction scale of 0.1 mmol. Fmoc protecting groups were removed using 20% piperidine in dimethylformamide (DMF), followed by activation of carboxyl groups and amino acid coupling. Fmoc-L-Cys(Acm)-resin was used for all syntheses. Once synthesis was complete, the peptide-resin was removed from the synthesizer and transferred to a

filtered reaction vessel. Resin cleavage and global deprotection of protecting groups was done concurrently, based on a protocol by Pedersen et al.[165] The peptide-resin was washed three times with DMF, followed by three washes with dichloromethane (DCM), and dried under high vacuum for 1-4 hours. Resin cleavage and global deprotection of protecting groups was achieved using a cleavage cocktail of trifluoroacetic acid (TFA)/water (H_2O)/triisopropalsilane (18/1/1). The peptide-resin was suspended in 5 mL of cleavage cocktail and rocked for 2 hours at room temperature (RT). Following cleavage, the peptide was filtered from the resin, the resin was washed with TFA, and the peptide was precipitated with cold diethyl ether. The precipitate was centrifuged for 5 minutes at 4000 revolutions per minute (RPM), producing a peptide pellet and a diethyl ether supernatant. The ether was decanted, the peptide was washed twice more with diethyl ether, and the peptide pellet was dried with forced air before being prepared for lyophilization or high performance liquid chromatography purification.

High Performance Liquid Chromatography (HPLC) purification of Acm-protected peptides

Reverse phase high performance liquid chromatography was performed on an Agilent Technologies 1260 Infinity semi-preparative HPLC system (Wilmington, DE) equipped with a Phenomenex, C18 Luna, 10u, 10 x 250 mm^2 column at a 10 mL/min flow rate. Peptides were eluted using a gradient of H_2O containing 0.1% TFA and acetonitrile containing 0.1 % TFA. Peptides were detected at 215, 255, and 450 nm wavelengths. The following gradients were used for each candidate peptide:

DP1-ACM-FAM: 10%-60% Acetonitrile + 0.1% TFA: H2O + 0.1% TFA in 30 minutes. DP1-ACM-FAM was eluted at 11.92 minutes.

DP2-ACM-FAM: 15%-30% Acetonitrile + 0.1% TFA: H_2O + 0.1% TFA in 30 minutes. DP2-ACM-FAM was eluted at 4.73 minutes.

DP3-ACM-FAM: 10%-60% Acetonitrile + 0.1% TFA: H_2O + 0.1% TFA in 30 minutes. DP3-ACM-FAM was eluted at 9.13 minutes.

DP4-ACM-FAM: 15%-75% Acetonitrile + 0.1% TFA: H_2O + 0.1% TFA in 30 minutes. DP3-ACM-FAM was eluted at 6.06 minutes.

Peak-based fraction collection was completed using the automatic fraction collector integrated into the Agilent system by setting a peak absorbance threshold. Collected fractions were combined, concentrated on the rotary evaporator, and lyophilized. Lyophilized products were stored at -20 °C until ESI-MS characterization.

Cyclization of Acm-protected peptides

Cyclization of Acm-protected peptides was adapted from the protocols of Andreu et al.[166] and Zhang et al.[167] The Acm-protected peptide was dissolved in 4:1 glacial acetic acid: H_2O to reach a final concentration of 100 µmol/100 mL. The solution was stirred at 25 °C and protected from light. To start the reaction, 5 equivalents of iodine (I_2) per Acm protecting group was added to the solution, resulting in a dark orange solution. The reaction was monitored via HPLC and was stopped once the starting material peak was no longer present. To stop the reaction, ice-cold diethyl ether (9 volume equivalents) was added to the reaction solution to simultaneously quench the I_2 and isolate the peptide product. The solution was cooled on dry ice for 3 minutes followed by centrifugation for 3 minutes at 5000 RPM. The ether solution was decanted, and the cyclic peptide product was prepared for HPLC purification. Reverse phase HPLC was performed as described above with the following gradients used for each candidate peptide:

DP1c-FAM: 10%-60% Acetonitrile + 0.1% TFA: H_2O + 0.1% TFA in 30 minutes. DP1c-FAM was eluted at 12.6 and 12.9 minutes.

DP2c-FAM: 15%-50% Acetonitrile + 0.1% TFA: H_2O + 0.1% TFA in 30 minutes. DP2c-FAM was eluted at 7.7 and 8.0 minutes.

DP3c-FAM: 10%-60% Acetonitrile + 0.1% TFA: H_2O + 0.1% TFA in 30 minutes. DP3c-FAM was eluted at 9.6 minutes.

DP4c-FAM: 15%-70% Acetonitrile + 0.1% TFA: H_2O + 0.1% TFA in 30 minutes. DP4c-FAM was eluted at 6.7 minutes.

Cell Lines

Human colorectal carcinoma cells (HCT116) were obtained from Dr. Seulki Lee. HCT116 constitutively express DR5[168]. The HCT116 cells were maintained in RPMI 1640 medium (Corning Cellgro), supplemented with 10% fetal bovine serum (FBS) and 1% penicillin-streptomycin (Corning Cellgro). Cell cultures were maintained at 37 °C and 5% carbon dioxide (CO_2) in a humidified incubator.

In vitro binding of FAM-labelled peptides

To assess the binding of our candidate peptides to death receptor 5, we performed flow cytometry analysis. Cells were detached using nonenzymatic cell dissociation buffer (Gibco) and suspended in phosphate-buffered saline (PBS) buffer supplemented with 2 mM of EDTA and 1% FBS (FACS buffer) to a final concentration of 1 x 10^6 cells/100 µL solution. 100 µL of the FAM-labelled peptide was added to the aliquots (final concentration: 200 nM), mixed, and left to incubate for 1 hour at 37 °C and 5% CO_2 in the dark. Cells were then washed three times with FACS buffer, resuspended in FACS buffer, and filtered before flow cytometry analysis. Flow cytometry analysis was completed on a FACSCalibur flow cytometer (Becton Dickinson), with at least 20,000 events recorded.

Results

Synthesis and purification of Acm-protected peptides

Peptide synthesis of Acm-protected peptides was completed without issue on the Liberty Blue automated peptide synthesizer. For each candidate peptide, 6-FAM was added at the N-terminal of the peptide as the last step of the synthesis. Washing, drying, and global deprotection of the peptides from their resins resulted in peptide products that were separable via HPLC. A representative HPLC trace of DP1-ACM-FAM is shown in Figure 6-1. ESI-MS characterization of peptide candidates confirmed the major product peaks collected corresponded to the Acm-protected peptide product (Figure 6-2).

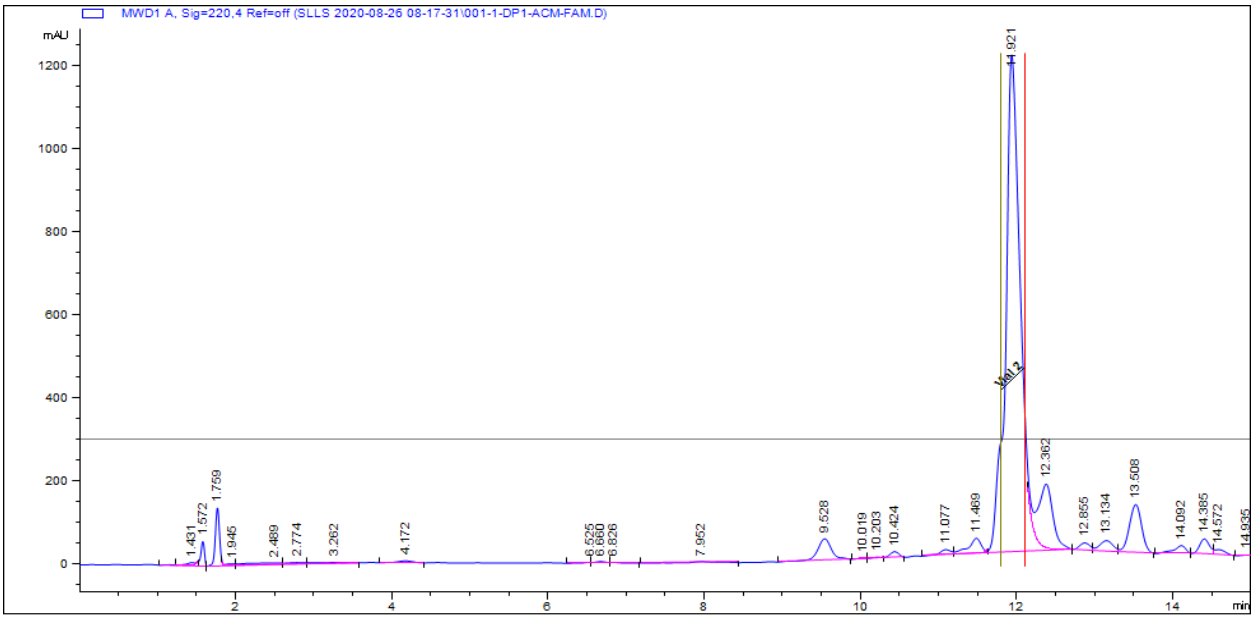

Figure 6-1. HPLC analysis of DP1-ACM-FAM.

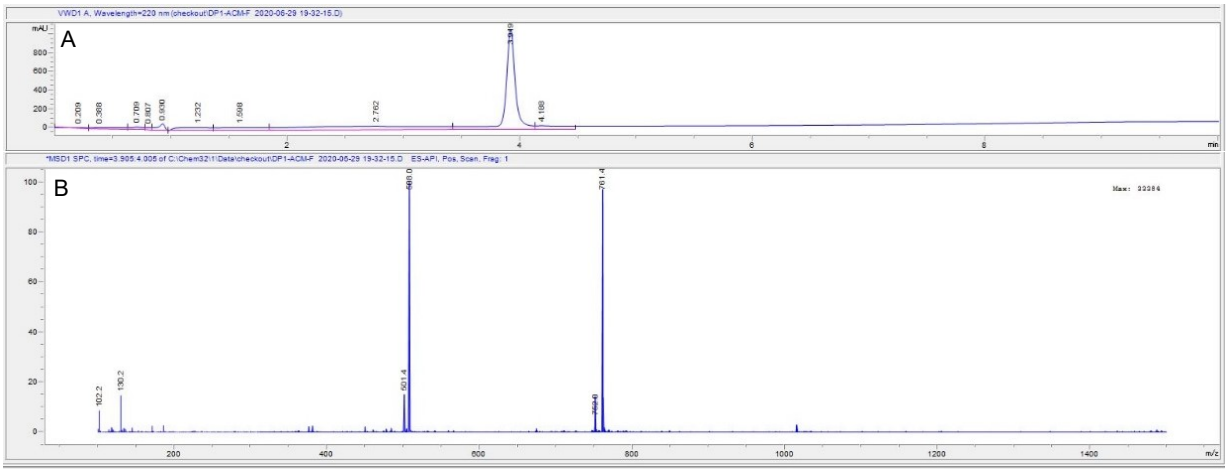

Figure 6-2. ESI-MS analysis of DP1-ACM-FAM.

A. LC chromatogram of purified DP1-ACM-FAM detected at wavelength 220 nm.

B. MS spectra of DP1-ACM-FAM. Observed peaks correspond to the m/z of $[M+2H]^{2+}$ and $[M+3H]^{3+}$.

Cyclization of Acm-protected peptides

To form cyclic peptides via disulfide bond formation, Acm-protected peptides underwent I_2 oxidation to simultaneously remove the Acm-protecting groups and form the disulfide bonds. Within 60 minutes, formation of product peaks was observed for all peptide candidates (Figure 6-3). Reaction time for each peptide candidate differed slightly, with DP1c-FAM taking 180 minutes to reach completion and DP3c-FAM taking closer to 300 minutes to complete. At later timepoints, the additional product peak formation was observed, most likely due to side chain reactions.

ESI-MS characterization of cyclic peptide candidates resulted in the identification of the fully deprotected cyclic product of interest. Interestingly, for peptide candidates DP1c-FAM and DP2c-FAM, the two major product peaks of interest corresponded to the major product of interest, likely due to the presence of isomers[169].

Flow cytometry

Initial flow cytometry assessment of the peptide candidates binding to HCT116 colorectal cancer cells is shown in Figure 6-4. All peptide candidates tested demonstrated binding to the HCT116 cells, with candidate DP3c-FAM showing the highest amount of cellular binding.

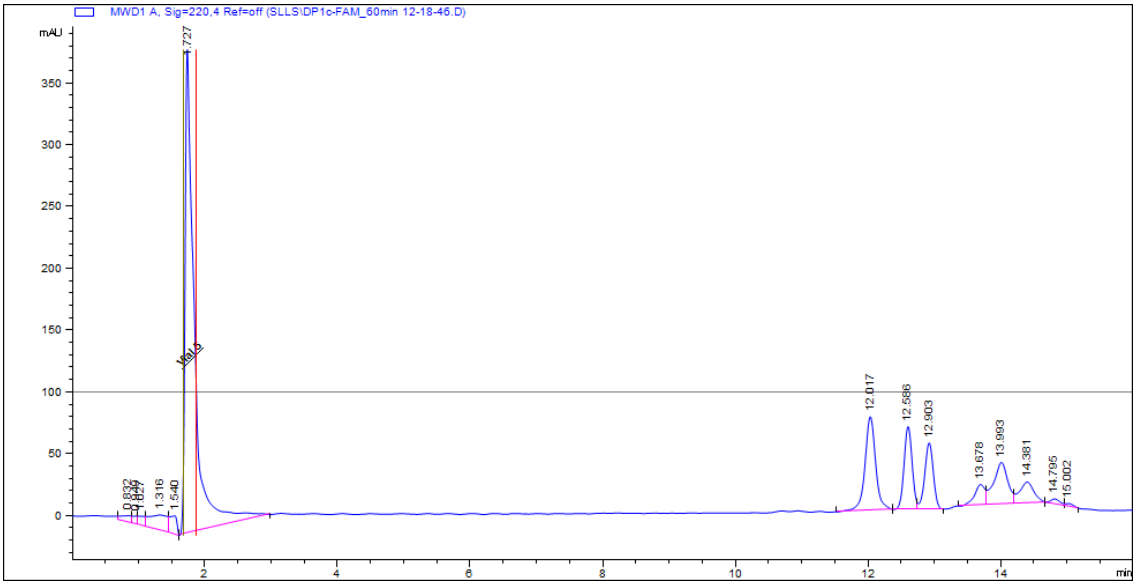

Figure 6-3. HPLC analysis of cyclic reaction of DP1c-FAM at 60 minutes**.**

Detection at 220 nm is shown. The starting material is shown at 12.0 min and the major product peaks of DP1c-FAM are observed at 12.59 min and 12.90 minutes. Additional product peaks are shown between 13.88 and 15.00 minutes.

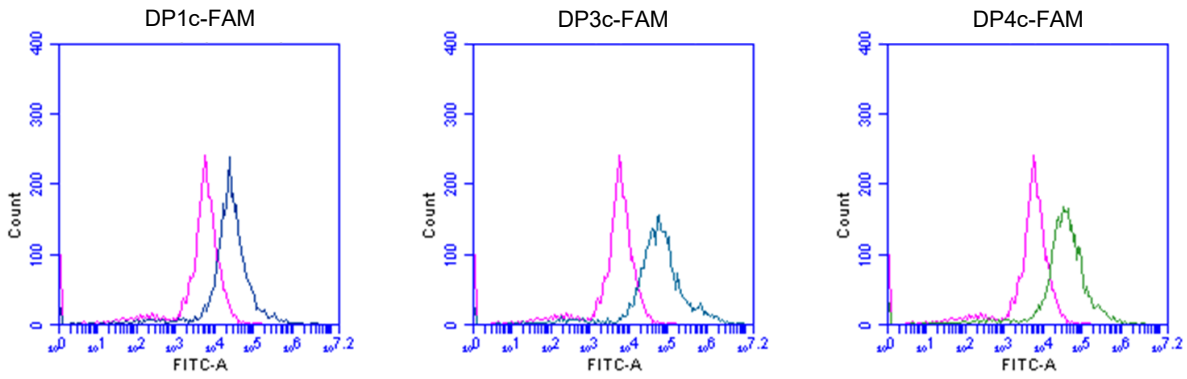

Figure 6-4. Flow cytometry analysis of DP1c-FAM, DP3c-FAM, and DP4c-FAM in HCT116 cells.

The pink peak corresponds to the cells only peak (control) and the blue/green peaks correspond to the HCT116 cells treated with the cyclic peptides.

Discussion

We have shown a solid approach to the synthesis of cyclic peptides identified via phage display. These peptides were synthesized on the solid support, functionalized with a fluorescent label, and converted into cyclic molecules through the formation of a disulfide bind. When testing the ability of these peptides to engage DR5 *in vitro*, we saw that these peptides were able to engage DR5 expressed on human colorectal cancer HCT116 cells.

When approaching the synthesis of these candidate peptides, it was important to control for the labeling of the peptides at the N-terminus. This is because we do not know which amino acids contribute to the binding of the peptide to DR5, so labeling of the peptide at the N-terminus was done to minimize the alteration of the bioactivity of these peptide candidates[170]. Since all the candidate peptides contained lysine residues, it was essential that the labeling of the peptide with 6-FAM was done prior to deprotection of the peptide candidates. This is because unprotected lysine contains an *ε*-amino group that can also readily be labeled with 6-FAM[171]. To avoid this, we moved forward with labeling of the peptide on the solid support followed by subsequent deprotection and cyclization of the peptides.

Since engineered peptides suffer from low stability *in vivo*, we moved forward with a cyclic strategy when preparing our candidate peptides. Cyclic peptides are known to have longer half-lives *in vivo* due to increased structural stability and resistance to proteolysis[172] as well as improved binding ability due to conformational rigidity resulting in more entropically favored interaction[173]. Additionally, since our candidate peptides contain free sulfhydryl groups in their unprotected, linear form, there was the potential for random multimerization of these peptides. To avoid this issue and improve the stability of these peptides, we moved forward with cyclizing these peptides by leveraging their cysteine groups to form disulfide bonds. Although there are numerous approaches to disulfide bond formation in peptides[174], we chose to use an I_2 oxidation approach that simultaneously removed the Acm protecting groups and formed the disulfide bonds due to its simplicity and favorable reaction

outcomes[175]. Since the Acm protecting group is stable under most standard peptide synthesis conditions and not TFA-labile[176], this allowed the peptides to remain Acm-protected after global deprotection of other the protecting groups and resin cleavage, preventing unwanted side reactions and allowing us to control the formation of the cyclic product. Interestingly, the cyclization of DP1c-FAM and DP2c-FAM resulted in the production of two product peaks that had the same molecular weight as our cyclic product of interest. Although these results were unexpected, it is most likely due to the formation of isomers during the formation of the disulfide bond linkage[169].

When the peptides were tested in the HCT116 cells, we observed modest binding of the peptide candidates via flow cytometry, with DP3c-FAM showing the most binding to the HCT116 cell line. While these studies show favorable binding of the peptides to DR5, more work is necessary to fully characterize the binding ability of these peptide agents.

Future Work

To fully characterize these peptide candidates, future work will be focused on further characterization of the ability of these agents to bind DR5. To assess the bioactivity of these peptide candidates, we plan to leverage affinity-based approaches, such as bio-layer interferometry (BLI) or surface plasmon resonance (SPR), to provide valuable information of the binding of these agents as well as affinity characteristics, including dissociation constant (K_D) values, which will be used to determine the optimal DR5 peptides.

Once an optimal candidate peptide has been identified, the peptide candidate will be prepared for both NIRF and PET/SPECT applications by leveraging the N-terminal alpha-amino group as the site of modification for both targets. The peptides will be conjugated with a NIR dye, IRDye 800CW® (LI-COR Biosciences), or 1,4,7,10-tetraazacyclododecane-1,4,7,10-tetraacetic acid (DOTA) enabling the peptides to be used for NIRF or SPECT/PET applications, respectively. DOTA-peptides will undergo subsequent radiolabeling with ^{111}In or ^{64}Cu to be functionalized for SPECT or PET. Probes will be purified using HPLC and characterized using mass spectrometry. In addition to previous *in*

vitro experiments, specific binding will be further assessed using cellular uptake and fluorescence-activated cell sorting (FACS) studies using human tumor cell lines, such as DR5+ colon (HCT-116), breast (MCF7), and prostate (PC3). Once these peptides have been fully characterized and tested in *in vitro* models, we will utilize these functionalized peptides to monitor TRAIL-mediated events *in vivo* in mouse xenograft models.

Acknowledgements

I would like to acknowledge Dr. Seulki Lee for being my collaborator on this project and providing his resources and valuable expertise of death receptors to this project. I would also like to thank Dr. Yumin Oh for his assistance with the cellular model and *in vitro* assessment of the peptide candidates. Finally, I would like to thank the Society of Nuclear Medicine and Molecular Imaging (SNMMI) for awarding me the Bradley-Alavi Student Fellowship to help support this work.

References

1. Mankoff, D. A. A definition of molecular imaging. *J. Nucl. Med.* **48**, (2007).
2. Pysz, M. A., Gambhir, S. S. & Willmann, J. K. Molecular imaging: current status and emerging strategies. *Clin. Radiol.* **65**, 500–516 (2010).
3. Willmann, J. K., van Bruggen, N., Dinkelborg, L. M. & Gambhir, S. S. Molecular imaging in drug development. *Nat. Rev. Drug Discov.* **7**, 591–607 (2008).
4. Lu, F.-M. & Yuan, Z. PET/SPECT molecular imaging in clinical neuroscience: recent advances in the investigation of CNS diseases. *Quant. Imaging Med. Surg.* **5**, 433–447 (2015).
5. Jones, M. A. *et al.* Molecular Imaging of Inflammatory Disease. *Biomedicines* **9**, (2021).
6. Weissleder, R. Molecular Imaging in Cancer. *Science (80-.).* **312**, 1168–1171 (2006).
7. Y., C. I. & C., W. J. Cardiovascular Molecular Imaging. *Circulation* **123**, 425–443 (2011).
8. Weber, W. A. *et al.* The Future of Nuclear Medicine, Molecular Imaging, and Theranostics. *J. Nucl. Med.* **61**, 263S LP-272S (2020).
9. Wu, M. & Shu, J. Multimodal Molecular Imaging: Current Status and Future Directions. *Contrast Media Mol. Imaging* **2018**, 1382183 (2018).
10. Martí-Bonmatí, L., Sopena, R., Bartumeus, P. & Sopena, P. Multimodality imaging techniques. *Contrast Media Mol. Imaging* **5**, 180–189 (2010).
11. James, M. L. & Gambhir, S. S. A Molecular Imaging Primer: Modalities, Imaging Agents, and Applications. *Physiol. Rev.* **92**, 897–965 (2012).
12. Chen, K. & Chen, X. Design and development of molecular imaging probes. *Curr. Top. Med. Chem.* **10**, 1227–1236 (2010).
13. R., L. J. & Jeanne, L. Molecular Imaging in Drug Discovery and Development. *Circ. Cardiovasc. Imaging* **11**, e005355 (2018).
14. Zhang, L., Bhatnagar, S., Deschenes, E. & Thurber, G. M. Mechanistic and quantitative insight into cell surface targeted molecular imaging agent design. *Sci. Rep.* **6**, 25424 (2016).
15. Furman, D. *et al.* Chronic inflammation in the etiology of disease across the life span. *Nat. Med.* **25**, 1822–1832 (2019).
16. Kotas, M. E. & Medzhitov, R. Homeostasis, inflammation, and disease susceptibility. *Cell* **160**, 816–827 (2015).
17. Turner, M. D., Nedjai, B., Hurst, T. & Pennington, D. J. Cytokines and chemokines: At the crossroads of cell signalling and inflammatory disease. *Biochimica et biophysica acta* vol. 1843 2563–2582 (2014).
18. Pober, J. S. & Sessa, W. C. Inflammation and the blood microvascular system. *Cold Spring Harb. Perspect. Biol.* **7**, a016345–a016345 (2014).
19. Serhan, C. N. & Savill, J. Resolution of inflammation: the beginning programs the end. *Nat. Immunol.* **6**, 1191–1197 (2005).
20. Sugimoto, M. A., Sousa, L. P., Pinho, V., Perretti, M. & Teixeira, M. M. Resolution of Inflammation: What Controls Its Onset? *Front. Immunol.* **7**, 160 (2016).
21. Yu, D. M. T. *et al.* The dipeptidyl peptidase IV family in cancer and cell biology. *FEBS J.* **277**, 1126–1144 (2010).
22. Kelly, T., Huang, Y., Simms, A. E. & Mazur, A. Fibroblast Activation Protein-α. A Key Modulator of the Microenvironment in Multiple Pathologies. in *International Review of Cell and Molecular Biology* (2012). doi:10.1016/B978-0-12-394308-8.00003-0.

23. Puré, E. & Blomberg, R. Pro-tumorigenic roles of fibroblast activation protein in cancer: back to the basics. *Oncogene* **37**, 4343–4357 (2018).

24. Zi, F. *et al.* Fibroblast activation protein α in tumor microenvironment: Recent progression and implications (Review). *Mol. Med. Rep.* **11**, 3203–3211 (2015).

25. Posadas, I., López-Hernández, B. & Ceña, V. Nicotinic receptors in neurodegeneration. *Curr. Neuropharmacol.* **11**, 298–314 (2013).

26. Court, J. *et al.* Nicotinic receptor abnormalities in Alzheimer's disease. *Biol. Psychiatry* **49**, 175–184 (2001).

27. de Jonge, W. J. & Ulloa, L. The alpha7 nicotinic acetylcholine receptor as a pharmacological target for inflammation. *Br. J. Pharmacol.* **151**, 915–929 (2007).

28. Zarriello, S. *et al.* Humble beginnings with big goals: Small molecule soluble epoxide hydrolase inhibitors for treating CNS disorders. *Prog. Neurobiol.* **172**, 23–39 (2019).

29. Nelson, J. W. *et al.* Role of soluble epoxide hydrolase in age-related vascular cognitive decline. *Prostaglandins Other Lipid Mediat.* **113**–**115**, 30–37 (2014).

30. Park, J. S. *et al.* Targeting of dermal myofibroblasts through death receptor 5 arrests fibrosis in mouse models of scleroderma. *Nat. Commun.* **10**, 1128 (2019).

31. Hinz, B. Formation and function of the myofibroblast during tissue repair. *J. Invest. Dermatol.* **127**, 526–537 (2007).

32. Ho, Y. Y., Lagares, D., Tager, A. M. & Kapoor, M. Fibrosis--a lethal component of systemic sclerosis. *Nat. Rev. Rheumatol.* **10**, 390–402 (2014).

33. Oh, Y. *et al.* Systemic PEGylated TRAIL treatment ameliorates liver cirrhosis in rats by eliminating activated hepatic stellate cells. *Hepatology* **64**, 209–223 (2016).

34. Jacob, M., Chang, L. & Pure, E. Fibroblast Activation Protein in Remodeling Tissues. *Curr. Mol. Med.* (2012) doi:10.2174/156652412803833607.

35. Miao, Q. *et al.* Near-Infrared Fluorescent Molecular Probe for Sensitive Imaging of Keloid. *Angew. Chemie - Int. Ed.* **57**, 1256–1260 (2018).

36. van der Geest, T. *et al.* Imaging fibroblast activation protein to monitor therapeutic effects of neutralizing interleukin-22 in collagen-induced arthritis. *Rheumatol. (United Kingdom)* **57**, 737–747 (2018).

37. Brennen, W. N., Isaacs, J. T. & Denmeade, S. R. Rationale Behind Targeting Fibroblast Activation Protein– Expressing Carcinoma-Associated Fibroblasts as a Novel Chemotherapeutic Strategy. *Mol. Cancer Ther.* **11**, 257–266 (2012).

38. Waumans, Y., Baerts, L., Kehoe, K., Lambeir, A. M. & De Meester, I. The dipeptidyl peptidase family, prolyl oligopeptidase and prolyl carboxypeptidase in the immune system and inflammatory disease, including atherosclerosis. *Front. Immunol.* **6**, 1–18 (2015).

39. Chen, S.-J. & Jiaang, W.-T. Current Advances and Therapeutic Potential of Agents Targeting Dipepti- dyl Peptidases-IV, -II, 8/9 and Fibroblast Activation Protein. *Curr. Top. Med. Chem.* **11**, 1447–1463 (2011).

40. Juillerat-Jeanneret, L., Tafelmeyer, P. & Golshayan, D. Fibroblast activation protein-α in fibrogenic disorders and cancer: more than a prolyl-specific peptidase? *Expert Opin. Ther. Targets* **21**, 977–991 (2017).

41. Yazbeck, R., Jaenisch, S. E. & Abbott, C. A. Potential disease biomarkers: dipeptidyl peptidase 4 and fibroblast activation protein. *Protoplasma* **255**, 375–386 (2018).

42. Chen, X. & Song, E. Turning foes to friends: targeting cancer-associated fibroblasts. *Nat. Rev. Drug Discov.* (2018) doi:10.1038/s41573-018-0004-1.

43. Quail, D. F. & Joyce, J. A. Microenvironmental regulation of tumor progression and metastasis. *Nat. Med.* **19**, 1423–1437 (2013).

44. Shi, M. *et al.* Expression of fibroblast activation protein in human pancreatic adenocarcinoma and its clinicopathological significance. *World J. Gastroenterol.* (2012) doi:10.3748/wjg.v18.i8.840.

45. Sandberg, T. P. *et al.* Increased expression of cancer-associated fibroblast markers at the invasive front and its association with tumor-stroma ratio in colorectal cancer. *BMC Cancer* **19**, 284 (2019).

46. Chen, L., Qiu, X., Wang, X. & He, J. FAP positive fibroblasts induce immune checkpoint blockade resistance in colorectal cancer via promoting immunosuppression. *Biochem. Biophys. Res. Commun.* (2017) doi:10.1016/j.bbrc.2017.03.039.

47. Lo, A. *et al.* Fibroblast activation protein augments progression and metastasis of pancreatic ductal adenocarcinoma. *JCI Insight* **2**, (2017).

48. Liao, Y., Ni, Y., He, R., Liu, W. & Du, J. Clinical implications of fibroblast activation protein-α in non-small cell lung cancer after curative resection: A new predictor for prognosis. *J. Cancer Res. Clin. Oncol.* **139**, 1523–1528 (2013).

49. Henry, L. R. *et al.* Clinical implications of fibroblast activation protein in patients with colon cancer. *Clin. Cancer Res.* (2007) doi:10.1158/1078-0432.CCR-06-1746.

50. Welt, S. *et al.* Antibody targeting in metastatic colon cancer: A phase I study of monoclonal antibody F19 against a cell-surface protein of reactive tumor stromal fibroblasts. *J. Clin. Oncol.* **12**, 1193–1203 (1994).

51. Laverman, P. *et al.* Immuno-PET and Immuno-SPECT of Rheumatoid Arthritis with Radiolabeled Anti-Fibroblast Activation Protein Antibody Correlates with Severity of Arthritis. *J. Nucl. Med.* **56**, 778–783 (2015).

52. Meletta, R. *et al.* Evaluation of the radiolabeled boronic acid-based FAP inhibitor MIP-1232 for atherosclerotic plaque imaging. *Molecules* **20**, 2081–2099 (2015).

53. Wolf, B. B., Quan, C., Tran, T., Wiesmann, C. & Sutherlin, D. On the edge of validation--cancer protease fibroblast activation protein. *Mini Rev. Med. Chem.* **8**, 719–727 (2008).

54. Hu, Y. *et al.* Synthesis and structure-activity relationship of N-alkyl Gly-boro-Pro inhibitors of DPP4, FAP, and DPP7. *Bioorg. Med. Chem. Lett.* **15**, 4239–4242 (2005).

55. Lindner, T. *et al.* Development of quinoline-based theranostic ligands for the targeting of fibroblast activation protein. *J. Nucl. Med.* **59**, 1415–1422 (2018).

56. Jansen, K. *et al.* Selective Inhibitors of Fibroblast Activation Protein (FAP) with a (4-Quinolinoyl)-glycyl-2-cyanopyrrolidine Scaffold. *ACS Med. Chem. Lett.* **4**, 491–496 (2013).

57. Jansen, K. *et al.* Extended structure-activity relationship and pharmacokinetic investigation of (4-quinolinoyl)glycyl-2-cyanopyrrolidine inhibitors of fibroblast activation protein (FAP). *J. Med. Chem.* **57**, 3053–3074 (2014).

58. Loktev, A. *et al.* A Tumor-Imaging Method Targeting Cancer-Associated Fibroblasts. *J. Nucl. Med.* **59**, 1423–1429 (2018).

59. Giesel, F. L. *et al.* 68 Ga-FAPI PET/CT: Biodistribution and Preliminary Dosimetry Estimate of 2 DOTA-Containing FAP-Targeting Agents in Patients with Various Cancers . *J. Nucl. Med.* (2019) doi:10.2967/jnumed.118.215913.

60. Roy, J., Hettiarachchi, S. U., Kaake, M., Mukkamala, R. & Low, P. S. Design and validation of fibroblast activation protein alpha targeted imaging and therapeutic agents. *Theranostics* **10**, 5778–5789 (2020).

61. Westerlund, K. *et al.* Increasing the Net Negative Charge by Replacement of DOTA Chelator with DOTAGA Improves the Biodistribution of Radiolabeled Second-Generation Synthetic Affibody

Molecules. *Mol. Pharm.* **13**, 1668–1678 (2016).

62. Xavier, M.-A. E., Liu, S., Leppla, S. H. & Cornelissen, B. Pre-labelling versus direct labelling of anthrax proteins for imaging of matrix metalloproteinases activity using DOTA-GA. *Nucl. Med. Biol.* **72**–**73**, 49–54 (2019).

63. Moreau, M. *et al.* DOTAGA-Trastuzumab. A New Antibody Conjugate Targeting HER2/Neu Antigen for Diagnostic Purposes. *Bioconjug. Chem.* **23**, 1181–1188 (2012).

64. Eisenwiener, K. P., Powell, P. & Mäcke, H. R. A convenient synthesis of novel bifunctional prochelators for coupling to bioactive peptides for radiometal labelling. *Bioorg. Med. Chem. Lett.* **10**, 2133–2135 (2000).

65. Ogawa, Y. *et al.* Three Distinct Stroma Types in Human Pancreatic Cancer Identified by Image Analysis of Fibroblast Subpopulations and Collagen. *Clin. cancer Res. an Off. J. Am. Assoc. Cancer Res.* **27**, 107–119 (2021).

66. Ryabtsova, O. *et al.* Acylated Gly-(2-cyano)pyrrolidines as inhibitors of fibroblast activation protein (FAP) and the issue of FAP/prolyl oligopeptidase (PREP)-selectivity. *Bioorganic Med. Chem. Lett.* **22**, 3412–3417 (2012).

67. Loktev, A. *et al.* Development of fibroblast activation protein-targeted radiotracers with improved tumor retention. *J. Nucl. Med.* **60**, 1421–1429 (2019).

68. Fiori, M. E. *et al.* Cancer-associated fibroblasts as abettors of tumor progression at the crossroads of EMT and therapy resistance. *Mol. Cancer* **18**, 1–16 (2019).

69. Sadelain, M., Rivière, I. & Riddell, S. Therapeutic T cell engineering. *Nature* **545**, 423–431 (2017).

70. Hou, C. M. *et al.* Fibroblast activation proteins-α suppress tumor immunity by regulating T cells and tumor-associated macrophages. *Exp. Mol. Pathol.* **104**, 29–37 (2018).

71. Cheng, Y. & Prusoff, W. H. Relationship between the inhibition constant (K1) and the concentration of inhibitor which causes 50 per cent inhibition (I50) of an enzymatic reaction. *Biochem. Pharmacol.* **22**, 3099–3108 (1973).

72. Barretina, J. *et al.* The Cancer Cell Line Encyclopedia enables predictive modelling of anticancer drug sensitivity. *Nature* (2012) doi:10.1038/nature11003.

73. Goldman, M. *et al.* The UCSC Xena platform for public and private cancer genomics data visualization and interpretation. *bioRxiv* (2019) doi:10.1101/326470.

74. Hung, Y.-W. *et al.* Soluble epoxide hydrolase activity regulates inflammatory responses and seizure generation in two mouse models of temporal lobe epilepsy. *Brain. Behav. Immun.* **43**, 118–129 (2015).

75. Ren, Q. *et al.* Gene deficiency and pharmacological inhibition of soluble epoxide hydrolase confers resilience to repeated social defeat stress. *Proc. Natl. Acad. Sci.* **113**, E1944 LP-E1952 (2016).

76. Ren, Q. *et al.* Soluble epoxide hydrolase plays a key role in the pathogenesis of Parkinson's disease. *Proc. Natl. Acad. Sci.* **115**, E5815 LP-E5823 (2018).

77. Horti, A. G. *et al.* 18F-FNDP for PET Imaging of Soluble Epoxide Hydrolase. *J. Nucl. Med.* **57**, 1817–1822 (2016).

78. Du, Y. *et al.* PET imaging of soluble epoxide hydrolase in non-human primate brain with [18F]FNDP. *EJNMMI Res.* **10**, 67 (2020).

79. Azad, B. B., Holt, D. P., Ravert, H. T., Horti, A. G. & Dannals, R. F. An optimized radiosynthesis of [18F]FNDP, a positron emission tomography radiotracer for imaging soluble epoxide hydrolase (sEH). *J. Label. Compd. Radiopharm.* **61**, 567–572 (2018).

80. Rahmim, A., Cheng, J.-C., Blinder, S., Camborde, M.-L. & Sossi, V. Statistical dynamic image reconstruction in state-of-the-art high-resolution PET. *Phys. Med. Biol.* **50**, 4887–4912 (2005).

81. Innis, R. B. *et al.* Consensus Nomenclature for in vivo Imaging of Reversibly Binding Radioligands. *J. Cereb. Blood Flow Metab.* **27**, 1533–1539 (2007).

82. Logan, J. *et al.* Graphical Analysis of Reversible Radioligand Binding from Time—Activity Measurements Applied to [N-11C-Methyl]-(−)-Cocaine PET Studies in Human Subjects. *J. Cereb. Blood Flow Metab.* **10**, 740–747 (1990).

83. Glatting, G., Kletting, P., Reske, S. N., Hohl, K. & Ring, C. Choosing the optimal fit function: Comparison of the Akaike information criterion and the F-test. *Med. Phys.* **34**, 4285–4292 (2007).

84. Golla, S. S. V *et al.* Model selection criteria for dynamic brain PET studies. *EJNMMI Phys.* **4**, 30 (2017).

85. Sjöstedt, E. *et al.* An atlas of the protein-coding genes in the human, pig, and mouse brain. *Science (80-.).* **367**, eaay5947 (2020).

86. Dani, J. A. Overview of nicotinic receptors and their roles in the central nervous system. *Biol. Psychiatry* **49**, 166–174 (2001).

87. Pimlott, S. L. *et al.* Nicotinic acetylcholine receptor distribution in Alzheimer's disease, dementia with Lewy bodies, Parkinson's disease, and vascular dementia: in vitro binding study using 5-[(125)i]-a-85380. *Neuropsychopharmacol. Off. Publ. Am. Coll. Neuropsychopharmacol.* **29**, 108–116 (2004).

88. Sabri, O., Kendziorra, K., Wolf, H., Gertz, H.-J. & Brust, P. Acetylcholine receptors in dementia and mild cognitive impairment. *Eur. J. Nucl. Med. Mol. Imaging* **35 Suppl 1**, S30-45 (2008).

89. Meyer, P. M. *et al.* Reduced alpha4beta2*-nicotinic acetylcholine receptor binding and its relationship to mild cognitive and depressive symptoms in Parkinson disease. *Arch. Gen. Psychiatry* **66**, 866–877 (2009).

90. Marutle, A., Warpman, U., Bogdanovic, N. & Nordberg, A. Regional distribution of subtypes of nicotinic receptors in human brain and effect of aging studied by (+/-)-[3H]epibatidine. *Brain Res.* **801**, 143–149 (1998).

91. Mitsis, E. M. *et al.* Age-related decline in nicotinic receptor availability with [(123)I]5-IA-85380 SPECT. *Neurobiol. Aging* **30**, 1490–1497 (2009).

92. Sultzer, D. L. *et al.* Cholinergic Receptor Binding in Alzheimer Disease and Healthy Aging: Assessment In Vivo with Positron Emission Tomography Imaging. *Am. J. Geriatr. psychiatry Off. J. Am. Assoc. Geriatr. Psychiatry* **25**, 342–353 (2017).

93. Horti, A. G. & Villemagne, V. L. The quest for Eldorado: development of radioligands for in vivo imaging of nicotinic acetylcholine receptors in human brain. *Curr. Pharm. Des.* **12**, 3877–3900 (2006).

94. Horti, A. G., Kuwabara, H., Holt, D. P., Dannals, R. F. & Wong, D. F. Recent PET radioligands with optimal brain kinetics for imaging nicotinic acetylcholine receptors. *J. Labelled Comp. Radiopharm.* **56**, 159–166 (2013).

95. Paterson, D. & Nordberg, A. Neuronal nicotinic receptors in the human brain. *Prog. Neurobiol.* **61**, 75–111 (2000).

96. Kuwabara, H. *et al.* Imaging α4β2 Nicotinic Acetylcholine Receptors (nAChRs) in Baboons with [18F]XTRA, a Radioligand with Improved Specific Binding in Extra-Thalamic Regions. *Mol. Imaging Biol.* **19**, 280–288 (2017).

97. Gao, Y. *et al.* Discovery of (-)-7-methyl-2-exo-[3′-(6-[18F]nuoropyridin- 2-yl)-5′-pyridinyl]-7-azabicyclo[2.2.1]heptane, a radiolabeled antagonist for cerebral nicotinic acetylcholine receptor (α4β2-nAChR) with optimal positron emission tomography imaging properties. *J. Med. Chem.* **51**, 4751–4764 (2008).

98. Pichika, R. *et al.* Nicotinic alpha4beta2 receptor imaging agents: part II. Synthesis and biological evaluation of 2-[18F]fluoro-3-[2-((S)-3-pyrrolinyl)methoxy]pyridine (18F-nifene) in rodents and

imaging by PET in nonhuman primate. *Nucl. Med. Biol.* **33**, 295–304 (2006).

99. Smits, R. *et al.* Synthesis and biological evaluation of both enantiomers of [(18)F]flubatine, promising radiotracers with fast kinetics for the imaging of α4β2-nicotinic acetylcholine receptors. *Bioorg. Med. Chem.* **22**, 804–812 (2014).

100. Hughes, C. P., Berg, L., Danziger, W. L., Coben, L. A. & Martin, R. L. A new clinical scale for the staging of dementia. *Br. J. Psychiatry* **140**, 566–572 (1982).

101. Poirier, J. *et al.* Apolipoprotein E4 allele as a predictor of cholinergic deficits and treatment outcome in Alzheimer disease. *Proc. Natl. Acad. Sci. U. S. A.* **92**, 12260–12264 (1995).

102. Wevers, A. *et al.* Expression of nicotinic acetylcholine receptors in Alzheimer's disease: postmortem investigations and experimental approaches. *Behav. Brain Res.* **113**, 207–215 (2000).

103. Coughlin, J. M. J. M. *et al.* The distribution of the alpha7 nicotinic acetylcholine receptor in healthy aging: An in vivo positron emission tomography study with [18F]ASEM. *Neuroimage* **165**, 118–124 (2018).

104. Sossi, V. *et al.* The second generation HRRT-a multi-centre scanner performance investigation. in *IEEE Nuclear Science Symposium Conference Record, 2005* vol. 4 2195–2199 (IEEE, 2005).

105. Hilton, J. *et al.* Column-switching HPLC for the analysis of plasma in PET imaging studies. *Nucl. Med. Biol.* **27**, 627–630 (2000).

106. Bevington, P. R. & Robinson, D. K. Data reduction and error analysis. *McGrawâ€"Hill, New York* (2003).

107. Hillmer, A. T. *et al.* Imaging of cerebral α4β2* nicotinic acetylcholine receptors with (-)-[(18)F]Flubatine PET: Implementation of bolus plus constant infusion and sensitivity to acetylcholine in human brain. *Neuroimage* **141**, 71–80 (2016).

108. Akaike, H. A new look at the statistical model identification. *IEEE Trans. Automat. Contr.* **19**, 716–723 (1974).

109. Carson, R. E. Positron emission tomography and autoradiography: Principles and applications for the Positron emission tomography and autoradiography: Principles and applications for the brain and heart, Chapter Parameter estimation in positron emission tomography. (1986).

110. Hoaglin, D. C. & Iglewicz, B. Fine-tuning some resistant rules for outlier labeling. *J. Am. Stat. Assoc.* **82**, 1147–1149 (1987).

111. Horti, A. G. & Wong, D. F. Clinical Perspective and Recent Development of PET Radioligands for Imaging Cerebral Nicotinic Acetylcholine Receptors. *PET Clin.* **4**, 89–100 (2009).

112. Volkow, N. D., Ding, Y.-S., Fowler, J. S. & Gatley, S. J. Imaging brain cholinergic activity with positron emission tomography: its role in the evaluation of cholinergic treatments in Alzheimer's dementia. *Biol. Psychiatry* **49**, 211–220 (2001).

113. Court, J. A., Martin-Ruiz, C., Graham, A. & Perry, E. Nicotinic receptors in human brain: topography and pathology. *J. Chem. Neuroanat.* **20**, 281–298 (2000).

114. Mukherjee, J. *et al.* Human brain imaging of nicotinic acetylcholine α4β2* receptors using [(18) F]Nifene: Selectivity, functional activity, toxicity, aging effects, gender effects, and extrathalamic pathways. *J. Comp. Neurol.* **526**, 80–95 (2018).

115. Sabri, O. *et al.* First-in-human PET quantification study of cerebral α4β2* nicotinic acetylcholine receptors using the novel specific radioligand (-)-[(18)F]Flubatine. *Neuroimage* **118**, 199–208 (2015).

116. Wong, D. F. *et al.* PET imaging of high-affinity α4β2 nicotinic acetylcholine receptors in humans with 18F-AZAN, a radioligand with optimal brain kinetics. *J. Nucl. Med.* **54**, 1308–1314 (2013).

117. Quik, M., Perez, X. A. & Grady, S. R. Role of α6 nicotinic receptors in CNS dopaminergic function:

relevance to addiction and neurological disorders. *Biochem. Pharmacol.* **82**, 873–882 (2011).

118. Wallace, T. L. & Porter, R. H. P. Targeting the nicotinic alpha7 acetylcholine receptor to enhance cognition in disease. *Biochem. Pharmacol.* **82**, 891–903 (2011).

119. Freedman, R., Hall, M., Adler, L. E. & Leonard, S. Evidence in postmortem brain tissue for decreased numbers of hippocampal nicotinic receptors in schizophrenia. *Biol. Psychiatry* **38**, 22–33 (1995).

120. Marutle, A. *et al.* Laminar distribution of nicotinic receptor subtypes in cortical regions in schizophrenia. *J. Chem. Neuroanat.* **22**, 115–126 (2001).

121. Guan, Z. Z., Zhang, X., Ravid, R. & Nordberg, A. Decreased protein levels of nicotinic receptor subunits in the hippocampus and temporal cortex of patients with Alzheimer's disease. *J. Neurochem.* **74**, 237–243 (2000).

122. D'hoedt, D. & Bertrand, D. Nicotinic acetylcholine receptors: an overview on drug discovery. *Expert Opin. Ther. Targets* **13**, 395–411 (2009).

123. Hurst, R., Rollema, H. & Bertrand, D. Nicotinic acetylcholine receptors: from basic science to therapeutics. *Pharmacol. Ther.* **137**, 22–54 (2013).

124. Mazurov, A. A., Speake, J. D. & Yohannes, D. Discovery and development of α7 nicotinic acetylcholine receptor modulators. *J. Med. Chem.* **54**, 7943–7961 (2011).

125. Mazurov, A. A. *et al.* Discovery of (2S,3R)-N-[2-(pyridin-3-ylmethyl)-1-azabicyclo[2.2.2]oct-3-yl]benzo[b]furan-2-carboxamide (TC-5619), a selective α7 nicotinic acetylcholine receptor agonist, for the treatment of cognitive disorders. *J. Med. Chem.* **55**, 9793–9809 (2012).

126. Olincy, A. *et al.* Proof-of-concept trial of an alpha7 nicotinic agonist in schizophrenia. *Arch. Gen. Psychiatry* **63**, 630–638 (2006).

127. Shytle, R. D., Silver, A. A., Sheehan, K. H., Sheehan, D. V & Sanberg, P. R. Neuronal nicotinic receptor inhibition for treating mood disorders: preliminary controlled evidence with mecamylamine. *Depress. Anxiety* **16**, 89–92 (2002).

128. Taly, A. & Charon, S. α7 nicotinic acetylcholine receptors: a therapeutic target in the structure era. *Curr. Drug Targets* **13**, 695–706 (2012).

129. Perry, E. K., Martin-Ruiz, C. M. & Court, J. A. Nicotinic receptor subtypes in human brain related to aging and dementia. *Alcohol* **24**, 63–68 (2001).

130. Horti, A. G. Development of [18F]ASEM, a specific radiotracer for quantification of the α7-nAChR with positron-emission tomography. *Biochem. Pharmacol.* **97**, 566–575 (2015).

131. Horti, A. G. *et al.* 18F-ASEM, a radiolabeled antagonist for imaging the aα7-nicotinic acetylcholine receptor with PET. *J. Nucl. Med.* **55**, 672–677 (2014).

132. Hillmer, A. T. *et al.* PET imaging of α7 nicotinic acetylcholine receptors: a comparative study of [18F]ASEM and [18F]DBT-10 in nonhuman primates, and further evaluation of [18F]ASEM in humans. *Eur. J. Nucl. Med. Mol. Imaging* **44**, 1042–1050 (2017).

133. Wong, D. F. *et al.* Human Brain Imaging of α7 nAChR with [18F]ASEM: a New PET Radiotracer for Neuropsychiatry and Determination of Drug Occupancy. *Mol. Imaging Biol.* **16**, 730–738 (2014).

134. Court, J. A. *et al.* Nicotinic and muscarinic cholinergic receptor binding in the human hippocampal formation during development and aging. *Brain Res. Dev. Brain Res.* **101**, 93–105 (1997).

135. Hellström-Lindahl, E. & Court, J. A. Nicotinic acetylcholine receptors during prenatal development and brain pathology in human aging. *Behav. Brain Res.* **113**, 159–168 (2000).

136. Nordberg, A. & Winblad, B. Brain Nicotinic and Muscarinic Receptors in Normal Aging and Dementia. in *Alzheimer's and Parkinson's Disease: Strategies for Reseach and Development* 95–108 (1986).

137. Utsugisawa, K. *et al.* Changes with aging and ischemia in nicotinic acetylcholine receptor subunit alpha7 mRNA expression in postmortem human frontal cortex and putamen. *Neurosci. Lett.* **270**, 145–148 (1999).

138. Folstein, M. F., Folstein, S. E. & McHugh, P. R. 'Mini-mental state'. A practical method for grading the cognitive state of patients for the clinician. *J. Psychiatr. Res.* **12**, 189–198 (1975).

139. Wechsler, D. Wechsler adult intelligence scale--. (1955).

140. Delis, D. C., Kaplan, E. & Kramer, J. H. Delis-Kaplan executive function system. (2001).

141. Freedman, M., Leach, L., Kaplan, E., Shulman, K. & Delis, D. C. *Clock drawing: A neuropsychological analysis*. (Oxford University Press, USA, 1994).

142. Delis, D. C., Kramer, J. H., Kaplan, E. & Thompkins, B. A. O. *CVLT: California verbal learning test-adult version: manual*. (Psychological Corporation, 1987).

143. Gao, Y. *et al.* Derivatives of dibenzothiophene for positron emission tomography imaging of α7-nicotinic acetylcholine receptors. *J. Med. Chem.* **56**, 7574–7589 (2013).

144. Coughlin, J. M. *et al.* Neuroinflammation and brain atrophy in former NFL players: An in vivo multimodal imaging pilot study. *Neurobiol. Dis.* **74**, 58–65 (2015).

145. Levin, E. D. α7-Nicotinic receptors and cognition. *Curr. Drug Targets* **13**, 602–606 (2012).

146. De Leon, M. J. *et al.* Frequency of hippocampal formation atrophy in normal aging and Alzheimer's disease. *Neurobiol. Aging* **18**, 1–11 (1997).

147. Driscoll, I. *et al.* Longitudinal pattern of regional brain volume change differentiates normal aging from MCI. *Neurology* **72**, 1906–1913 (2009).

148. Tisserand, D. J. *et al.* A voxel-based morphometric study to determine individual differences in gray matter density associated with age and cognitive change over time. *Cereb. Cortex* **14**, 966–973 (2004).

149. Young, J. W. *et al.* Nicotine improves sustained attention in mice: evidence for involvement of the alpha7 nicotinic acetylcholine receptor. *Neuropsychopharmacol. Off. Publ. Am. Coll. Neuropsychopharmacol.* **29**, 891–900 (2004).

150. Ikonomovic, M. D. *et al.* Cortical alpha7 nicotinic acetylcholine receptor and beta-amyloid levels in early Alzheimer disease. *Arch. Neurol.* **66**, 646–651 (2009).

151. Nishiyama, S., Ohba, H., Kanazawa, M., Kakiuchi, T. & Tsukada, H. Comparing α7 nicotinic acetylcholine receptor binding, amyloid-β deposition, and mitochondria complex-I function in living brain: A PET study in aged monkeys. *Synapse* **69**, 475–483 (2015).

152. Stuckey, D. W. & Shah, K. TRAIL on trial: preclinical advances in cancer therapy. *Trends Mol. Med.* **19**, 685–694 (2013).

153. von Karstedt, S., Montinaro, A. & Walczak, H. Exploring the TRAILs less travelled: TRAIL in cancer biology and therapy. *Nat. Rev. Cancer* **17**, 352–366 (2017).

154. O'Leary, L. *et al.* Decoy receptors block TRAIL sensitivity at a supracellular level: the role of stromal cells in controlling tumour TRAIL sensitivity. *Oncogene* **35**, 1261–1270 (2016).

155. Lemke, J., von Karstedt, S., Zinngrebe, J. & Walczak, H. Getting TRAIL back on track for cancer therapy. *Cell Death Differ.* **21**, 1350–1364 (2014).

156. Ashkenazi, A., Holland, P. & Eckhardt, S. G. Ligand-Based Targeting of Apoptosis in Cancer: The Potential of Recombinant Human Apoptosis Ligand 2/Tumor Necrosis Factor–Related Apoptosis-Inducing Ligand (rhApo2L/TRAIL). *J. Clin. Oncol.* **26**, 3621–3630 (2008).

157. de Miguel, D., Lemke, J., Anel, A., Walczak, H. & Martinez-Lostao, L. Onto better TRAILs for cancer treatment. *Cell Death Differ.* **23**, 733–747 (2016).

158. Chae, S. Y. *et al.* Improved Antitumor Activity and Tumor Targeting of NH2-Terminal–Specific

PEGylated Tumor Necrosis Factor–Related Apoptosis-Inducing Ligand. *Mol. Cancer Ther.* **9**, 1719–1729 (2010).

159. Kim, T. H. *et al.* PEGylated TNF-Related Apoptosis-Inducing Ligand (TRAIL) Analogues: Pharmacokinetics and Antitumor Effects. *Bioconjug. Chem.* **22**, 1631–1637 (2011).

160. Oh, Y. *et al.* Delivery of tumor-homing TRAIL sensitizer with long-acting TRAIL as a therapy for TRAIL-resistant tumors. *J. Control. Release* **220**, 671–681 (2015).

161. Park, J.-S. *et al.* PEGylated TRAIL ameliorates experimental inflammatory arthritis by regulation of Th17 cells and regulatory T cells. *J. Control. Release* **267**, 163–171 (2017).

162. Ichikawa, K. *et al.* TRAIL-R2 (DR5) mediates apoptosis of synovial fibroblasts in rheumatoid arthritis. *J. Immunol.* **171**, 1061–1069 (2003).

163. Lamhamedi-Cherradi, S.-E., Zheng, S., Tisch, R. M. & Chen, Y. H. Critical Roles of Tumor Necrosis Factor–Related Apoptosis-Inducing Ligand in Type 1 Diabetes. *Diabetes* **52**, 2274 LP – 2278 (2003).

164. Pan, X. *et al.* Association of TRAIL and Its Receptors with Large-Artery Atherosclerotic Stroke. *PLoS One* **10**, e0136414–e0136414 (2015).

165. Pedersen, S. L. & Jensen, K. J. Peptide Release, Side-Chain Deprotection, Work-Up, and Isolation. in *Peptide Synthesis and Applications* (eds. Jensen, K. J., Tofteng Shelton, P. & Pedersen, S. L.) 43–63 (Humana Press, 2013). doi:10.1007/978-1-62703-544-6_3.

166. Andreu, D. *et al.* Formation of Disulfide Bonds in Synthetic Peptides and Proteins. in *Peptide Synthesis Protocols* (eds. Pennington, M. W. & Dunn, B. M.) 91–169 (Humana Press, 1995). doi:10.1385/0-89603-273-6:91.

167. Zhang, S. *et al.* Simultaneous Post-cysteine(S-Acm) Group Removal Quenching of Iodine and Isolation of Peptide by One Step Ether Precipitation. *Int. J. Pept. Res. Ther.* **14**, 301–305 (2008).

168. Galligan, L. *et al.* Chemotherapy and TRAIL-mediated colon cancer cell death: the roles of p53, TRAIL receptors, and c-FLIP. *Mol. Cancer Ther.* **4**, 2026–2036 (2005).

169. Chino, N. *et al.* Generation of two isomers with the same disulfide connectivity during disulfide bond formation of human uroguanylin. *Lett. Pept. Sci.* **3**, 45–52 (1996).

170. Gaudriault, G. & Vincent, J. P. Selective labeling of alpha- or epsilon-amino groups in peptides by the Bolton-Hunter reagent. *Peptides* **13**, 1187–1192 (1992).

171. Nanda, J. S. & Lorsch, J. R. Chapter Eight - Labeling a Protein with Fluorophores Using NHS Ester Derivitization. in *Laboratory Methods in Enzymology: Protein Part A* (ed. Lorsch, J. B. T.-M. in E.) vol. 536 87–94 (Academic Press, 2014).

172. Lee, A. C.-L., Harris, J. L., Khanna, K. K. & Hong, J.-H. A Comprehensive Review on Current Advances in Peptide Drug Development and Design. *Int. J. Mol. Sci.* **20**, (2019).

173. Joo, S. H. Cyclic peptides as therapeutic agents and biochemical tools. *Biomol. Ther. (Seoul).* **20**, 19–26 (2012).

174. Chen, L., Annis, I. & Barany, G. Disulfide Bond Formation in Peptides. *Curr. Protoc. Protein Sci.* **23**, 18.6.1-18.6.19 (2001).

175. He, R., Pan, J., Mayer, J. P. & Liu, F. Stepwise Construction of Disulfides in Peptides. *ChemBioChem* **21**, 1101–1111 (2020).

176. Veber, D., Milkowski, J., Varga, S., Denkewalter, R. & Hirschmann, R. Acetamidomethyl. A Novel Thiol Protecting Group for Cysteine. *J. Am. Chem. Soc.* **94**, 5456–5461 (1972).

CV

EDUCATION

Ph.D., Biomedical Engineering, Johns Hopkins University School of Medicine **2015 – Present**

B.S., Bioengineering, University of Illinois at Urbana-Champaign **2011 – 2015**

PROFESSIONAL EXPERIENCE

Webmaster **2019 – Present**

Precision Molecular Imaging Coalition

Johns Hopkins University School of Medicine, Baltimore, MD

- Created and developed website for the Resource for Molecular Imaging Agents in Precision Medicine P41 grant.
- Execute all web-based content updates for the Center for Translational Molecular Imaging (CTMI) website.

Graduate Research Assistant **August 2015 – Present**

Mentor: Martin Pomper, M.D., Ph.D., Department of Radiology

Johns Hopkins University School of Medicine, Baltimore, MD

- Synthesized and assessed peptide-based imaging agents targeting death-receptor 5.
- Developed and evaluated inhibitor-based imaging agents for targeted molecular imaging of fibroblast activation protein alpha (FAP) in mouse cancer models.
- Modeled the kinetics and distribution of ^{18}F brain radiotracers (^{18}F-FNDP, ^{18}F-XTRA, and ^{18}F-ASEM) in human clinical studies.

Undergraduate Research Assistant **June 2013 – May 2015**

Experimental Molecular Imaging Laboratory

Mentor: Professor Wawrzyniec Dobrucki, Department of Bioengineering

Beckman Institute for Advanced Science and Technology, Urbana, IL

- Completed the initial evaluation and characterization of a novel cRGD-peptide imaging agent targeting the $\alpha_V\beta_3$ integrin
- Evaluated the cRGD-peptide agent's ability to assess peripheral angiogenesis in a type-1 diabetes model.

PEER-REVIEWED SCIENTIFIC ARTICLES

Accepted

1. **Slania SL,** Das D, Lisok A, Du Y, Jiang Z, Mease RC, Rowe SP, Nimmagadda S, Yang X, Pomper MG. (2021). Imaging of fibroblast activation protein in cancer xenografts using novel (4-quinolinoyl)-glycyl-2-cyanopyrrolidine-based small molecules. *J Med Chem.* 64(7), 4059-4070.
2. Coughlin JM*, **Slania S***, Du Y*, Shinehouse L, Brosnan MK, Azad BB, Holt DP, Fan H, Lesniak WG, Minn I, Rowe SP, Dannals RF, Horti AG, Pomper MG. (2021). First-in-human neuroimaging of soluble epoxide hydrolase using 18F-FNDP PET. *Eur J Nucl Med Mol Imaging*.
3. Park JS, Oh Y, Park YJ, Park O, Yang H, **Slania S**, … Pomper MG, Lee, S. (2019). Targeting of dermal myofibroblasts through death receptor 5 arrests fibrosis in mouse models of scleroderma. *Nature Communications*, *10*(1), 1128.
4. Hedhli J, **Slania SLL**, Płoska A, Czerwinski A, Konopka CJ, Wozniak M, Banach M, Dobrucki IT, Kalinowski L, Dobrucki LW. (2018). Evaluation of a dimeric-cRGD peptide for targeted PET-CT imaging of peripheral angiogenesis in diabetic mice. *Scientific Reports*, *8*(1), 5401.
5. Coughlin JM*, **Slania S***, Du Y*, Rosenthal HB, Lesniak WG, Minn I, Smith GS, Dannals RF, Kuwabara H, Wong DF, Wang Y, Horti AG, Pomper, MG. (2018). 18F-XTRA PET for enhanced imaging of the extrathalamic α4β2 nicotinic acetylcholine receptor. *Journal of Nuclear Medicine*, *59*(10), 1603–1608.
6. Zhang J, Li Y, **Slania S**, Yadav NN, Liu J, Wang R, Zhang J, Pomper MG, van Zijl PC, Yang X, Liu G. (2018). Phenols as Diamagnetic T2-Exchange Magnetic Resonance Imaging Contrast Agents. *Chemistry - A European Journal*, *24*(6), 1259–1263.
7. Coughlin JM, Du Y, Rosenthal HB, **Slania S**, … Pomper MG. (2018). The distribution of the alpha7 nicotinic acetylcholine receptor in healthy aging: An in vivo positron emission tomography study with [18F]ASEM. *NeuroImage*, *165*, 118–124.

* Authors contributed equally to this work

BOOK CHAPTERS

1. Caffarini J, Kelleher N, Konopka CC, Mazurek M, Nandyala A, Patel D, **Slania S**, Wang S, Yada RC, Pan D. (2016). Multimodal imaging and theranostic application of disease-directed agents. *Topics in Medicinal Chemistry*, *20*, 75–104.

CONFERENCE ABSTRACTS

1. **Slania S,** Lisok A, Rowe SP, Sysa Shah P, Du Y, Pomper MG, Nimmagadda S, Yang X. Small molecule FAP-α inhibitors for targeted molecular imaging of tumor microenvironment. Oral Presentation. 2017 Biomedical Engineering Society Annual Meeting. Phoenix, Arizona.
2. **Slania S**, Czerwinski A, Dobrucki IT, Dobrucki LW. PET-CT imaging of peripheral angiogenesis in type-1 diabetes Using novel dimeric cRGD peptide. Poster Presentation. 2014 Biomedical Engineering Society Annual Meeting. San Antonio, TX.

3. Schuh S, Wozniak M, Hedhli J, **Slania S**, Czerwinski A, Kalinowski L, Dobrucki LW, Dobrucki IT. Using molecular imaging for in vivo evaluation of doxorubicin-based anti-cancer treatment in combination with the herbal medicine black cohosh in MCF-7 xenografts. Poster Presentation. 2014 Biomedical Engineering Society Annual Meeting. San Antonio, TX.
4. **Slania S**, Dobrucki IT, Czerwinski A, Valenzuela F, Dobrucki LW. Initial evaluation of novel dimeric-cRGD peptide for multimodal imaging of angiogenesis. Poster Presentation. 2013 Biomedical Engineering Society Annual Meeting. Seattle, WA.

PATENTS

1. Imaging and radiotherapeutic agents targeting fibroblast-activation protein-α (FAP-α) (W0/2019083990); **Slania S**, Yang X, Nimmagadda S, Rowe S, Pomper MG.

TEACHING EXPERIENCE

Gateway Computing: Python (EN.500.113) **Fall 2020**

Lead Course Assistant, Department of Computer Science, JHU

Supervising Instructors: Dr. Kwame Kutten, Dr. John Edison, Dr. Vishwa Parekh

Immunoengineering (EN.585.751) **Spring 2020**

Teaching Assistant, Department of Biomedical Engineering, JHU

Supervising Instructors: Dr. John Hickey, Elana Ben-Akiva

Systems Bioengineering Lab I (EN.580.421) **Fall 2018**

Teaching Assistant, Department of Biomedical Engineering, JHU

Supervising Instructor: Dr. Benjamin Bejar-Haro

Introduction to Scientific Computing in BME (EN.580.200) **Fall 2017**

Teaching Assistant, Department of Biomedical Engineering, JHU

Supervising Instructor: Dr. Winston Timp

General Chemistry I (CHEM 102) **Spring 2015**

Merit Instructor, Department of Chemistry, UIUC

Supervising Instructor: Dr. Gretchen Adams

Biomedical Instrumentation (BIOE 414) **Spring 2015**

Student Grader, Department of Bioengineering, UIUC

Supervising Instructor: Dr. Wawrzyniec Dobrucki

Signals and Systems in Bioengineering (BIOE 205) **Spring 2014**

Student Grader, Department of Bioengineering, UIUC

Supervising Instructor: Dr. Marcia Pool

Conservation Principles of Bioengineering (BIOE 201) **Fall 2013**

Student Grader, Department of Bioengineering, UIUC

Supervising Instructor: Dr. Princess Imoukhuede

Engineering Grand Challenges (ENG 198) **Fall 2013**

Engineering Learning Assistant, College of Engineering, UIUC

Supervising Instructor: Dr. SungWoo Nam

Engineering Orientation (ENG 100) **Fall 2013**

Engineering Learning Assistant, College of Engineering, UIUC

Supervising Instructor: Michelle Adeoye

HONORS AND AWARDS

Bradley-Alavi Student Fellowship, Society of Nuclear Medicine and Molecular Imaging	2019
Featured Article of the Month, Journal of Nuclear Medicine	2018
NSF GRFP, Honorable Mention	2016
Finalist, Cozad New Venture Competition	2015
Distinguished Service Certificate, Alpha Phi Omega	2015
Kinetic Leadership Knot, Alpha Phi Omega	2014
Second Place, Saint Louis University Elevator Pitch Competition	2014
First Place Venture Capitalist Pitch, Coulter College	2014
Tau Beta Pi Honors Fraternity	2013
James Scholar, College of Engineering, UIUC	2011 – 2015
Dean’s List, College of Engineering, UIUC	Fall 2011 – Spring 2014

LEADERSHIP EXPERIENCE

Member, BME PhD Equity, Diversity, and Inclusion (EDI) Committee, JHU 2020 - Present

- Served as a member of the founding EDI committee and helped develop the group's initiative and goals
- Leads the initiative on mental health advocacy and education for graduate students

Volunteer, Thread Inc., Baltimore, MD 2016 - Present

- Mentored, tutored, and supported high school student to ensure graduation
- Regularly tutored multiple students during after school sessions

President, BME Graduate Student Council, JHU 2016-2017

- Ran monthly council meetings, oversaw all council members and council initiatives, and led the planning for the Annual BME Retreat.

Graduate Student Association Representative, Department of Biomedical Engineering, JHU 2015-2016

- Acted as representative for the BME Ph.D. students to the Graduate Student Association by regularly attending meetings, voting on behalf of BME Ph.D. students, and communicating updates to the BME Ph.D. council.

Alpha Phi Omega, Alpha Alpha Chapter, UIUC 2012-Present

- **Independent Projects Chair** (Fall 2013)
    - Verified and documented 1000+ service hours completed by our chapter's active members
- **Active Member** (Fall 2012 – Spring 2015)
    - Completed 200+ service hours over my 6 semesters of active membership
    - Completed three intensive leadership courses through the APO LEADS leadership development program
- **External Service Committee Director** (Spring 2014)
    - Managed and helped lead a 10 person committee focused on planning service events with community partners
- **Advisor Relations Chair** (Fall 2014)
    - Served as the official liaison between the executive board and advisory board
- **National Service Week Chair** (Fall 2014)

- Coordinated, promoted, and executed a week of service projects to celebrate National Service Week

- **Vice President of Service Internal** (Spring 2015)
  - Served as a member of the Executive Board and voted on important chapter decisions
  - Led a committee focused on creating new service events and forming new service partnerships for the chapter

- **Alumni** (2015-Present)

Biomedical Engineering Society, UIUC Chapter 2012-2015

- **Treasurer** (2013-2015)
  - Maintained a detailed record of the chapter's financial transactions and collected all membership dues

- **President** (2014-2015)
  - Supervised all society affairs and activities, presided over all meetings, and oversaw all chapter officers and committees.
  - Led an initiative to increase chapter membership, increasing membership by almost 50% during my tenure.

Bioengineering Undergraduate Advisory Board, UIUC 2012-2015

- **Sophomore Representative** (2012-2013)
  - Acted as representative to the Advisory Board for the sophomore Bioengineering class

- **Junior Representative** (2013-2014)
  - Acted as representative to the Advisory Board for the junior Bioengineering class

- **Committee Chair** (2014-2015)
  - Oversaw the Advisory Board and acted as the main contact between the Bioengineering students and the department
  - Organized and facilitated monthly meetings focused on providing feedback on curriculum and program changes

Student Volunteer, Presence Health, Champaign, IL Spring 2012- Fall 2013

- Stocked nurses' stations, prepared patient admission packets, and responded to patient request on the Medical-Surgical/Oncology floor.
- Completed 100+ service hours over the four semesters volunteering.